Smart Agriculture 2

Zhao Zhang · Hu Liu · Ce Yang ·
Yiannis Ampatzidis · Jianfeng Zhou ·
Yu Jiang *Editors*

Unmanned Aerial Systems in Precision Agriculture

Technological Progresses and Applications

Springer

Smart Agriculture

Volume 2

Series Editors

Zhao Zhang, Department of Agricultural and Biosystems Engineering, North Dakota State University, Fargo, ND, USA

Yiannis Ampatzidis, UF/IFAS Southwest Florida Research and Education Center, University of Florida, Immokalee, FL, USA

Paulo Flores, Department of Agricultural and Biosystems Engineering, North Dakota State University, Fargo, ND, USA

Yuanjie Wang, Agricultural Information Institute, Chinese Academy of Agricultural Sciences, Beijing, China

The book series Smart Agriculture presents progress of smart agricultural technologies, which includes, but not limited to, specialty crop harvest robotics, UAV technologies for row crops, innovative IoT applications in plant factories, and big data for optimizing production process. It includes both theoretical study and practical applications, with emphasis on systematic studies. AI technologies in agricultural productions will be emphasized, consisting of innovative algorithms and new application domains. Additionally, new crops are emerging, such as hemp in U.S., and covered as well. This book series would cover regions worldwide, such as U.S., Canada, China, Japan, Korea, and Brazil.

The book series Smart Agriculture aims to provide an academic platform for interdisciplinary researchers to provide their state-of-the-art technologies related to smart agriculture. Researchers of different academic backgrounds are encouraged to contribute to the book, such as agriculture engineers, breeders, horticulturist, agronomist, and plant pathologists. The series would target a very broad audience – all having a professional related to agriculture production. It also could be used as textbooks for graduate students.

More information about this series at https://link.springer.com/bookseries/16785

Zhao Zhang · Hu Liu · Ce Yang ·
Yiannis Ampatzidis · Jianfeng Zhou · Yu Jiang
Editors

Unmanned Aerial Systems in Precision Agriculture

Technological Progresses and Applications

Springer

Editors
Zhao Zhang
Key Lab of Smart Agriculture
Systems, Ministry of Education
China Agricultural University
Beijing, China

Hu Liu
Chinese Academy of Sciences
Northwest Institute of Eco-Environment
and Resources
Lanzhou, Gansu, China

Ce Yang
Department of Bioproducts and Biosystems
Engineering
University of Minnesota
St. Paul, MN, USA

Yiannis Ampatzidis
UF/IFAS Southwest Florida Research
and Education Center
University of Florida
Immokalee, FL, USA

Jianfeng Zhou
University of Missouri
Columbia, MO, USA

Yu Jiang
School of Integrative Plant Science
Cornell University
Geneva, NY, USA

ISSN 2731-3476 ISSN 2731-3484 (electronic)
Smart Agriculture
ISBN 978-981-19-2026-4 ISBN 978-981-19-2027-1 (eBook)
https://doi.org/10.1007/978-981-19-2027-1

Contents

Chapter 1
Applications of UAVs and Machine Learning in Agriculture

Sri Charan Kakarla, Lucas Costa, Yiannis Ampatzidis, and Zhao Zhang

Abstract Farmers across the world are looking for more efficient ways to collect data about various plant physiological factors. This data collection is conventionally done using manual methods, which are time-consuming and labor intensive. Remote sensing technologies (aerial and ground based) combined with machine learning techniques can be used for high-throughput phenotyping and provide critical information for precision crop management. In this chapter, different types of unmanned aerial vehicles (UAVs) equipped with various types of sensors are presented. The advantages and disadvantages of each type of UAV and sensing system are discussed for precision agriculture applications. Furthermore, an overview of artificial intelligence algorithms is presented with examples of their usage in precision agriculture. Machine learning, which is an application of AI, is used to process and analyze data generated by these remote sensing systems. These algorithms are used for their capabilities to process complex big data to estimate plant needs and predict production.

1.1 Introduction

Unmanned aerial vehicles (UAVs) have become a great tool for various agricultural applications that helps growers across the world. UAVs are currently used for applications such as plant health and stress monitoring, pest and disease detection and management, plant phenotyping and yield estimation, etc. When compared to conventional methods and strategies, UAV based agricultural applications are

S. C. Kakarla · L. Costa · Y. Ampatzidis (✉)
Department of Agricultural and Biological Engineering, Southwest Florida Research and Education Center, University of Florida, IFAS, 2685 SR 29 North, Immokalee, FL 34142, USA
e-mail: i.ampatzidis@ufl.edu

Z. Zhang
Key Laboratory of Modern Precision Agriculture System Integration Research, Ministry of Education, China Agricultural University, Beijing 100083, China

Key Lab of Agricultural Information Acquisition Technology, Ministry of Agriculture and Rural Affairs, China Agricultural University, Beijing 100083, China

Z. Zhang et al. (eds.), *Unmanned Aerial Systems in Precision Agriculture*,
Smart Agriculture 2, https://doi.org/10.1007/978-981-19-2027-1_1

efficient, require less labor, and can cover large areas. UAVs are now commonly used in remote sensing applications for precision agriculture. With the integration of spectral sensors to the UAVs, they can sense beyond the human vision. For examples, UAVs are being used to detect and differentiate diseases that have similar visual symptoms at the early stage [1, 2]. Scouting of plants for disease detection is an essential component of integrated pest management. Visual/manual scouting is labor-intensive, expensive, requires expertise in pest identification, and the observations may be subjective and biased in terms of disease identification [3–5]. Accurate disease identification at the beginning of an outbreak is essential for the selection of effective active ingredients in spray treatments and reduces the dosage required with significant environmental and economic benefits. Diseases are currently detected in the field by visual scouting of plants and fruits. However, diagnosis based on visual symptoms is difficult due to the inability to differentiate among similar foliar symptoms of diseases. Initially, symptoms for these diseases may appear alike requiring additional confirmatory tests in a lab that could delay the diagnosis by hours or even days. UAVs equipped with sensors like hyperspectral camera can significantly reduce the time taken for this process and can also be cheaper than the traditional process [6, 7].

Tree height and canopy size measurements are other applications of the UAVs. Traditional sensing technologies for evaluation of field phenotypes rely on manual sampling and are often very labor intensive and time consuming, especially when covering large areas. Additionally, field surveys for pest and disease detection, plant inventory, and plant health assessments are expensive, labor intensive and time consuming. Small UAVs equipped with RGB (Red, Green, Blue), and multispectral sensors have recently become flexible and cost-effective solutions for rapid, precise, and non-destructive high-throughput phenotyping. UAVs equipped with RGB cameras combined with cloud-based web applications integrated with deep learning networks allow growers to constantly monitor crop health status, estimate plant water needs, detect diseases and pests, and quantify pruning strategies and impacts. UAVs equipped with LiDAR sensors are also used to monitor landscape and terrain changes in forests. There are several artificial intelligence and machine learning algorithms and platforms that have been developed in recent years that use post processed UAV data to present growers with various crop parameters, such as health conditions, canopy size and density. They can also be used to generate different maps (e.g., weed intensity, soil, and yield). In addition, UAVs can be used for spraying applications. They can be used for site specific spraying where the UAV based imagery data identifies a high-risk area affected with a disease and the UAV is programmed to be able to travel to the high-risk location and spray that specific area.

1.2 Types of UAVs

Unmanned aerial vehicles can be classified into different types based on their aerodynamic features. The four major types are (Fig. 1.1 and Table 1.1): multi-rotor, fixed-wing, single-rotor, and hybrid vertical take-off and landing (VTOL).

1. Multi-rotor UAVs: These are the most commonly used UAVs by professionals and hobbyists. They are widely used for applications like aerial photography, aerial mapping, and recreational sports. These types of UAVs are the cheapest option available in the market currently. They can be further classified into different types based on the number of rotors on the UAV: (i) Tricopter (3 rotors); (ii) Quadcopter (4 rotors); (iii) Hexacopter (6 rotors); and (iv) octocopter (8 rotors). Generally, the payload capacity increases with the number of rotors the UAV is equipped with. Compared to the low cost as the advantage, multi-rotor UAVS have several disadvantages. They have limited flight time and endurance when compared to the other types of UAVs. This is due to the fact that they need to consume a lot of energy to remain stable in air fighting against gravity and winds. The average flight time for multi-rotor UAVs ranges around 20–40 min.
2. Fixed-wing UAVs: The design of these types of UAVs are akin to regular airplanes with wings. In contrast to the multi-rotor UAVs, they do not require a lot of energy to stay in the air as they take advantage of the aerodynamic lift provided by its structure. Due to this, they can fly for a longer time compared to the multi-rotor UAVs. The average flight time for fixed-wing UAVs can last around 1–2 h. A disadvantage of these types of UAVs is that they usually need a lot of space for takeoff and landing. They also lack the ability to hover and are considered to be more complex and difficult to manipulate/operate than multi-rotor UAVs, requiring professional training. These types of UAVs also typically cost more than the multi-rotor UAVs.
3. Single-rotor UAVs: This type of UAVs looks very similar to helicopters in their design and structure. They are usually equipped with a large rotor on its top and a small rotor on its tail to control the direction of heading. These UAVs are usually powered by gas engines and therefore can fly for longer time when compared to multi-rotor UAVs (powered by rechargeable batteries). The downside of this type of UAVs is the operational dangers that comes with its large sized and more powerful rotors. They are also more difficult to fly than multi-rotor UAVs, and professional training is required. They usually cost even more than the fixed-wing UAVs but compensate for this price difference with a higher payload carrying capacity than fixed-wing UAVs.
4. Hybrid VTOL UAVs: This type of UAVs combines the advantages of fixed-wing and multi-rotors UAVs with vertical takeoff and landing capabilities. These UAVs are relatively new in the market and there are limited options available. They have a long flight time and can carry larger payloads, but the efficiency of these UAVs needs to be tested and evaluated.

Fig. 1.1 Different types of UAVs

Table 1.1 Different types of UAVs with price points and payload capabilities

Type of UAV	Price	Payload capabilities
Multi-rotor	Starts from $100	• Can hold up to 4 sensors at once • Depends on the number of gimbal spots available but can also mount using self-made mounts
Fixed wing	Starts from $1,000	• Usually, can carry 1 to 2 sensors at once • Sensors already come preinstalled in the UAV
Single rotor	Starts from $10,000	• Mostly used for spraying applications
Hybrid VTOL	Starts from $8,000	• Usually, can carry 1 to 2 sensors at once • Comes with preinstalled sensors

Types of Sensing Technologies:

1. RGB sensors

The RGB sensors are commonly referred to as visual or color cameras. They are widely used in a huge number of common devices such as cellphones, tablets, digital cameras, etc. These sensors measure the reflectance in the red, green, and blue spectrums and provide the users with a visible image. When UAVs equipped with RGB cameras are flown over large areas, they collect thousands of images, which are then stitched together using photogrammetry software to produce a map of the entire field. These maps can be used for several agricultural applications (e.g., to develop plant inventories, estimate plant leaf density and plant canopy volume) [8, 9].

2. Multispectral sensors

Multispectral sensors are an advanced version of RGB sensors, which can provide data beyond what the naked human eyes can see, and thus can capture information beyond the human vision. They provide reflectance data from the near infrared (NIR) spectrum in additional to the red, green, and blue spectrums that are usually captured by the RGB sensors. These data can be used for the calculation of several vegetation indices (VIs), among which the mostly used is the normalized difference vegetation index (NDVI). In agriculture, NDVI is measured on a scale from 0 to 1, with 0 being a stressed and 1 being a healthy plant. NDVI is being widely used by researchers to identify plant stress, predict crop yield, etc. The following is the formula to calculate NDVI:

$$NDVI = \frac{(NIR - Red)}{(NIR + Red)}$$

where Red and NIR are the spectral reflectance measurements in the red and near-infrared regions, respectively.

3. Hyperspectral sensors

The hyperspectral sensor is one of the most complex spectral sensing technologies being used in agricultural applications. It is not being as widely used as the other spectral sensors, due to very high cost of equipment and complex operating procedures. Contrary to the RGB and multispectral sensors, hyperspectral sensors collect reflectance data in continuous scans along a spectrum, usually ranging from 400 to 2,400 nm. While multispectral sensors collect reflectance data over discrete broader bands (e.g., 4–10 bands), hyperspectral sensors collect reflectance data from much narrow bands (e.g., 4–20 nm). Researchers have been using hyperspectral sensors combined with machine learning (ML) algorithms to correlate the collected reflectance data with various agricultural parameters. For example, hyperspectral sensors are being used to detect, identify, and distinguish plant diseases with similar visual symptoms, which can be a very complex task for RGB and multispectral cameras [2, 10–12].

4. Thermal sensors

Thermal sensors measure the energy radiated by an object at a wavelength (ranging from 7,000 to 12,000 nm) corresponding to its surface temperature. They can provide the users with surface temperature of various objects present in a field. Thermal cameras are widely used for precision irrigation applications. They can also be used with ML to detect leaf wetness [13] and fruits on trees [14].

5. LiDAR sensors

Light detection and ranging (LiDAR) sensors measure the distance to objects around them by illuminating the target with laser light and calculating the time required for the light to return to the sensor. LiDAR sensors have been used historically to map

Fig. 1.2 Different types of sensors outfitted to UAVs

digital elevation and surface models of the earth's surface. In agriculture, LiDAR sensors are being used for 3D modelling of the farms and farm buildings. They can also be used to measure various parameters such as crop height, crop density, canopy size, etc. Garcia et al. [15] used LiDAR data to model forest canopy height and Sankey et al. [16] used LiDAR and hyperspectral fusion for topography modelling in southwestern forests of USA, which can help monitoring landscape changes. LiDAR sensors can be used both on ground and air-based platforms for various applications (Fig. 1.2).

1.3 Examples of UAV-Based Agricultural Applications

1. Weed Mapping: Weed mapping is one of most popular applications of UAVs in precision agriculture. Weeds are undesirable plants that can grow near agricultural crops and can lead to various issues. They are competing with the crops for water, nutrients, and space, causing crop growth issues and resulting in yield loss. Since weed control is closely related to crop yield, it is very important to eliminate weeds in an agricultural field. Weed control is usually done by the use of herbicides. The most conventional spraying strategy in farming is

to spray herbicides uniformly over the entire field (blanket application), even where there are no weeds. However, this strategy may not be efficient in terms of cost and time, and also the overuse of herbicides can result in the evolution of herbicide-resistant weeds and can affect the growth and yield of the crops. In addition, indiscriminate herbicide spraying causes environmental issues (e.g., soil and water contamination) and agrochemical residues on food products. To overcome these problems, through precision agriculture practices, site-specific weed management (SSWM) is used [17]. SSWM refers to the spatially variable application of herbicides rather than spraying them in the whole field. In this context, the field is divided into management zones that each receives a customized management, as usually weed plants spread through only few spots of the field. To achieve this goal, it is necessary to generate an accurate weed cover map for precise spraying of herbicide. UAVs can gather images and derive data from the whole field that can be used to generate a precise weed cover map depicting the spots where the chemicals are needed: (a) the most; (b) the least; or (c) not at all.

2. Plant growth monitoring: UAVs are most frequently used for monitoring the growth of vegetation and providing yield estimates. For a grower to systematically monitor the progress of crop growth, there is a lot of human effort and time involved which makes it almost practically impossible. This problem is compounded by presence of diseases and pests in the fields which makes even more challenging to track the crop growth. In addition, under extreme weather conditions (e.g., rain), growers have challenges to get access to crop fields. Regular collection of information and visualization of crops using UAVs provides increased opportunities to monitor crop growth and record the variability observed in several parameters of the field. The information acquired by the UAVs can be used for the creation of three-dimensional digital maps of the crop, and for the measurement of various parameters, such as crop height, plant inter- and intra-row distance, leaf area index (LAI), etc. UAVs offer the potential to systematically collect crop information, therefore farmers can optimize crop management, such as use of inputs (e.g., nutrients, water), timing of harvest, pest and disease control, or even identify possible management errors.
3. Crop health and disease monitoring: UAVs are also used to monitor vegetation health. Crop health is a very important factor that needs to be monitored, as pests, diseases and improper/insufficient nutrients in crops can cause significant economic loss due to the reduced yield and lowered crop quality. Crops should be monitored constantly to early detect the pests and diseases and avoid spreading throughout the field. Traditionally, this task is performed by human experts who visually inspect the crop. However, this can be very time consuming, as it can require months to inspect an entire field preventing the potentials of "continuous" monitoring. Furthermore, several diseases have similar visual symptoms, which makes it difficult even for the experts to accurately detect and distinguish diseases in early stages. To overcome this challenge, remote sensing technologies, such as multispectral and hyperspectral sensors, combined with ML algorithms have been used to detect and distinguish diseases that have similar

visual symptoms. There are studies that indicate that early detection of disease (e.g., in an asymptomatic stage) is possible (e.g., [1, 18, 19]), which can help growers to timely identify disease hotspots, and thereby treating the hotspots and avoid the spread of disease to other parts of the field. NDVI is the mostly used vegetation index that has been used extensively to estimate the crop health status in large fields by using images collected from UAVs. Another common disease control method is the proactive and frequent application of pesticides. Such strategies incur a high cost and increase the likelihood of ground water contamination and pesticide residues in the products. In precision agriculture, site-specific disease control takes place. Precision agriculture practices adopt a decision-based disease management strategy, in which automated and non-destructive crop disease detection plays a very important role. Disease detection is feasible as diseases induce changes in biophysical and biochemical characteristics of the crops. UAV-based data processing technologies use crop imaging information to identify changes in plant biomass and their health. Therefore, diseases can be detected in their early stages enabling farmers to intervene in order to reduce losses. In this context, UAVs can be used in the two different stages of disease control: (a) at the initial stage of infection by collecting crop health relevant information, during which UAVs can detect a possible infection before visual indications appear and map the size of the infection to different parts of a culture; and (b) during the treatment of infection when farmers can use UAVs for targeted spraying as well as for accurately monitoring the course of their intervention.

4. Yield prediction and monitoring: The most widely adopted method for gathering information about yield and crop quality is through actual harvesting, weighing, and sorting either by human workforce or using automated machines [20–22]. For example, several automated systems were developed for yield monitoring in specialty crops, utilizing weighing systems and identification technologies [23–25]. However, the development of accurate yield estimation/prediction models is a very challenging task. Yield prediction is a critical step in defining the adequate resources, management strategies, and logistics related to the workforce, storage, packaging, and transportation [26]. UAV-based remote sensing and artificial intelligence can be used to predict crop yield [27, 28] and fruit quality [29] with an acceptable accuracy.
5. Crop spraying: An application of UAVs in precision agriculture that is more rarely met is crop spraying. The main spraying equipment used in conventional farming are the manual air-pressure and battery-powered knapsack sprayers. However, these conventional sprayers can cause major pesticide losses. In addition, the operators need to be present when spraying, which leads to exposure to biohazards. In this manner, UAVs can be useful due to the lower operator exposure and improved ability to apply chemicals in a timely and highly spatially resolved manner. The use of precision systems for measuring distances allows UAVs to follow the morphology of the ground, keeping their height constant. Therefore, an aircraft can spray the appropriate amount of herbicide spatially, adjusting both its height and the amount it sprays based on the crop site in which

it is located. Crop spraying is particularly important in cases where diseases have been identified where it is important to reduce pesticide use without affecting crop yield. In conclusion, UAV-based systems can make a decisive contribution to crop spray management.

In addition to the common applications mentioned above, UAVs have also been used for soil analysis, assessment of soil electrical conductivity, genotype selection, animal detection and management, and other applications.

1.4 Artificial Intelligence and Machine Learning

The simulation of human intelligence processes by machines, particularly computer systems, is known as artificial intelligence (AI). Expert systems, natural language processing, speech recognition, and machine vision are examples of AI applications.

Artificial intelligence systems work by learning from a massive amount of training data, analyzing the data for correlations and patterns, and then using these patterns to predict future status. By evaluating millions of samples, an image recognition technology may learn to identify and characterize objects in pictures.

The science of computer algorithms that improve automatically over experience, which has been a fundamental concept in AI research since the field's inception, is called machine learning (ML). Machine learning algorithms create a model based on sample data, referred to as "training data", in order to make predictions or judgments without being explicitly programmed.

Machine learning algorithms typically involve three main steps: learning, testing, and self-adjusting. The learning stage comes from the training data, where the computer creates a set of rules and reasoning from the data. These solutions are then compared to a testing dataset, which generates a score quantifying how good or accurate the created models are. The algorithm then uses these scores to either generate the final model if the scores are high (good) or continue training to search for better possibilities.

The application of ML in human tasks began with algorithms that mimicked the step-by-step reasoning that humans employ when solving problems or making logical inferences. Using notions from probability and economics, the earliest AI investigations devised ways for coping with uncertain or partial information. However, these methods proved insufficient for answering huge reasoning problems, as they got exponentially slower as the size of the problems increased.

Artificial neural networks, a methodology from the early machine-learning days, came and went over the decades. Neural networks are inspired by our understanding of the biology of our brains- mimicking the vast number of interconnected neurons. However, unlike a biological brain, where any neuron within a given physical distance can link to any other neuron, these artificial neural networks have discrete layers, connections, and data propagation directions.

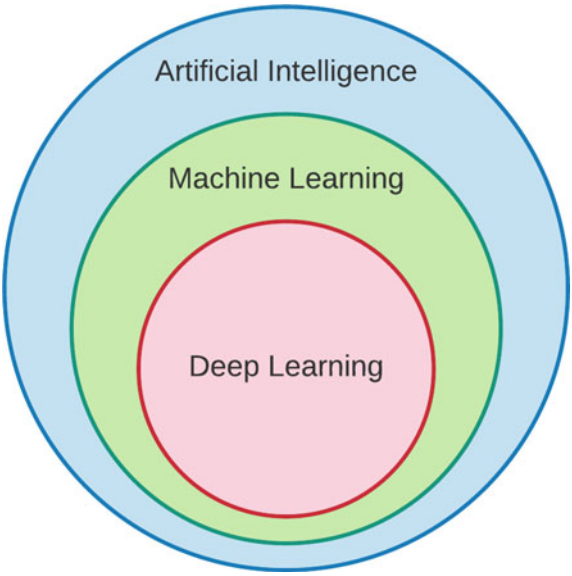

Fig. 1.3 Illustration of the relationship between artificial intelligence, machine learning, and deep learning

As the problem increased in both size and complexity, so did the size and complexity of the neural networks required to solve them. This came to a point where this approach proved to generate reliable and accurate solutions but would only be possible with a much larger amount of data and training. Deep learning is a subset of a larger family of machine learning techniques (Fig. 1.3) based on representation learning and artificial neural networks. In deep learning, the word "deep" refers to the employment of numerous layers in the network. Deep learning is a more recent form that has an unbounded number of layers of bounded size, allowing for practical application and optimization while maintaining theoretical universality under mild conditions. The simplest approach to illustrate their relationship is to see them as AI—the original idea—at the center, containing machine learning—which grew later—and ultimately deep learning—which is driving today's AI explosion (Fig. 1.3).

There are three types of learning: supervised, unsupervised, semi-supervised learning, and reinforcement learning.

Supervised learning

The major distinction of supervised learning is the presence of the labeled datasets for training. Labels identify what the observed data represents and are prepared by a human operator. They are used by the algorithm as the truth to be compared when training and testing the model. Those developing the algorithm must manually go through the dataset and apply labels to objects or features of interest. This gives developers a fair amount of control over the learning process, hence the name "supervised" learning. Through this learning process, the algorithm learns to essentially create its own labels based on the provided parameters, with the end goal being to apply the

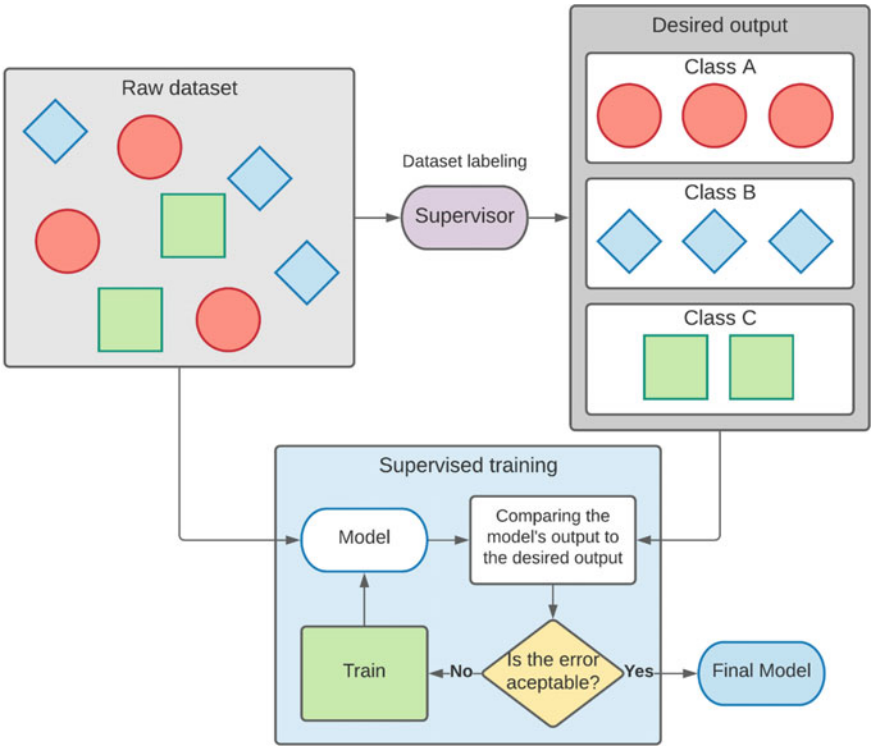

Fig. 1.4 Workflow of a supervised learning model with a supervisor labeling the raw dataset, which is used by the training algorithm to develop the model

algorithm on new, unlabeled datasets for autonomous labeling. Figure 1.4 presents the workflow of a supervised learning model training process. The main applications of supervised learning include object detection, recognition, and classification. An example of supervised learning in agriculture can be seen through the study from Varela et al. [30], where the objective of this study was to develop a method for counting corn plants based on ultra-high-resolution imagery obtained from UAVs utilizing supervised learning. To achieve this aim, an excess greenness (ExG) index was utilized to distinguish green pixels from the background, which allowed for the rows and inter-row contours to be identified and extracted. A training procedure was then implemented using geometric descriptors as inputs of the classifier. Following this, a decision tree was implemented and tested using two training modes in each site to allow the workflow to experience varying ground conditions at the time of the aerial data acquisition. For an object classification task, there was an overall accuracy of 0.96 and 0.93 acquired for local classifications based on the correctly assessed corn and non-corn objects and for the combined training modes respectively.

Unsupervised learning

In contrast to supervised learning, in unsupervised learning the provided datasets are completely unlabeled. To compensate for the lack of labels and thus foundational knowledge, much larger datasets are usually used when compared to supervised learning. Unsupervised learning is more akin to human learning than supervised learning in that it involves drawing from past experiences to augment future decisions, rather than needing to be explicitly taught everything. Because the datasets being used in unsupervised learning are unlabeled, there is less upfront manual labor required from developers to begin learning, however the results are generally less reliable than those generated from supervised learning and often require more manual labor in verification processes post-learning. Figure 1.5 presents the workflow of an unsupervised learning model process. The primary applications of unsupervised learning involve clustering datapoints by similarity, detecting anomaly datapoints, dimensionality reduction, and discovering variable associations or relationships. Common real-world examples include online shopping suggestions and credit card fraud detection systems. An example of semi-supervised learning in agriculture can be seen through the study from Shorewala et al. [31], where the aim was to estimate weed density and distribution across farmlands using only limited color images acquired from autonomous robots. To accomplish this task, the foreground vegetation pixels containing crops and weeds were first identified using a convolutional neural network (CNN) based unsupervised segmentation. Proceeding this, the weed infected regions were identified through a 'fine-tuned' CNN, which eliminated the need for manual labeling. The approach was verified through two datasets with differing crop and weed species. This method was able to localize weed-infested regions with a maximum recall of 0.99 and estimated weed density with a maximum accuracy of 82%.

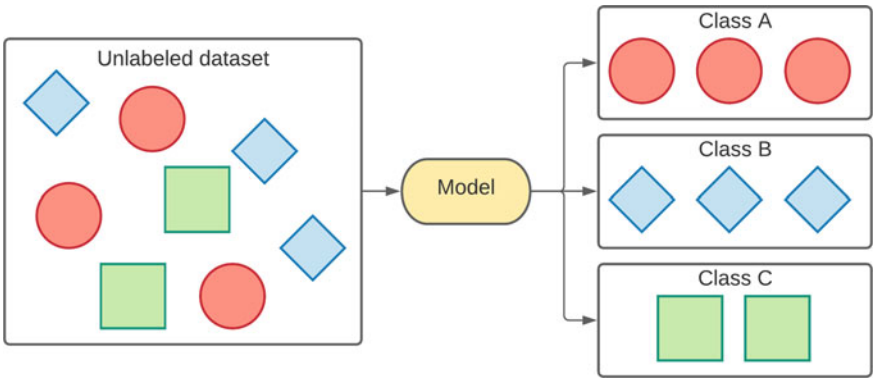

Fig. 1.5 Workflow of an unsupervised learning model differentiating 3 object classes

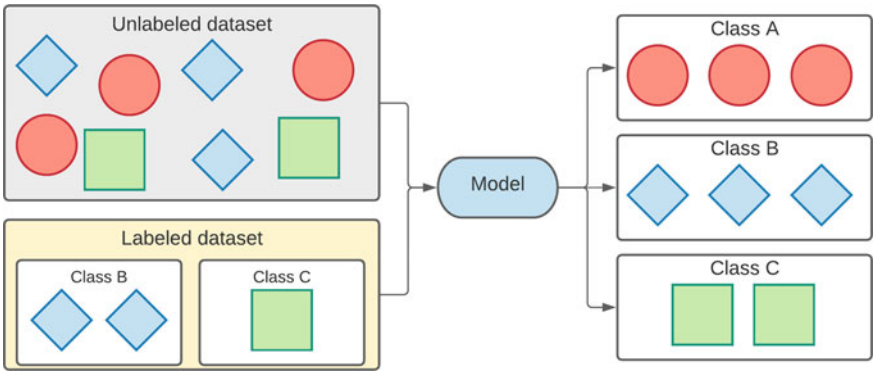

Fig. 1.6 Workflow of a semi supervised learning model using a small number of labels to better understand the dataset

Semi-supervised learning

Semi-supervised learning is a hybrid method of machine learning that benefits from the strengths of supervised and unsupervised learning, while mitigating their weaknesses. Labeled data can provide higher accuracy than inexpensive unlabeled data, however its acquisition is often labor intensive and time consuming which can render it impractical. Semi-supervised learning uses these two data types in tandem to produce a superior algorithm maintaining decent accuracy with reasonable time and cost expense. This is achieved by training a small, labeled dataset first, which provides a model capable of labeling a large, unlabeled dataset. Figure 1.6 presents the workflow of a semi supervised model process. The resulting labels are not ideal but can be used in conjunction with the initial labeled dataset to retrain the model and reduce error in the subsequent training session. An example of unsupervised learning in agriculture can be seen through De Rainville et al. [32], where the aim was to utilize supervised and unsupervised learning methods to obtain the morphological attributes of the crops and weeds present within various fields. The feature extraction process for the study was based on the spatial localization of vegetation in the fields. Features from the weed leaf area distribution were extracted from the cultivation inter-rows, which allowed for the features of the crops to be inferred from the mixture model equation. These extracted features were then passed to a naive bayesian classifier and a gaussian mixture clustering algorithm to distinguish weeds from crop plants. This technique was able to correctly classify an average of 94% of corn and soybean plants and 85% of the multiple weed species without prior knowledge on the species present in the field.

Reinforcement learning

In contrast to the other algorithms, reinforcement learning does not utilize datasets at all, and instead learns through an experimental learning environment and a scoring system from an interpreter. The interpreter is designed by the developer to understand

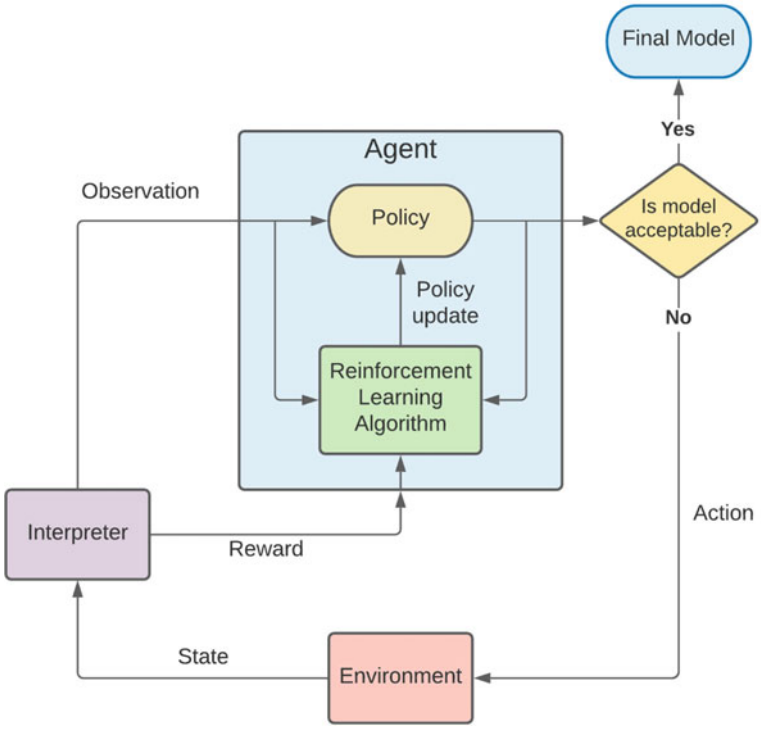

Fig. 1.7 Workflow of a reinforcement learning model training

the objective and reward scores to the model in the training stage. At the training stage the algorithm is taught to do a task through trial and error, with actions bringing the task closer to completion receiving higher scores from the interpreter. Through this positive feedback, the algorithm attempts to improve the action policy to solve the task upon positively scored actions. Figure 1.7 presents the workflow of a reinforcement learning training process. Through many iterations, the algorithm can learn to perfect a specific task based on the required specifications. This task mastery, however, is very dependent on the task environment being identical to that on which it was trained on. This type of learning is the basis of AI programs that are taught to play certain electronic games to the level of which they can defeat highly skilled human players. An example of reinforced learning in agriculture can be seen through Zhang et al. [33], where the aim was to develop a UAV that preserves battery life through sampling specific sections of a field and predicting the crop health for the whole field based on the samples obtained. Reinforcement learning (RL) and CNN were utilized to accurately and autonomously sample the field. The flight simulations were run on an aerial image dataset collected from an 80-acre corn field to develop and test the methodology. The ExG vegetation Index was utilized as the measurement for the crop health condition which was the criteria the AI was judged upon. Compared to

the conventional UAV scouting approach, which can be costly and time consuming due to the need to exchange depleted batteries multiple times, the proposed scouting approach sampled 40% of the field, predicted crop health with 90% accuracy, reduced labor cost by 4.8 times and increased agricultural profits by 1.4 times.

More use cases of UAV data combined with artificial intelligence

UAVs can be used to collect survey places that are difficult to be reached by foot, which can help increase the possibility to detect wildfires early. Gonzalez et al. [34] used thermal images and videos acquired from a UAV and applied artificial intelligence image processing using OpenCV to detect, classify, and locate wildlife in their natural habitats. The detection results from aerial data were compared to the ground data and the accuracy was 100%.

For fast and accurate plant disease detection, Sandino et al. [35] integrated hyperspectral imaging, UAVs, and machine learning algorithms to detect paperbark tea trees affected with myrtle rust. They used the spectral data acquired using UAVs and processed the data using Python programming language with the help of eXtreme Gradient Boosting (XGBoost). XGBoost is a common machine learning algorithm for complex and high dimensional data sets, such as spectral data. The detected trees were located using the Geospatial Data Abstraction Library (GDAL). The Scikit-learn third-party library was used to fine-tune the detection with statistical analyses and robust mathematical models. They were able to achieve detection rates of 97.24% for healthy trees and 94.72% for affected trees. The algorithm obtained a multiclass detection rate of 97.35%.

For livestock tracking and autonomous monitoring without attaching wearable sensors to animals (e.g., [36, 37]) used a UAV equipped with a high-resolution camera to count and track livestock animals. They used a CNN for object detection to detect and count several animal species and achieved detection accuracy rates of 97.1%. This information can be used to monitor a large number of livestock with minimal labor and discomfort to animals.

Han et al. [38] used spectral and structural information from a UAV equipped with a RGB and multispectral imaging systems. They used this information to estimate the above-ground biomass (AGB) using four machine-learning regression algorithms (e.g., multiple linear regression-MLR, support vector machine-SVM, artificial neural network-ANN, and random forest-RF). These four algorithms were evaluated and compared to create a suitable model that achieved highest accuracy rate in estimating the AGB biomass. ANN and RF models had a higher R^2 (coefficient of determination) and a lower RMSE (root-mean-square deviation), which indicates that they performed better than MLR and SVM models. R^2 and RMSE values respectively for test set are as follows: MLR (0.661,1.28), SVM (0.689,1.22), ANN (0.691,1.21) and RF (0.699, 1.2).

To expedite vegetable indices development, Costa et al. [39] created a workflow for developing agricultural indices using genetic algorithms. This study proposed a new index, vNDVI (visible NDVI), which estimates NDVI values of vegetation from uncalibrated RGB cameras mounted on UAVs (or other remote sensing platforms) with an average error of 6.89% on three crops (citrus, wheat, and sugarcane) tested.

This solution can provide effective indices to track different plant conditions while minimizing sensor costs.

For large scale grove monitoring and managing, Ampatzidis et al. [40] developed a cloud-based application to process, analyze, and visualize UAV collected data. This application can automatically create tree inventories and assess plant characteristics such as tree health, height, canopy size, and leaf density. It was found that this emerging technology detected citrus trees with mean absolute percentage error (MAPE) of 2.3% in a commercial citrus orchard with 175,977 trees (1,871 acres; 39 normal and high-density spacing blocks). Furthermore, it accurately estimated tree height with 4.5% and 13.0% MAPE for normal and high-density spacing respectively, and canopy size with MAPE of 12.9% and 34.6% for normal and high-density spacing, respectively. It provides a consistent, more direct, cost-effective, and rapid method for field survey and plant phenotyping.

To minimize labor and costs involving in plant nutrient analysis and management, Costa et al. [41] developed a gradient boosting regression trees model to estimate citrus tree leaf nutrient content based on multispectral reflectance from UAV imagery. The model was trained on Valencia and Hamlin citrus varieties. This novel methodology estimated macronutrients [Nitrogen (N), Phosphorus (P), Potassium (K), Magnesium (Mg), Calcium (ca), and Sulfur (S)] with high precision (under 15% average) and micronutrients with good accuracies (under 25% average error).

1.5 Conclusion

The use of UAVs for agricultural applications have been steadily growing, providing growers with practical information in a short time using minimal resources. There are various types of UAVs available in the market providing growers with a choice to choose a type that is best suited for their application. UAVs can also be equipped with several types of sensors such as RGB, multispectral, hyperspectral, thermal and LiDAR ranging from $500 to $30,000. The data collected from the UAVs equipped with these sensors can be processed and analyzed using various artificial intelligence techniques and machine learning models to provide growers with valuable use cases such as disease detection, nutrient management, phenotyping, inventory management, yield prediction, etc.

References

1. Abdulridha J, Ehsani R, Abd-Elrahman A, Ampatzidis Y (2019) A remote sensing technique for detecting laurel wilt disease in avocado in presence of other biotic and abiotic stresses. Comput Electron Agric 156:549–557
2. Hariharan J, Fuller J, Ampatzidis Y, Abdulridha J, Lerwill A (2019) Finite difference analysis and bivariate correlation of hyperspectral data for detecting Laurel wilt disease and nutritional deficiency in avocado. Remote Sens. 11(15):1748. https://doi.org/10.3390/rs11151748

3. Cruz A, Ampatzidis Y, Pierro R, Materazzi A, Panattoni A, De Bellis L, Luvisi A (2019) Detection of grapevine yellows symptoms in Vitis vinifera L. with artificial intelligence. Comput Elect Agricul 157:63–76
4. Cruz AC, Luvisi A, De Bellis L, Ampatzidis Y (2017a) X-FIDO: an effective application for detecting olive quick decline syndrome with novel deep learning methods. Front Plant Sci, 10 October 2017. doi:https://doi.org/10.3389/fpls.2017.01741
5. Cruz A, De Bellis L, Luvisi A, Ampatzidis Y (2017b) Vision-based plant disease detection system using transfer and deep learning. ASABE 2017, Annual International Meeting, July 16–July 19, 2017, Spokane, WA, USA, ASABE Paper No. 1700241. doi:https://doi.org/10.13031/aim.201700241
6. Ampatzidis Y, De Bellis L, Luvisi A (2017) iPathology: robotic applications and management of plants and plant diseases. Sustainability 9(6):1010. doi:https://doi.org/10.3390/su9061010
7. Luvisi A, Ampatzidis Y, De Bellis L (2016) Plant pathology and information technology: opportunity and uncertainty in pest management. Sustainability 8(8):831. doi: https://doi.org/10.3390/su8080831
8. Ampatzidis Y, Partel V (2019) UAV-based high throughput phenotyping in citrus utilizing multispectral imaging and artificial intelligence. Remote Sens 11(4):410. doi:https://doi.org/10.3390/rs11040410
9. Ampatzidis Y, Partel V, Meyering B, Albrecht U (2019) Citrus rootstock evaluation utilizing UAV-based remote sensing and artificial intelligence. Comput Electron Agric 164. https://doi.org/doi.org/10.1016/j.compag.2019.104900
10. Abdulridha J, Ampatzidis Y, Qureshi J, Roberts P (2020a) Laboratory and UAV-based identification and classification of tomato yellow leaf curl, bacterial spot, and target spot diseases in tomato utilizing hyperspectral imaging and machine learning. Remote Sens 12(17):2732. doi:https://doi.org/10.3390/rs12172732
11. Abdulridha J, Ampatzidis Y, Roberts P, Kakarla SC (2020) Detecting powdery mildew disease in squash at different stages using UAV-based hyperspectral imaging and artificial intelligence. Biosys Eng 197:135–148. https://doi.org/doi.org/10.1016/j.biosystemseng.2020.07.001
12. Abdulridha J, Ampatzidis Y, Kakarla SC, Roberts P (2020) Detection of target spot and bacterial spot diseases in tomato using UAV-based and benchtop-based hyperspectral imaging techniques. Precision Agric 21:955–978. https://doi.org/doi.org/10.1007/s11119-019-09703-4
13. Swarup A, Lee WS, Peres N, Fraisse C (2020) Strawberry plant wetness detection using color and thermal imaging. J Biosyst Eng 45(4):409–421. https://doi.org/10.1007/s42853-020-00080-9
14. Gan H, Lee WS, Alchanatis V, Abd-Elrahman A (2020) Active thermal imaging for immature citrus fruit detection. Biosys Eng 198:291–303. https://doi.org/10.1016/j.biosystemseng.2020.08.015
15. García M, Saatchi S, Ustin S, Balzter H (2018) Modelling forest canopy height by integrating airborne LiDAR samples with satellite Radar and multispectral imagery. Int J Appl Earth Obs Geoinf 66:159–173. https://doi.org/10.1016/j.jag.2017.11.017
16. Sankey T, Donager J, McVay J, Sankey JB (2017) UAV lidar and hyperspectral fusion for forest monitoring in the southwestern USA. Remote Sens Environ 195:30–43. https://doi.org/10.1016/j.rse.2017.04.007
17. Partel V, Kakarla SC, Ampatzidis Y (2019) Development and evaluation of a low-cost and smart technology for precision weed management utilizing artificial intelligence. Comput Electron Agric 157:339–350
18. Abdulridha J, Ampatzidis Y, Ehsani R, de Castro A (2018) Evaluating the performance of spectral features and multivariate analysis tools to detect Laurel wilt disease and nutritional deficiency in avocado. Comput Elect Agricul 155(Dec 2018):203–2011
19. Abdulridha J, Batuman O, Ampatzidis Y (2019) UAV-based remote sensing technique to detect citrus canker disease utilizing hyperspectral imaging and machine learning. Remote Sens 11(11):1373
20. Ampatzidis YG, Vougioukas SG (2009) Field experiments for evaluating the incorporation of RFID and barcode registration and digital weighing technologies in manual fruit harvesting. Comput Electron Agric 66(2):166–172

21. Ampatzidis YG, Vougioukas SG, Bochtis DD, Tsatsarelis CA (2009) A yield mapping system for hand-harvested fruits based on RFID and GPS location technologies: field testing. Precision Agric 10(1):63–72
22. Ampatzidis YG, Vougioukas SG, Whiting MD (2011) A wearable module for recording worker position in orchards. Comput Electron Agric 78(2):222–230. https://doi.org/10.1016/j.compag.2011.07.011
23. Ampatzidis YG, Whiting MD, Liu B, Scharf PA, Pierce F (2013) Portable weighing system for monitoring picker efficiency during manual harvest of sweet cherry. Precision Agric 14(2):162–171
24. Ampatzidis YG, Whiting MD, Scharf PA, Zhang Q (2012) Development and evaluation of a novel system for monitoring harvest labor efficiency. Comput Electron Agric 88:85–94
25. Ampatzidis YG, Wortman R, Tan L, Whiting M (2016) Cloud-based harvest management information system for hand-harvested specialty crops. Comput Electron Agric 122:161–167
26. Ampatzidis YG, Vougioukas SG, Whiting MD, Zhang Q (2014) Applying the machine repair model to improve efficiency of harvesting fruit. Biosyst Eng 120(April 2014):25–33
27. Apolo-Apolo OE, Martínez-Guanter J, Egea G, Raja P, Pérez-Ruiz M (2020) Deep learning techniques for estimation of the yield and size of citrus fruits using a UAV. Eur J Agron 115. https://doi.org/10.1016/j.eja.2020.126030
28. Vijayakumar V, Costa L, Ampatzidis Y (2021) Prediction of citrus yield with AI using ground-based fruit detection and UAV imagery. 2021 Virtual ASABE Annual International Meeting, July 11–14, 2021, ASABE Paper No. 2100493, doi:https://doi.org/10.13031/aim.202100493
29. Ojo I, Costa L, Ampatzidis Y, Shukla S (2021) Citrus fruit maturity prediction utilizing UAV multispectral imaging and machine learning. 2021 Virtual ASABE annual international meeting, July 11–14, 2021, ASABE Paper No. 2100495, doi:https://doi.org/10.13031/aim.202100495
30. Varela S, Dhodda PR, Hsu WH, Prasad PVV, Assefa Y, Peralta NR, Griffin T, Sharda A, Ferguson A, Ciampitti IA (2018) Early-season stand count determination in corn via integration of imagery from unmanned aerial systems (UAS) and supervised learning techniques. Remote Sens 10:343. https://doi.org/10.3390/rs10020343
31. Shorewala S, Ashfaque A, Sidharth R, Verma U (2021) Weed density and distribution estimation for precision agriculture using semi-supervised learning. IEEE Access 9:27971–27986. https://doi.org/10.1109/ACCESS.2021.3057912
32. De Rainville FM, Durand A, Fortin FA et al (2014) Bayesian classification and unsupervised learning for isolating weeds in row crops. Pattern Anal Applic 17:401–414. https://doi.org/10.1007/s10044-012-0307-5
33. Zhang Z, Boubin J, Stewart C, Khanal S (2020) Whole-field reinforcement learning: a fully autonomous aerial scouting method for precision agriculture. Sensors 20:6585. https://doi.org/10.3390/s20226585
34. Gonzalez L, Montes G, Puig E, Johnson S, Mengersen K, Gaston K (2016) Unmanned aerial vehicles (UAVs) and artificial intelligence revolutionizing wildlife monitoring and conservation. Sensors 16(1):97. https://doi.org/10.3390/s16010097
35. Sandino J, Pegg G, Gonzalez F, Smith G (2018) Aerial mapping of forests affected by pathogens using UAVs, hyperspectral sensors, and artificial intelligence. Sensors 18(4):944. https://doi.org/10.3390/s18040944
36. Chamoso P, Raveane W, Parra V, González A (2014) UAVs applied to the counting and monitoring of animals. In *Ambient Intelligence—Software and Applications*, pp 71–80, Springer International Publishing
37. Nunes L, Ampatzidis Y, Costa L, Wallau M (2021) Horse foraging behavior detection using sound recognition techniques and artificial intelligence. Comput Electron Agric 183. https://doi.org/doi.org/10.1016/j.compag.2021.106080
38. Han L, Yang G, Dai H, Xu B, Yang H, Feng H, Li Z, Yang X (2019) Modeling maize above-ground biomass based on machine learning approaches using UAV remote-sensing data. Plant Methods 15(1). doi:https://doi.org/10.1186/s13007-019-0394-z

39. Costa L, Nunes L, Ampatzidis Y (2020) A new visible band index (vNDVI) for estimating NDVI values on RGB images utilizing genetic algorithms. Comput Elect Agricul 172:105334
40. Ampatzidis Y, Partel V, Costa L (2020) Agroview: cloud-based application to process, analyze and visualize UAV-collected data for precision agriculture applications utilizing artificial intelligence. Comput Elect Agric 174:105457
41. Costa L, Kunwar S, Ampatzidis Y, Albretch U (2021) Determining leaf nutrient concentrations in citrus trees using UAV imagery and machine learning. Precision Agric. https://doi.org/10.1007/s11119-021-09864-1

Chapter 2
Robot Operating System Powered Data Acquisition for Unmanned Aircraft Systems in Digital Agriculture

Yu Jiang

Abstract Unmanned aircraft systems (UAS) have been popularized recently for agricultural applications. While many commercial and open-source solutions have been and are being developed, limited efforts have been made for custom data acquisition systems which are crucial to address major technical issues in the current UAS systems for agriculture. This chapter aims to provide a conceptual framework based on robot operating system (ROS) for the design and development of custom data acquisition (DAQ) systems for UAS in agriculture. Design concepts and major implementation details are provided to facilitate future development. A case study is given in this chapter to demonstrate the use of the conceptual framework to design and implement a ROS-based data acquisition system for a commercial drone. The case study also demonstrated the success of the developed system for image acquisition in a hemp breeding experiment and the value of using UAS sensing systems for high throughput phenotyping in hemp. Therefore, the proposed conceptual framework can be used as a reference to develop custom DAQ systems in future studies.

2.1 Introduction

Agriculture is facing tremendous challenges caused by the continuously growing world population along with major environmental [13] and social issues [19] such as climate change [12], limited arable land and water resources [24], and labor shortage [39]. Past efforts have focused on addressing specific issues: the Green Revolution aimed for yield increases but not resource use efficiency; agricultural mechanization revolution aimed for productivity but not pollution and environmental consequences; and precision agriculture aimed for optimal return over investment but not equity. The new digital agriculture (DA) revolution aims to digitize the whole supply chain of agrifood systems and provides systems solutions to massive aforementioned challenges [2].

Y. Jiang (✉)
Cornell University, 635 W North St. Geneva, New York, United States of America 14456
e-mail: yujiang@cornell.edu

Z. Zhang et al. (eds.), *Unmanned Aerial Systems in Precision Agriculture*,
Smart Agriculture 2, https://doi.org/10.1007/978-981-19-2027-1_2

Unmanned aircraft systems (UAS), or drones in many recent research studies, are a key DA component that offers mobility to sensing and actuation operations for agricultural applications [1, 9, 14, 18, 32, 35]. Based on the driving-mode, UAS platforms can be categorized as three groups: (1) single-rotors, (2) multirotors, and (3) fixed-wing platforms [14]. Single-rotors (e.g., helicopters) and fixed-wing platforms have been widely used in remote sensing and spraying in agriculture for a long time [35]. Due to improved operability, reduced cost, and sufficient market availability, multirotors have been recently popularized for both agricultural research and production management, especially for high throughput plant phenotyping [9, 35]. Compared with other mobile platforms (e.g., ground and satellite systems), multirotors offer a unique balance between sensing coverage and resolution. Typically, a multirotor-based system has a flight duration of 20 to 30 minutes, which can cover up to 100 acres with a sensing resolution at the millimeter to centimeter (or organ to plot) levels [29, 30, 37]. This throughput and resolution combination would be sufficient for plant- and plot-level research studies and breeding as well as decision-making support in production systems. Depending on the sensing modules (e.g., RGB, multi/hyper-spectral imaging, thermal imaging, and LiDAR) used, UAS-based systems have demonstrated success in measuring traits related to plant morphology (e.g., plant height and volume) [17, 21], physiology [10], stresses [1], crop yield [15, 38], and crop quality [27, 33]. Particularly, many off-the-shelf UAS-based systems have been well integrated with RGB, multi-/hyper-spectral, and thermal imaging modules, which allow non-engineering experts to readily utilize these new tools for collecting needed raw data in research fields and production farms [14, 29, 35]. Therefore, recent interests and efforts have been concentrated on the development of data analytical methodologies and processing pipelines to extract and interpret important crop traits from raw data collected by UAS systems, leading to new biological and agronomic findings and precision management practices. On the other hand, two major engineering needs have been identified for UAS in agriculture: (1) multimodal sensing UAS for agricultural applications and (2) coordinated multi-agent UAS for agricultural sensing [14]. The two needs are related to the design of UAS control and data acquisition.

A large body of literature has focused on the design and control of quadcopters, a representative multirotor, because of the dynamics and diverse military and civilian applications [3, 11, 20, 23]. The control and mechatronics of multirotors (or other types of UAS) are continued research topics, but recent interests have shifted towards multi-agent UAS control [4, 28, 31], operation safety [22], and visualization [22, 34]. The design and control of quadcopters have been gradually formalized in the past decade, which has led to two main options: (1) commercial products via representative manufacturers such as DJI Inc. and (2) open-source solutions via large community supports such as PX4 Autopilot. Both options provide software development kit (SDK) and/or predefined interfaces to enable the customization of UAS systems for various domain applications such as digital agriculture. The key difference between the two options is the balance between guaranteed performance and modification flexibility. Development of data acquisition system for UAS (especially multirotors) has been largely overlooked because of well-integrated commercial products and/or

the use of single sensors. Most studies on the development of UAS data acquisition system have reported custom computer programs to control a particular instrument, which lacked the expandability to new sensors with different hardware/software interfaces [7, 8]. Several pioneering attempts, however, have reported the design of new data acquisition system for UAS with either flexible control synchronization [6, 25] and/or multimodal sensing capabilities [16, 36]. In particular, two of them reported the use of robot operating system (ROS)-based solutions [6, 36]. A major limitation of the two studies is the lack of an abstract framework to guide the design and development of ROS-based data acquisition systems which enable multimodal and multi-agent UAS sensing in future agricultural applications.

This chapter aims to provide a conceptual framework for the design and development of a ROS-based data acquisition system for UAS systems in digital agriculture. Basic concepts of ROS components and examples of using ROS for both commercial and open-source UAS systems are provided. A case study of using the proposed framework is presented for an industrial hemp research. Future development and potential applications are also discussed.

2.2 ROS-Based Data Acquisition System

2.2.1 Basic Concepts and Components in ROS

ROS is an open-source middleware for robots and provides a collection of libraries of fundamental functions for robot development [26]. Although ROS is not an actual operating system (OS), it provides OS-level functions such as hardware abstraction, low-level device control, commonly used functions, message-passing between processes, and stable package management. There are three levels of concepts in ROS: file system, computation graph, and community. While all three are important for the ROS ecosystem, the computation graph level is the focus in this chapter because it is directly related to the development of a ROS-based data acquisition system.

In the runtime, ROS builds a computation graph that enables peer-to-peer connections among individual processes via the ROS communication mechanism (Fig. 2.1). There are three types of communications in ROS: (1) synchronous remote procedure call (RPC), (2) asynchronous data streaming, and (3) global data storage and sharing. The communication approaches are implemented by using various ROS computation graph components which should be briefly introduced prior to the design and development of ROS-based data acquisition. The basic components in a ROS computation graph include Node, Service, Master, Parameter Server, Topic, Message, and Bag.

Node: Nodes are the basic computational processes in ROS. A ROS program usually comprises a collection of nodes with each being dedicated for a particular function to achieve a fine-grained modularity. For instance, a node can be developed to interface with an encoder for robot control uses. All nodes are typically connected via the asynchronous data streaming (publisher-subscriber scheme) to form a com-

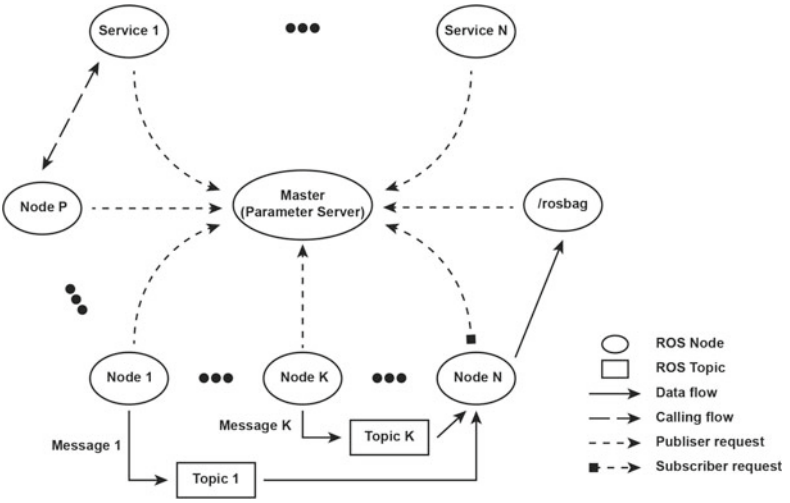

Fig. 2.1 Diagram of key ROS components and their potential connections in a ROS computation graph. It should be noted Node and Service are both processes but use different communication schemes. ROS Master is a naming and registration service to allow the rest nodes and services to identify each other and Parameter Server is a part of ROS Master. Rosbag is the default ROS package to save and retrieve information (e.g., raw data, timestamp, etc.) in the ROS Bag format

putation graph for robot operations such as sensor control and data acquisition. ROS provides two client libraries for the implementation of nodes in C++ (roscpp) and Python (rospy).

Services: Services can be considered as nodes but are defined by a node pair with one for requesting and one for replying. Compared to the publisher-subscriber scheme for one-way communication, the request-reply scheme used by services offers two-way interactions between the paired nodes. This is particularly useful for RPC-style control. It should be noted that one node can advertise multiple services.

Master: The ROS Master is a special service for name registration and identification for the rest nodes and services in a ROS computation graph. Nodes and services should be registered in ROS Master prior to use. Otherwise, they can not be correctly identified and invoked.

Parameter Server: The Parameter Server is a central location in which data are stored by key for global access. Currently, the Parameter Server is a part of the ROS Master for use.

Messages: Messages are simply data structures consisting of fields with various data types. ROS messages support standard primitive types (e.g., integer, floating

point, boolean, etc.), arrays of primitive types, and arbitrarily nested structures and arrays. This is very similar to the structs in C programming language.

Topics: Topics are the transportation channels for the publisher-subscriber communication scheme. When they are communicated between nodes, messages are sent out by a publisher node to a topic and then disseminated to all nodes that subscribe to that topic. There is no restriction on the number of topics a node can publish to nor subscribe from. The same topic can also accept multiple publisher nodes concurrently. Thus, topics can be considered as input/output (I/O) buses to support low-latency, many-to-many communications and decouple information production and consumption. This will be particularly useful for data acquisition systems because data streaming errors in one sensor (or one node) would not affect the entire system.

Bags: Bags are a ROS format for message (or data in a general context) storage and retrieval. ROS provides the rosbag package with key functionalities including data recording, bag meta information check, retrieval of (or play back) collected bags, bag compression/decompression, bag file repairing, and so on. It should be noted that rosbag package does not provide a caching mechanism which might be necessary for high-speed, high data volume sensors.

2.2.2 Connecting with Other UAS Components

As a mobile platform, the data acquisition system of a UAS needs communications with the control system of that UAS to coordinate data collection with flight operations. Currently, most UAS platforms use either the DJI control system or Pixhawk-series controllers from PX4 Autopilot. The two control systems have their own ecosystems with different preferred features and development requirements, but both support ROS for secondary development.

The DJI development ecosystem provides an option with a well-integrated ROS environment such as the DJI onboard software development kit (OSDK) (Fig. 2.2). The DJI OSDK provides high-level ROS nodes to communicate with the drone and associated payloads such as cameras and gimbals that follow DJI protocols. These high-level ROS nodes can be used for time synchronization, obtaining drone status, flight control, motion planning, information management, and so on. Additionally, the OSDK also provides interfaces with other DJI SDKs such as payload SDK and mobile SDK for better system integration and development. Since the OSDK ROS is naturally built upon a specific ROS distribution (or version), it supports all packages for that ROS distribution as well. Therefore, a data acquisition system can be quickly developed and integrated with DJI drones for custom data collection needs. For instance, continuous data collection would be configured for imaging sensors (e.g., RGB cameras) with a high shutter speed, whereas a ‘stop-acquire-go’ mode would be set for point-based sensors (e.g., spectrometers) that need a hover for repeated measurements and/or an extended long exposure.

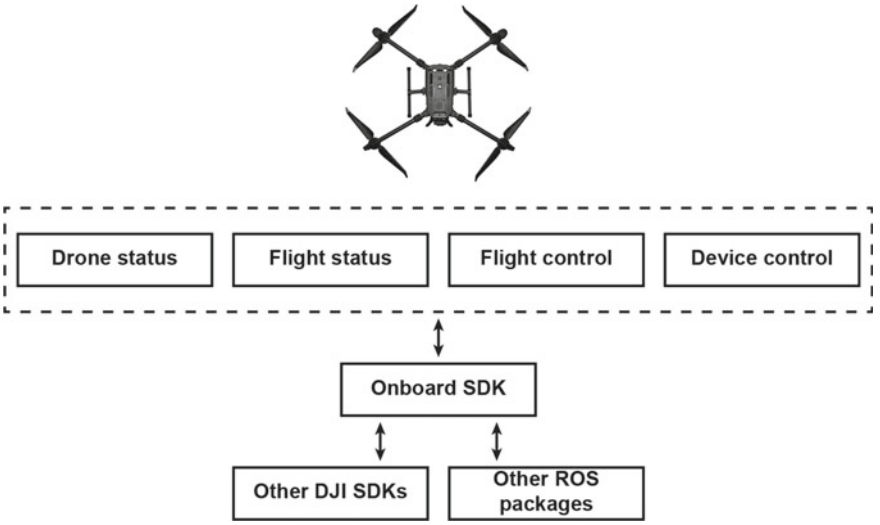

Fig. 2.2 Diagram of the DJI Onboard SDK (OSDK) and interfaces to other SDKs and ROS packages. Functions in the dashed-line rectangle are high-level ROS nodes in the DJI OSDK for drone information acquisition, flight status check, and flight and payload controls. Other DJI SDKs include mobile SDK for embedded systems (e.g., Androids and Apple iOS) and payload SDK for DJI-certified accessories and sensors (e.g., gimbals and cameras). DJI offers a version of OSDK built upon ROS and naturally supports all ROS packages for development

The PX4 Autopilot ecosystem offers a full-stack solution consisting of open-standard hardware controllers (i.e., Pixhawk-series controllers) and open-source control software (i.e., PX4) and ground station (i.e., QGroundControl) (Fig. 2.3). The PX4 control library is designed for all types of unmanned vehicles and provides more functionalities. For drone-related functionalities, PX4 is very similar to the DJI counterpart. Compared with the DJI OSDK, PX4 is not built upon ROS but has robotics application programming interfaces (APIs) to support the use of common robotics libraries such as ROS. It is noteworthy that PX4, as an open-source community solution, tends to be forward-looking and recommends either MAVSDK, the library from the PX4 Autopilot ecosystem, or ROS2, the newly-designed ROS system with new features such as the support of realtime operations. PX4 still supports ROS for the compatibility consideration. Therefore, a ROS-based data acquisition system can be used interchangeably between the two UAS ecosystems. Some minor modifications might be needed to accommodate differences due to various ROS distributions.

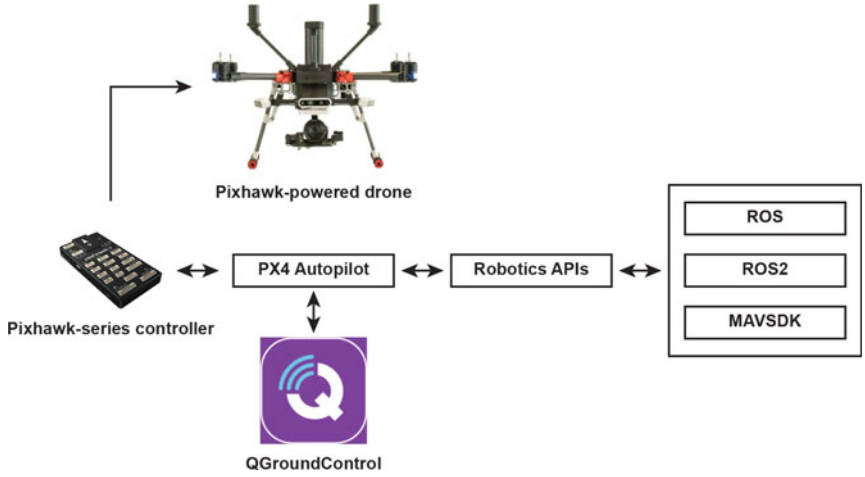

Fig. 2.3 Diagram of the PX4 Autopilot ecosystem including PX4, Pixhawk-series hardware controllers, and QGroundControl ground station. PX4 is a stack of autopilot control functions (i.e., software) for unmanned aerial, ground, and marine vehicles. PX4 provides robotics application programming interfaces (APIs) to facilitate the development of any PX4-powered robots for domain applications without considering all design details. Compared with the DJI ecosystem, PX4 Autopilot ecosystem supports more robot middlewares such as ROS, ROS2, and MAVSDK

2.2.3 Examples for Representative Sensors

UAS systems can carry a wide range of sensors. Based on the sensing principles, sensors can be categorized as optical, electrical, mechanical, acoustic, and so on. Based on the sensing modes, sensors can be grouped as imaging sensors (e.g., RGB, multi-/hyper-spectral, thermal cameras) and point-based sensors (e.g., spectrometers, environment sensors, and volatile organic compounds (VOC) sensors). From the data acquisition perspective, all these sensors can be divided into two categories: sensors have onboard data acquisition and sensor have no onboard data acquisition. The two types of sensors need different designs for ROS-based data acquisition.

Sensors without onboard data acquisition: Many commonly used sensors (e.g., spectrometers and industrial cameras) do not provide onboard data acquisition support because of the design complexity and cost requirements. Integrating these sensors need a data acquisition system not only perform sensor control but also data transfer from a sensor to a UAS-companion computer for storage, process, and visualization. As data streaming is needed and data transfer can be non-synchronized, ROS Node is the most proper option (Fig. 2.4). One node should be developed to control one sensor including sensor initialization, data streaming (i.e., topic registration and publishing), and error handling. A finite state machine (FSM) has been proposed to streamline important events that a sensor node should consider implementing in practice (Fig. 2.5). The key of implementing this state machine for a sensor node is to

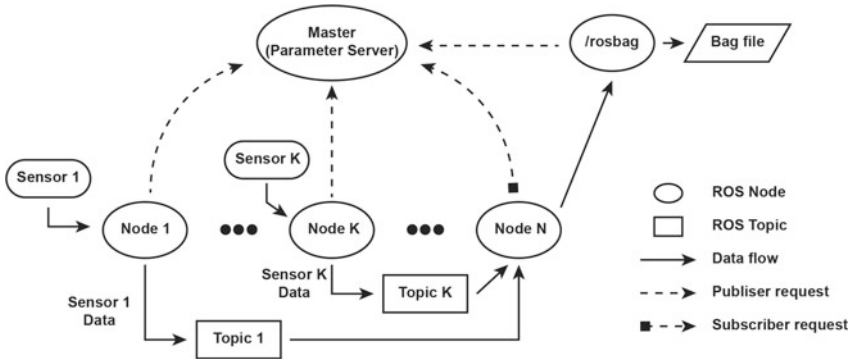

Fig. 2.4 Diagram of a ROS-based data acquisition system with sensor nodes. Each sensor node controls a single sensor for initialization, data streaming, and error handling. Typically, a separate node needs to be developed to subscribe all sensor nodes to gather information together and use the rosbag package for data serialization

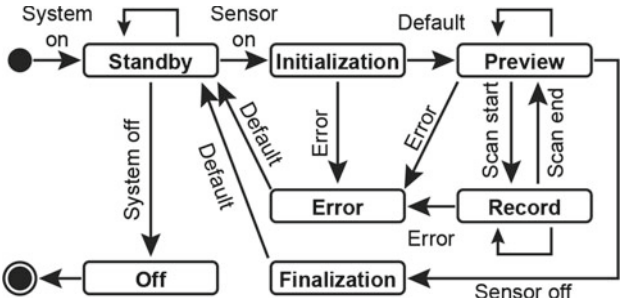

Fig. 2.5 Concept of the finite state machine (FSM) developed for sensor nodes and services to be used in a ROS-based data acquisition system. It should be noted that the implementation of a sensor node and service will be different because of the difference in their communication schemes. A sensor node needs to automate the entire state machine due to the one-way communication, whereas a sensor service can be designed to provide interactive responses to maximize human operator's involvement, especially for error handling

fully automate the state transition based on sensor responses because no interaction will occur with human operators.

An advantage of ROS for data collection is the rosbag library which provides functions in data recording, visualization, check, filtering, compression/decompression, and repairing. However, rosbag does not provide any caching option to accommodate data volume differences among sensors, I/O buses, computer memory, and external storage (e.g., hard drives). Thus, special design needs to be accomplished by developers to avoid potential memory-related issues such as memory leak for sensors with high sampling frequency and data volume.

Sensors with onboard data acquisition: Advanced sensors such as hyperspectral and multimodal cameras usually provide this option to improve data I/O efficiency

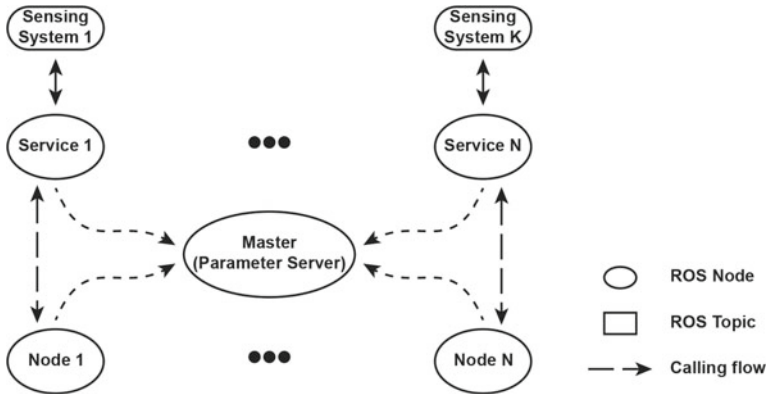

Fig. 2.6 Diagram of a ROS-based data acquisition system with sensor services. Each sensor service communicates with a single sensor via provided sensor control APIs. A corresponding client sensor node needs to be developed to invoke the service for RPC-style sensor control and data collection. Since no data are streamed back to the ROS-based data acquisition system, raw data will be saved in a format predefined by the sensor manufacturer in the onboard device. Also, data visualization through the same ROS environment is non-trivial and may require careful considerations in I/O bandwidth

and overall reliability. Compared with sensors without onboard data acquisition, key differences are (1) data streaming from a sensor to a UAS-companion computer is no long needed and (2) an interactive request-reply communication is required to ensure successful command communications and executions between a sensor and a computer. Therefore, ROS Service is the most proper option (Fig. 2.6). A replying node needs to be developed to communicate with a sensor via APIs provided by the sensor's manufacturer, and a client sensor node needs to be developed to invoke the replying node for various functions. The replying node can register multiple services with each being used for one control function of the sensor, so that the client node can implement the proposed FSM for handling various events based on the sensor running status. No sensor data are transferred from the sensor back to the UAS companion computer, presenting two challenges in the ROS-based data acquisition system. First, raw sensor data will be saved in a format predefined by the sensor manufacturer and may have different meta data information (especially timestamp). A viable solution is to save the ROS timestamp when the data collection request will be confirmed by the sensor service, so that data collected on this sensor can be co-registered with data collected on other sensors and in the UAS companion computer. Second, data visualization through the ROS system will be challenging. An alternative solution is to develop a separate visualization interface to directly visualize data from the sensor's onboard system.

2.3 A Case Study for Industrial Hemp Phenotyping

2.3.1 UAS Data Acquisition System

A custom UAS system was developed by integrating a DJI Matrice 100 platform with a Zenmuse 3 RGB camera (DJI, Shenzhen, China) and a MicaSense RedEdge five-band multispectral sensor (1280×960 px) (MicaSense Inc., Seattle, WA, USA). Based on the framework introduced in the previous section, a ROS-based data acquisition system was implemented to control the two cameras for continuous image collection during a flight. The RGB camera was controlled by using a sensor node and images were saved in ROS bag files, whereas the multispectral camera was controlled by using a sensor service and images with meta data were saved in the onboard SD cards.

2.3.2 Plant Materials and Experimental Design

An experiment was conducted to study the plant morphology contribution to biomass and cannabinoid yield for industrial hemp [5]. Hemp seeds were sown into deep 50-cell Sureroots trays with potting mix (LM111, Lambert, Rivière-Ouelle, QC, Canada) in the greenhouse with supplemental lighting with a 16:8 h light:dark regimen, 3 weeks before planting in the field at Cornell AgriTech (Geneva, NY, USA). The common parent, 'TJ's CBD', was planted from cuttings, but grown in the same greenhouse conditions as the seedlings. Cuttings were rooted using Clonex Rooting Gel (Hydrodynamics Intl., Lansing, MI, USA). At the time of planting (16 June 2020), 15 progeny individuals were randomly selected from each family, and planted together in single plots at 1.2 m spacing within a row and 1.8 m spacing between rows. Granular fertilizer (19-19-19, N-P-K) was incorporated at 95 kg/ha before raised beds with plastic mulch were built. Drip irrigation was installed under plastic mulch. Landscape fabric was installed in aisles to suppress weed pressure. Soil moisture sensors (HOBOnet 10HS, Onset Computer Corp, Bourne, MA, USA) were randomly installed across the field to aid in timing of irrigation. The field was fertigated twice through a Dosatron (Dosatron Intl., Inc., Clearwater, FL, USA) 4 and 6 weeks after planting, using Jack's 12-4-16 Hydro FeED RO (J.R. Peters Inc., Allentown, PA, USA).

2.3.3 Data Acquisition and Ground-Truth Measurements

The developed UAS system was flown 10 times during the growing season using the DroneDeploy App version 2.90.0 (DroneDeploy, Sydney, Australia). Flights were completed at 10 d intervals from 15 days after planting (DAP) to 93 DAP, with an

altitude of 20 m and 80% front and side overlap. Ground sampling distances for the Zenmuse 3 and RedEdge were 0.86 cm/pixel and 1.39 cm/pixel, respectively. Ground control points were manually surveyed utilizing a real-time kinematic Trimble R8s GPS (Trimble Inc., Sunnyvale, CA, USA), and used to georectify the reconstructed data in the universal transverse mercator coordinate system for successive analyses. Field assessment trials were performed to manually collect ground-truth data related to floral phenology, hemp stem growth and canopy morphology, chlorophyll concentration, and biomass [5].

2.3.4 Data Processing Pipeline for Extracting Morphological and Vegetation Traits

A data processing pipeline was developed to analyze collected aerial images for the extraction of morphological and vegetation index traits (Fig. 2.7). Collected color and multispectral images were retrieved from bag files and SD cards and then processed using Metashape Pro version 1.6.0 (Agisoft LLC, Russia) to reconstruct color and multispectral orthoimages and colorized 3-D point clouds. Plant geo-locations were calculated using color orthoimages. A color orthoimage was converted to an excessive green index map then binarized using the Otsu method. Connected component labeling was used to segment individual plants and calculate their center locations. Based on plant centers, bounding boxes of 1.83 m (across row) and 1.22 m (within row) were generated for the localization and segmentation of plants in point clouds and multispectral orthoimages. A significant shift of plant centers was observed between 23 and 34 DAP, so the plant geo-locations and bounding boxes were derived from the color orthoimages on the two days, respectively. The locations and bounding boxes calculated on 23 DAP were used to analyze the data collected on 23 DAP, and those calculated on 34 DAP were used for the rest of data.

In the colorized point clouds, the point cloud of each plant was cropped using the calculated bounding boxes. Random sample consensus (RANSAC) was used to identify the ground plane in the plant point cloud (red points in Fig. 2.7) and separate canopy points (green points in Fig. 2.7) for the extraction of canopy morphological traits: height, projected area, and volume. In the multispectral orthoimages, a circular region with a radius of 0.28 m was defined at each plant center, and seven vegetation indices were calculated using pixels within the region for a corresponding plant. The seven vegetation indices comprise the normalized difference vegetation index (NDVI), enhanced vegetation index (EVI), green chlorophyll index (GCI), green normalized difference vegetation index (GNDVI), modified non-linear index (MNLI), modified soil adjusted vegetation index 2 (MSAVI2), and optimized soil adjusted vegetation index (OSAVI).

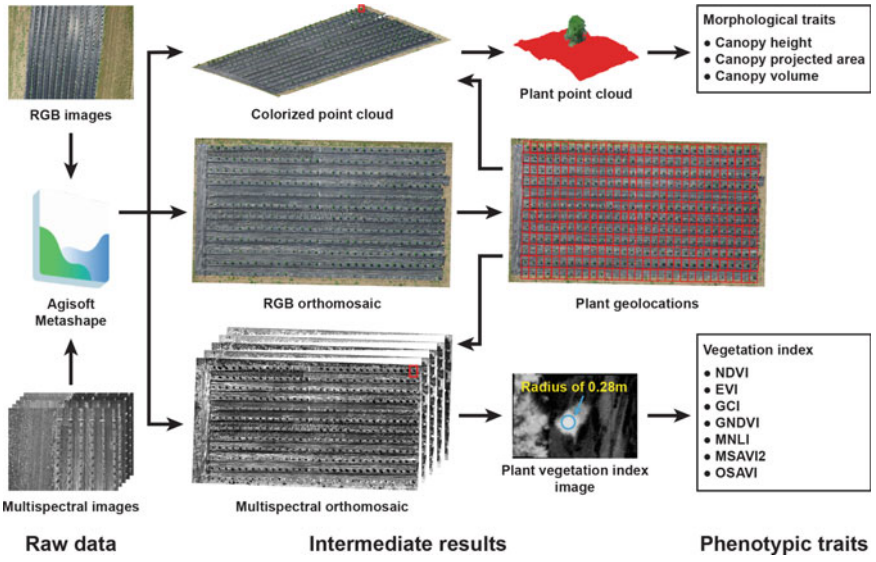

Fig. 2.7 Data processing pipeline for the extraction of phenotypic traits from RGB and multispectral data. Derived vegetation indices include normalized difference vegetation index (NDVI), enhanced vegetation index (EVI), green chlorophyll index (GCI), green normalized difference vegetation index (GNDVI), modified non-linear index (MNLI), modified soil adjusted vegetation index 2 (MSAVI2), and optimized soil adjusted vegetation index (OSAVI)

2.3.5 Measurement Accuracy

There were dramatic differences in morphological HTP aerial measurements (canopy height, area, and volume) between flights flown before and after 56 DAP, with good correlations among measurements within but not among earlier and later flights. These differences were due to a strong windstorm between 50 DAP and 56 DAP that resulted in moderate lodging and stem breakage. Even though F1 families were planted in rows, a family-level analysis did not have a major effect on HTP to field phenotypic correlations of later flights (Fig. 2.8). Canopy height and volume obtained from orthomosaic mesh layers were well correlated with corresponding field-collected phenotype plot height (r=0.83) and kite volume (r=0.67) for early flights. Family-level correlations were even stronger for height (r=0.95) and volume (r=0.80). Biomass yield was most associated with canopy volume (35 DAP) (r=0.56), yet this correlation was only marginally improved on a family mean basis and, for all aerial surveys beyond 50 DAP, there were only weak correlations between the two.

Instances of lodging did not affect vigor or productivity but confounded the accuracy of morphological indices after 56 DAP because of alterations in the primary axis and projected area of individual plots. Physiological indices were likewise affected, but not as profoundly as the morphological indices (Fig. 2.9). There were good phenotypic correlations with nearly all HTP measurements except EVI, which

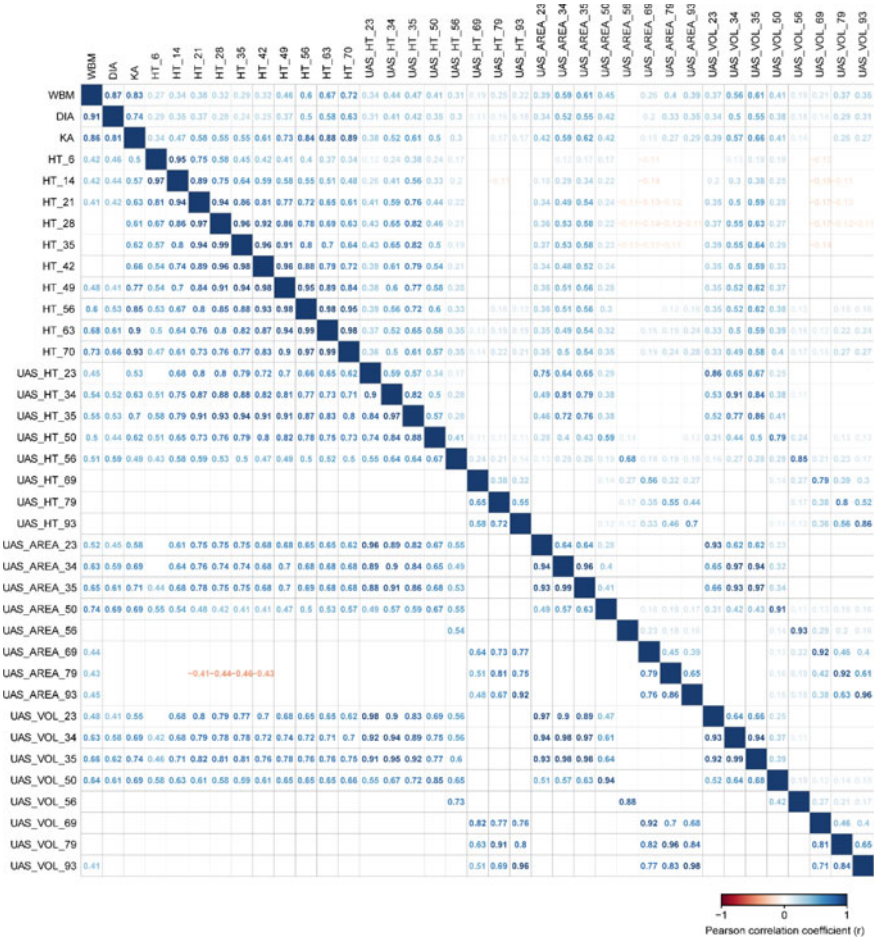

Fig. 2.8 Pairwise correlations of field collected traits with aerial morphological indices on a plot-level (upper triangle) and family-level (lower triangle) basis. The color of coefficients within cells represent significant ($p < 0.01$) positive (blue) or inverse (red) correlations. WBM, DIA, KA, HT, AREA, VOL are for total wet biomass, basal stem diameter, kite branch angle, plant height, plant canopy area, and plant canopy volume, respectively. UAS prefix indicates traits measured using the UAS system

was not informative. Notably, we observed that few cannabinoids were associated with physiological indices (Fig. 2.10). The strongest were in the abundance of the minor cannabinoids cannabicyclol (cannabicyclol; r = –0.35) and cannabidivarin (cannabidivarin; r = –0.17) with MNLI, MSAVI2, and OSAVI at 93 DAP, but those with cannabidivarin may be due to population structure, since only two families had individuals with >1% cannabidivarin content. It may be possible to predict cannabinoid profiles and yield using multispectral or hyperspectral data, similar to what

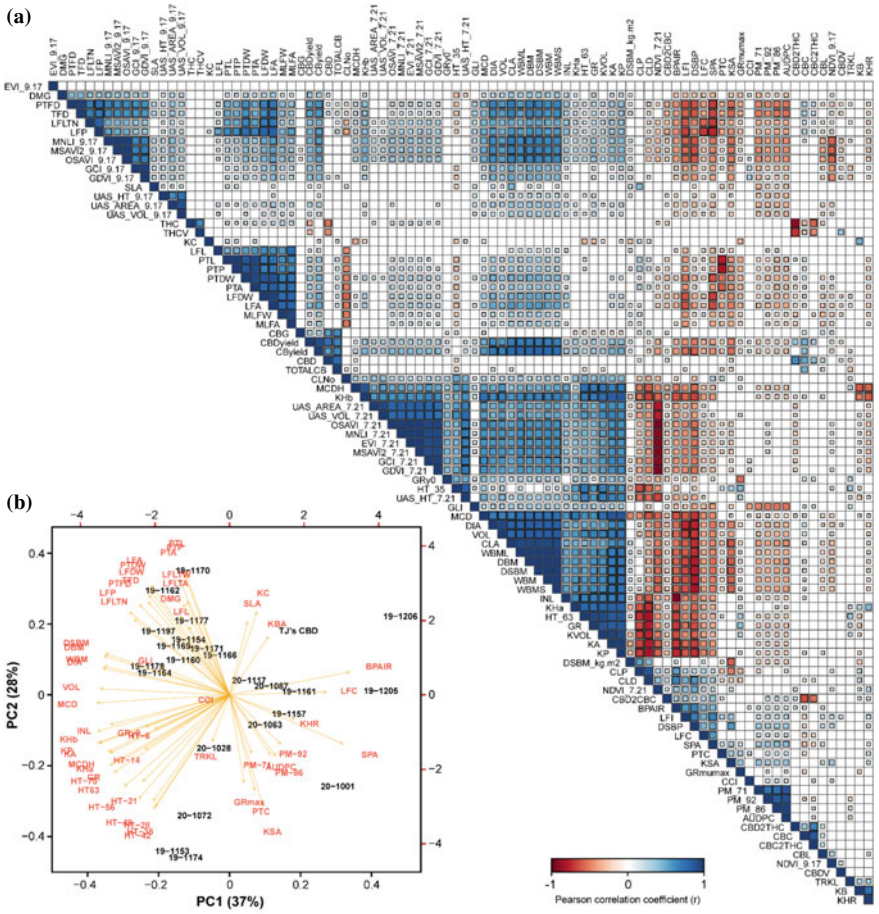

Fig. 2.9 Pairwise correlations of field collected traits. The color of each square in (**a**) represents a significant ($p < 0.01$) positive (blue) or inverse (red) correlation. The size of each square represents the strength of the correlation. Non-significant correlations ($p < 0.01$) were not drawn. Traits were ordered via hierarchical clustering (method = "complete"). PCA biplot (**b**) of the same traits (scaled) using family means

has been attempted with Fourier transform near-infrared spectroscopy (FT-NIR), but concerted segmentation of inflorescences would be required to develop an effective strategy to better estimate these profiles from aerial imaging. Further analyses of denser, direct-seeded plantings would both reduce incidence of lodging and offer better estimates compared with the larger plot spacing provided in this trial.

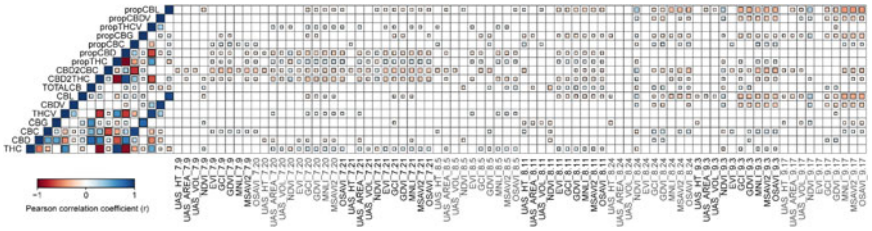

Fig. 2.10 Pairwise correlations of cannabinoid profiles and aerial indices over time. The color of each square in (A) represents a significant ($p < 0.01$) positive (blue) or inverse (red) correlation. The size of each square represents the strength of the correlation. Non-significant correlations ($p < 0.01$) were not drawn

2.4 Discussion

The developed ROS-based data acquisition system showed the capability to handle multiple sensors for collecting aerial images in the field. Sensors attached to the UAS platform were both with and without onboard data acquisition support, showing the ability of the proposed framework for designing new data acquisition systems for UAS platforms.

The case study demonstrated the use of this framework for only two sensors in one system and did not fully attempt all possible needs in the future. Based on a large body of literature in using ROS for UAS control, especially multi-agent UAS control [4, 28, 31], however, it is reasonable to envision the smooth integration of ROS-based data acquisition systems with multimodal sensing modules and/or UAS swarms for agricultural applications in the future. In particular, previous efforts on ROS-based UAS control and motion planning could be reused with minimal modifications for these newly integrated systems. Compared with off-the-shelf solutions and custom data acquisition systems previously developed, the framework in this chapter offers a new paradigm enabling rapid system development, deployment, and testing.

On the other hand, ROS has some major limitations such as no support of real time operations, which has led to the revolutionary development of ROS2. Although ROS2 uses many different design and implementation choices than ROS, it is fortunate that the ROS community provides several ways (e.g., ROS bridge package) to enable the communication between ROS and ROS2 to maximize the code reuse and performance stability. In particular, the use of ROS2 is highly recommended by the PX4 Autopilot community and would receive a strong community support for technical development and testing. In contrast, the DJI ecosystem has a slower pace in adopting newly developed ROS2 and/or other third-party libraries (e.g., MAVSDK) due likely to the compatibility and stability considerations. This may create additional burdens for researchers who may want to simultaneously take the advantages of ROS2 and commercial products with guaranteed performance and reliability.

2.5 Summary

This chapter provides a conceptual framework based on ROS to guide the design and development of data acquisition system for UAS in agricultural applications. By taking the advantage of ROS, the data acquisition system can have desired stability, customizability, modularity, and expandability without special considerations and efforts from developers. The conceptual framework provides implementation examples for sensors with/without onboard data acquisition support, which cover most possible use cases in practice. This will also be crucial for integrating multimodal sensing modules in a balanced data I/O to circumvent possible I/O issues in a central computer. The conceptual framework is expected to be used as a reference guideline for the development of multimodal and multi-agent UAS systems for digital agriculture in the future.

Acknowledgements The author would like to greatly thank Drs. Craig H Carlson and Lawrence B Smart to provide plant materials, experiment design, field management, and some results presented in this chapter.

References

1. Barbedo JGA (2019) A review on the use of unmanned aerial vehicles and imaging sensors for monitoring and assessing plant stresses. Drones 3(2)
2. Birner Regina, Daum Thomas, Pray Carl (2021) Who drives the digital revolution in agriculture? a review of supply-side trends, players and challenges. Appl Econ Perspect Policy 43(4):1260–1285
3. Bouabdallah S, Siegwart R (2007) Full control of a quadrotor. 2007 Ieee/Rsj International Conference on Intelligent Robots and Systems, Vols 1–9, pp 153–158
4. Cacace J, Finzi A, Lippiello V, Furci M, Mimmo N, Marconi L (2016) A control architecture for multiple drones operated via multimodal interaction in search & rescue mission. 2016 Ieee International Symposium on Safety, Security, and Rescue Robotics (Ssrr), pp 233–239
5. Carlson CH, Stack GM, Jiang Y, Taskiran B, Cala AR, Toth JA, Philippe G, Rose JKC, Smart CD, Smart LB (2021) Morphometric relationships and their contribution to biomass and cannabinoid yield in hybrids of hemp (cannabis sativa). J Experim Botany 72(22):7694–7709
6. Chang CY, Zhou RQ, Kira O, Marri S, Skovira J, Gu LH, Sun Y (2020) An unmanned aerial system (uas) for concurrent measurements of solar-induced chlorophyll fluorescence and hyperspectral reflectance toward improving crop monitoring. Agricultural and Forest Meteorology, 294
7. Or Dantsker D, Renato Mancuso, Michael S. Selig, Marco Caccamo. High-Frequency Sensor Data Acquisition System (SDAC) for Flight Control and Aerodynamic Data Collection
8. Henri Eisenbeiss (2004) A mini unmanned aerial vehicle (uav): system overview and image acquisition. Int Archives Photogr Remote Sens Spatial Inf Sci 36(5/W1):1–7
9. Feng L, Chen SS, Zhang C, Zhang YC, He Y (2021) A comprehensive review on recent applications of unmanned aerial vehicle remote sensing with various sensors for high-throughput plant phenotyping. Comput Elect Agric, 182
10. Francesconi S, Harfouche A, Maesano M, Balestra GM (2021) Uav-based thermal, rgb imaging and gene expression analysis allowed detection of fusarium head blight and gave new insights into the physiological responses to the disease in durum wheat. Front Plant Sci, 12

11. Gharib MR, Moavenian M (2016) Full dynamics and control of a quadrotor using quantitative feedback theory. Int J Numer Model Elect Netw Dev Fields 29(3):501–519
12. Godde CM, Mason-D'Croz D, Mayberry DE, Thornton PK, Herrero M (2021) Impacts of climate change on the livestock food supply chain; a review of the evidence. Glob Food Sec Agricult Policy Econ Environ, 28
13. Gomiero T, Paoletti MG, Pimentel D (2008) Energy and environmental issues in organic and conventional agriculture. Crit Rev Plant Sci 27(4):239–254
14. Guo W, Carroll ME, Singh A, Swetnam TL, Merchant N, Sarkar S, Singh AK, Ganapathysubramanian B (2021) Uas-based plant phenotyping for research and breeding applications. Plant Phen, 2021
15. Hassan MA, Yang MJ, Rasheed A, Yang GJ, Reynolds M, Xia XC, Xiao YG, He ZH (2019) A rapid monitoring of ndvi across the wheat growth cycle for grain yield prediction using a multi-spectral uav platform. Plant Sci 282:95–103
16. Hengy S, Laurenzis M, Schertzer S, Hommes A, Kloeppel F, Shoykhetbrod A, Geibig T, Johannes W, Rassy O, Christnacher F (2017) Multimodal uav detection: study of various intrusion scenarios. Electro-Opt Remote Sens Xi, 10434
17. Jimenez-Brenes FM, Lopez-Granados, de Castro AI, Torres-Sanchez J, Serrano N, Pena JM (2017) Quantifying pruning impacts on olive tree architecture and annual canopy growth by using uav-based 3d modelling. Plant Methods, 13
18. Kim J, Kim S, Ju C, Son HI (2019) Unmanned aerial vehicles in agriculture: a review of perspective of platform, control, and applications. IEEE Access 7:105100–105115
19. Klerkx L, Jakku E, Labarthe P (2019) A review of social science on digital agriculture, smart farming and agriculture 4.0: New contributions and a future research agenda. Njas-Wageningen J Life Sci, 90–91
20. Li C, Zhang Y, Li P (2017) Full control of a quadrotor using parameter-scheduled backstepping method: implementation and experimental tests. Nonlin Dyn 89(2):1259–1278
21. Li JT, Shi YY, Veeranampalayam-Sivakumar AN, Schachtman DP (2018) Elucidating sorghum biomass, nitrogen and chlorophyll contents with spectral and morphological traits derived from unmanned aircraft system. Front Plant Sci, 9
22. Lipovsky P, Szoke Z, Moucha V, Jurc R, Novotnak J (2019) Data acquisition system for uav autopilot and operator evaluation. 2019 Modern Safety Technologies in Transportation (Mosatt), pp 98–103
23. Madani T, Benallegue A (2006) Control of a quadrotor mini-helicopter via full state backstepiping technique. Proceedings of the 45th Ieee Conference on Decision and Control, Vols 1–14, pp 1515–1520
24. Molotoks A, Smith P, Dawson TP (2021) Impacts of land use, population, and climate change on global food security. Food Energy Sec 10(1)
25. Popescu D, Stoican F, Stamatescu G, Ichim L, Dragana C (2020) Advanced uav-wsn system for intelligent monitoring in precision agriculture. Sensors, 20(3)
26. Morgan Quigley, Josh Faust, Tully Foote, Jeremy Leibs. Ros: an open-source robot operating system. In International Conference on Robotics and Automation, vol 3
27. Rosas JTF, Pinto FDD, de Queiroz DM, Villar FMD, Valente DSM, Martins RN (2022) Coffee ripeness monitoring using a uav-mounted low-cost multispectral camera. Prec Agric 23(1):300–318
28. Shi P, Yan B (2021) A survey on intelligent control for multiagent systems. IEEE Trans Syst Man Cyber Syst 51(1):161–175
29. Shi YY, Thomasson JA, Murray SC, Pugh NA, Rooney WL, Shafian S, Rajan N, Rouze G, Morgan CLS, Neely HL, Rana A, Bagavathiannan MV, Henrickson J, Bowden E, Valasek J, Olsenholler J, Bishop MP, Sheridan R, Putman EB, Popescu S, Burks T, Cope D, Ibrahim A, McCutchen BF, Baltensperger DD, Avant RV, Vidrine M, Yang CH (2016) Unmanned aerial vehicles for high-throughput phenotyping and agronomic research. Plos One 11(7)
30. Tattaris M, Reynolds MP, Chapman SC (2016) A direct comparison of remote sensing approaches for high-throughput phenotyping in plant breeding. Front Plant Sci, 7

31. Thakoor O, Garg J, Nagi R (2020) Multiagent uav routing: a game theory analysis with tight price of anarchy bounds. IEEE Transac Autom Sci Eng 17(1):100–116
32. Tsouros DC, Bibi S, Sarigiannidis PG (2019) A review on uav-based applications for precision agriculture. Information 10(11)
33. Thomas Vatter, Adrian Gracia-Romero, Shawn Carlisle Kefauver, María Teresa Nieto-Taladriz, Nieves Aparicio, José Luis Araus (2021) Preharvest phenotypic prediction of grain quality and yield of durum wheat using multispectral imaging. The Plant J, n/a(n/a)
34. Wang Xu, Sun Hong, Long Yaowei, Zheng Lihua, Liu Haojie, Li Minzan (2018) Development of visualization system for agricultural uav crop growth information collection. IFAC-PapersOnLine 51(17):631–636
35. Xie CQ, Yang C (2020) A review on plant high-throughput phenotyping traits using uav-based sensors. Comput Elect Agricul, 178
36. Xu R, Li CY, Bernardes S (2021) Development and testing of a uav-based multi-sensor system for plant phenotyping and precision agriculture. Remote Sens 13(17)
37. Yang GJ, Liu JG, Zhao CJ, Li ZH, Huang YB, Yu HY, Xu B, Yang XD, Zhu DM, Zhang XY, Zhang RY, Feng HK, Zhao XQ, Li ZH, Li HL, Yang H (2017) Unmanned aerial vehicle remote sensing for field-based crop phenotyping: current status and perspectives. Front Plant Sci 8
38. Yu N, Li LJ, Schmitz N, Tiaz LF, Greenberg JA, Diers BW (2016) Development of methods to improve soybean yield estimation and predict plant maturity with an unmanned aerial vehicle based platform. Remote Sens Environ 187:91–101
39. Steven Zahniser, Edward Taylor J, Thomas Hertz, Diane Charlton (2018) Farm labor markets in the united states and mexico pose challenges for u.s. agriculture. Report, USDA Economic Research Service

Chapter 3
Unmanned Aerial Vehicle (UAV) Applications in Cotton Production

Aijing Feng, Chin Nee Vong, and Jianfeng Zhou

Abstract Cotton (*Gossypium hirsutum L.*) is an important cash crop and primary materials for clothing, fine paper, animal feed, and oil industries. Cotton production is affected by a combination effect of crop varieties, environment, and management. Precision agriculture technology has shown great potential to improve cotton production with sufficient high-resolution spatiotemporal data of soil, environment, and cotton development from seedling to harvest. The advances in unmanned aerial vehicles (UAVs), computer vision, and remote and proximal sensing technologies make it possible to scan large-scale field efficiently and quantify crop development. The big data analytics enabled by artificial intelligence (AI) have significantly increased the capacity in processing and analyzing complex data to quantify the interactions of environment and management on crop growth and yield. This chapter aims to summarize UAV applications in cotton production, focusing on field scouting and decision making, such as stand count, growth monitoring, and yield prediction, under different soil, weather conditions, and irrigation management. Meanwhile, the potentials and challenges of using UAV technologies in cotton production are also discussed.

Keywords UAV imaging · Remote sensing · Field management · Crop emergence · Growth monitoring · Yield prediction

3.1 Introduction

3.1.1 Precision Agriculture Technology in Agricultural Production

Cotton (*Gossypium hirsutum L.*) is an important cash crop that provides approximately 35% of the total fibers for textile industry, including clothing and fine paper

A. Feng · C. N. Vong · J. Zhou (✉)
Division of Plant Science and Technology, University of Missouri, Columbia, MO 65211, USA
e-mail: zhoujianf@missouri.edu

A. Feng
Bond Life Science Center, University of Missouri, Columbia, MO 65211, USA

Z. Zhang et al. (eds.), *Unmanned Aerial Systems in Precision Agriculture*,
Smart Agriculture 2, https://doi.org/10.1007/978-981-19-2027-1_3

[1, 2]. Cotton seeds are also critical sources for feed and oil industries because of their rich oil (18 - 24%) and protein (20–40%) [1, 2]. Cotton plays an important role in human daily life and livestock industry, and is grown in 17 states and as a major crop in 14 states of the United States of America [3]. There is a great need to increase cotton production due to the increasing global population of more than nine billion in 2050. However, there are adverse conditions for improving agricultural production, such as decreasing arable land due to urbanization, declining soil quality (e.g., soil erosion, salinization, and nutrient reduction) due to long-term cultivation, and insufficient freshwater for crop irrigation [4]. It is time to improve cotton production using emerging technologies to reduce the inputs of natural resources and impacts on environments.

Cotton production is determined by the combined effects of genotype, environment, and management (G × E × M) [5]. To understand the G × E × M interaction, acquiring high-resolution data of crop, water, and other environments is needed using emerging remote and proximal sensing technologies. Studies have shown that timely crop monitoring and accurate yield estimation are important in making optimal decisions for field management, increasing cotton production, and reducing the negative impacts on environments. For example, the information of cotton plants and the environment obtained from different growing stages can be used to quantify the environmental impacts and nutrient deficiencies [6] on cotton development and yield. Precision agriculture (PA) technology has been used as a promising field management strategy to improve crop production and management efficiency based on site-specific information. The key factors for the success of PA include fast and accurate data acquisition of crops, soil, and environments in a large field. It also needs timely data processing and analysis pipelines to translate sensor data to executive data for field management decisions [7–9].

Sensor systems are the key components for the implementation of PA for agricultural production. Various sensors have been used to quantify crop development and environmental variations [10, 11], which provide necessary information to develop decision-making tools for field management. Some examples include in-field weather stations that continuously record environmental conditions, e.g., air temperature, humidity, solar radiation, and precipitation. Proximal sensors (e.g., soil apparent electrical conductivity (EC_a) sensor and soil moisture sensor) are used to estimate soil texture, organic matter content [12], and soil moisture content at different depths. Infrared thermometers (IRTs) are used to measure crop canopy temperature to determine cotton water stress and schedule irrigation [13]. In addition, remote sensing systems based on satellite, airplane, unmanned aerial vehicles (UAVs), and ground vehicles are equipped with different sensors (e.g., optical sensors) for crop monitoring. The above site-specific information has been used to improve the efficiency of field management and crop production.

3.1.2 UAV-Based Remote Sensing (RS) for Crop Monitoring

Unmanned aerial vehicle (UAV)-based RS is currently widely used for crop monitoring due to the advantages of flexibility in sensor selection and data collection time when compared to satellite-based and ground-based sensing platforms. The UAV-based RS systems are usually equipped with multiple cameras and a global navigation satellite system (GNSS) to collect georeferenced imagery data of crops and soil in a high-throughput manner [14]. These systems are widely used to scout crops and collect site-specific information to make accurate decisions of crop management [15, 16]. Typical cameras used in UAV-based RS systems include visible red–green–blue (RGB) cameras, multispectral cameras, hyperspectral cameras, and infrared (IR) thermal cameras [14, 17]. Imagery data are processed using advanced machine learning (ML) to quantify crop characteristics in architecture, physiology, and chemical compositions [18], which are associated with plant health conditions and responses to the variation of environment and management.

The visible RGB cameras are the most ready-to-use sensors that are less expensive and in higher resolution comparing to multispectral and thermal cameras. The RGB cameras consist of three optical sensors with spectral bands of red (typical 550–650 nm), green (typical 470–600 nm), and blue (typical 420–530 nm) to produce digital images [19]. They have been used to acquire color information of different plant organs (e.g., leaf, stem, flower, and cotton boll) that can be used to characterize plants, quantify their health conditions and responses to biotic and abiotic stresses. The RGB images are also used to build point cloud data of plants to extract three-dimensional (3D) information, such as plant height and 3D architecture. As shown in Table 3.1, RGB images are used to calculate different image features that are used to quantify cotton development and yield. For example, plant height (PH), canopy cover (CC), greenness described as a^* and triangular greenness index (TGI) are used for the assessment of cotton stand count [14, 20]. Moreover, the cotton fiber index (CFI) derived from RGB images has been used as a useful index for cotton yield estimation [14, 21].

Despite the advantages of using RGB cameras, they are still limited by only being able to acquire information of plants in the spectral range of 400 to 700 nm wavelength. Research has found that some spectral bands in near-infrared range (800–2,500 nm) are more sensitive to the variations of plants due to biotic and abiotic stresses. Multispectral and hyperspectral cameras have been used in many studies to acquire high spatial resolution spectral information from the plants. Multispectral cameras usually consist of optical sensors with less than ten independent spectral bands, and hyperspectral cameras consist of up to 300 spectral bands. The image features extracted from these spectral cameras include spectral information of each band and their combination, which have shown great potential to quantify plant heath conditions and estimate yield. Some examples (as summarized in Table 3.1) show that different vegetation indices (VIs) based on the combination of multiple spectral bands are able to monitor plant health status and estimate cotton yield [14, 33, 40].

Table 3.1 Useful image features for cotton monitoring with UAV-based RS systems

Image type	Image features	Equations	Related traits	References
RGB	Seedling size	Total pixel number of a plant	Seedling stand count	[17, 22]
	Canopy cover *(CC)*	$CC = \frac{number\ of\ pixels\ of\ crop\ in\ a\ ROI}{overall\ number\ of\ pixels\ in\ the\ ROI}$	Yield, biomass, crop density	[23–26]
	Plant height	The difference in elevation between crop canopy and soil surface	Yield	[27–29]
	Cotton fiber index (*CFI*)	$CFI = \frac{number\ of\ pixels\ for\ fibre\ in\ a\ ROI}{overall\ number\ of\ pixels\ in\ the\ ROI}$	Yield	[14, 21]
	a^*	a^* channel in the CIE-LAB color space; a* represents the green–red color components	Yield, water content, nitrogen, chlorophyll content	[10, 30–32]
	Triangular greenness index (*TGI*)	TGI = -0.5 × ((*R*-*G*) × 0.19-(*R*-*B*) × 0.12), where R, G and B are pixel values in three channels	Yield, water content, nitrogen, chlorophyll content	[10, 30–32]
MS/ HS	*NDVI*	$NDVI = \frac{NIR-R}{NIR+R}$ where *NIR* and *R* are pixel values in the near-infrared and red channels, respectively	Yield, chlorophyll content, biomass	[23, 33–35]
	GNDVI	$GNDVI = \frac{NIR-G}{NIR+G}$ where *G* are pixel values in the green channel	Yield, chlorophyll content, biomass	[23, 34]
	NDRE	$NDRE = \frac{NIR-RE}{NIR+RE}$ where *RE* are pixel values in the red edge channel	Crop senescence, maturity	[36, 37]
Thermal	Crop water stress index *(CWSI)*	$CWSI = \frac{T_c-T_w}{T_b-T_w}$ where T_c is the crop canopy temperature, T_b is the temperature of the black poster board, and T_w is the temperature of the white poster board	Yield, water stress	[38, 39]

[$] ROI: region of interest; RGB: red–green–blue; MS: multispectral; HS: hyperspectral; NDVI: normalized difference vegetation index; GNDVI: green-based normalized difference vegetation index; and NDRE: normalized difference red edge index

In addition, thermal cameras have been used to quantify the energy of infrared (IR) radiation of an object with a temperature above absolute zero (-273 °C). Infrared thermal cameras capture the long-wave IR radiation (7.5–14 μm) emitted from crops and convert such radiation to electrical signals [41]. Plant temperature measurement has been primarily used to study plant water relations (e.g., stomatal conductance) since a major determinant of leaf temperature is the rate of evaporation or transpiration from the leaf [41]. Canopy temperature is highly correlated with canopy water stress and is used to capture plant responses to biotic and abiotic stresses [38]. Canopy temperature and the calculated crop water stress index (CWSI, Table 3.1) are found to be related to leaf water content [42–44] and show great potential for yield prediction [14].

3.1.3 UAV Imagery Data Processing Pipeline

Generally, the UAV imagery data collected are in the format of interval snapshots (still images) or videos. A large number of images may be collected for a large field. Figure 3.1 illustrates one of the typical data processing pipelines for UAV images, including image pre-processing, image processing, and analysis. The pre-processing steps consist of generating geo-referenced orthomosaic images and digital surface models (DSMs) [16] from the collected hundreds and thousands of sequential images

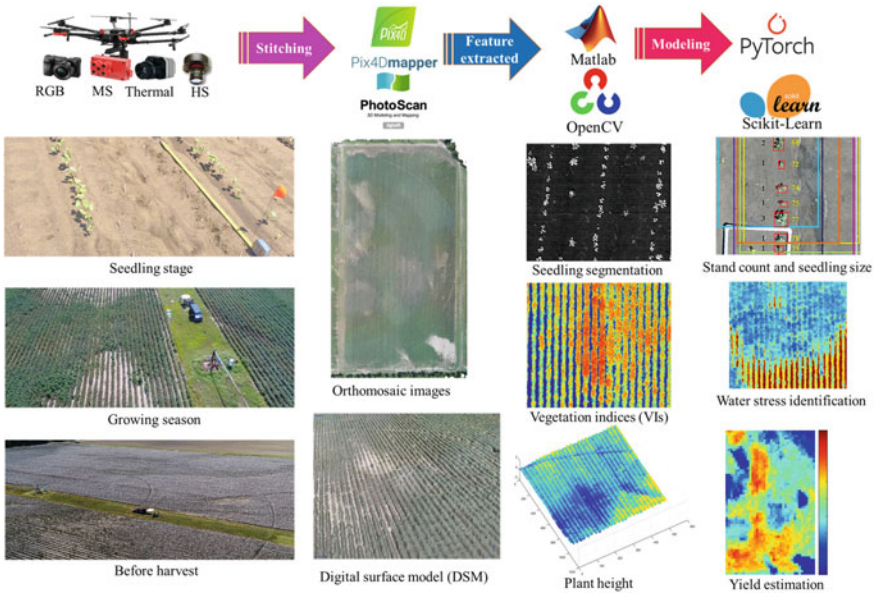

Fig. 3.1 General steps for UAV imagery data collection, processing, and analysis

or videos. The processes are usually conducted using customized or commercial UAV image stitching software such as Agisoft PhotoScan (Agisoft LLC, St. Petersburg, Russia) and Pix4D (Pix4D S.A., Prilly, Switzerland). Geo-referenced orthomosaic images and DSMs are further processed using advanced image processing techniques to remove background, segment plants, and extract image features. The image processing can be performed using commercial or open-source software such as Matlab (The MathWorks, Inc., Natick, MA, USA) and OpenCV (https://opencv.org/). The final step, image analysis, uses advanced ML models to translate the original images or extracted image features to useful information that is important for crop management. Some example applications include seedling assessment and stand count, water stress identification, and yield estimation. Some widely used commercial and open-source software for this step include Matlab, RStudio (RStudio, Boston, MA, USA) and PyTorch (https://pytorch.org/).

3.2 UAV Systems in Cotton Production

3.2.1 Field Management for Cotton Production

Cotton production includes several key growth stages, as shown in Fig. 3.2, including seed emergence, seedling, squaring, blooming (flowering), open boll, and harvest, that need different management strategies. The life span of cotton is about 150 – 180 days in the United States [3]. Germination and emergence usually take 5–15 days depending on the weather condition, soil temperature and moisture [45–47]. Some of

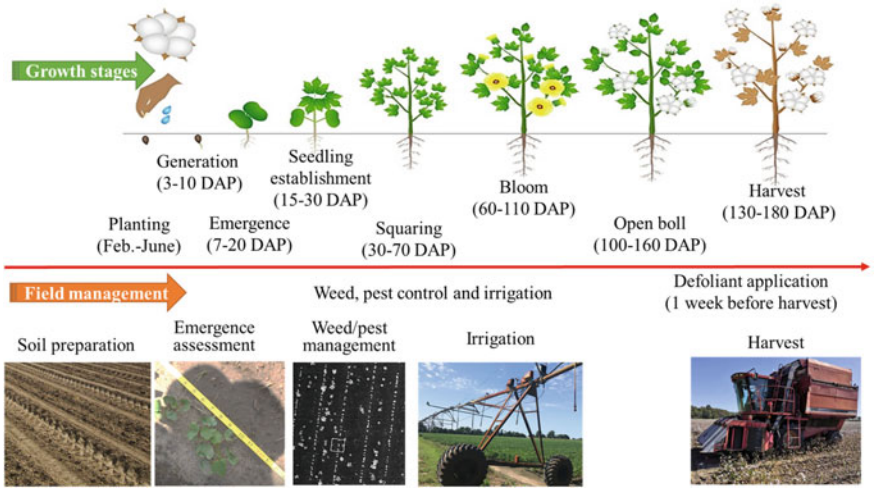

Fig. 3.2 Cotton development and related field managements. DAP: days after planting

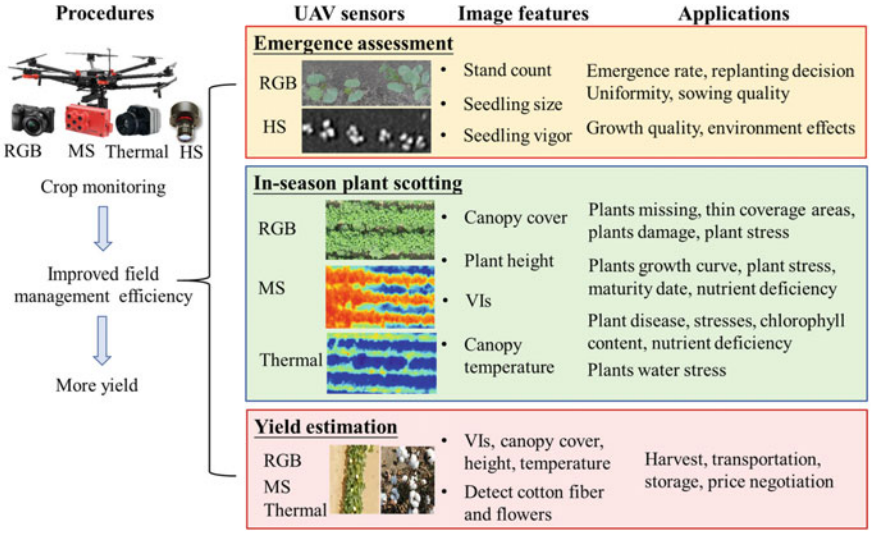

Fig. 3.3 UAV systems for cotton monitoring from emergence, development to harvest. RGB: red–green–blue; MS: multispectral; HS: hyperspectral; VIs: vegetation indices

the major factors that influence cotton growth and yield include planting rate, planting depth, row spacing, and seed placement [48–50]. Early stage field management in crop emergence and seedling establishment includes emergence and stand count assessment [50, 51] and weed control [3]. Pests, such as spider mites, aphids, whitefly and lygus bugs, are the primary targets to be managed at the stage after the first square [50, 52]. In addition, irrigation management is also an important practice in cotton production during square to bloom growth stages to improve yield [3, 13, 53–55]. Lastly, harvesting at the right time can potentially reduce crop yield loss.

Based on the general field management for cotton production mentioned perviously, the following sections will discuss the applications of UAV-based RS systems in making decisions on these field management. The sections are arranged based on different growth stages: (1) cotton emergence evaluations, (2) full-season cotton growth and health monitoring, and (3) yield estimation. The contents consist of the progress and advances of UAV applications in cotton production and the potentials and challenges of adopting UAVs in large-scale cotton production. Figure 3.3 summarizes the general approaches (sensors and image features used) and associated applications of using UAV-based RS systems in cotton production.

3.2.2 Cotton Emergence Assessment

Crop emergence is an important agronomic factor for field management in early stages. Cotton emergence is usually assessed based on plant population, stand count,

uniformity, seedling size, and etc. [50, 51]. Accurate and timely assessment of cotton stand count and seedling size helps farmers to make important management decisions, such as replanting, to reduce the yield loss due to missing plants [52]. Meanwhile, accurate cotton emergence information can be used to quantify the impact of soil and environments on crop emergence [56, 57], which may help farmers make optimal decisions on seed placement and planting. Conventionally, cotton emergence is assessed through visual observation (manual counts) in a small number of sampling sites [58], which is time-consuming, labor-intensive, and not suited to cover a large production field. Hence, UAV-based imaging technology has been used to assess some cotton emergence parameters such as stand count, canopy size, seedling number, and uniformity based on plant spacing as indicated in Table 3.2.

The primary challenge of assessing the cotton emergence using UAV imaging systems is the small seedling size at the early stage. For instance, their diameters were 2.4 and 3.5 cm on 11 and 17 DAP, respectively [61]. Hence, sufficient image resolution or GSD is needed and high-resolution RGB cameras have been widely used compared to other cameras (Table 3.1). With a low flight height of 10 to 20 m, images taken from the RGB cameras can achieve a better GSD ranging from 0.25 to 0.9 cm pixel^{-1}. However, using RGB cameras give another challenge on image segmentation to remove the background and detect the small seedlings. The large portion of soil background in the images caused the color distortion of seedlings due to the strong reflectance of soil [62] and the color contrast between crops and soil was weak [17]. Previous research indicated that RGB images were potentially affected by sunlight conditions and suggested that using multispectral images with near-infrared (NIR) spectral bands could be more efficient for crop seedling segmentation

Table 3.2 Studies related to cotton emergence assessment (stand count, canopy size, and seedling number) using UAV imagery

Emergence parameter	Sensor	DAP (days)	Flight Height (m)	GSD (cm pixel^{-1})	Performance (Accuracy)	References
Stand count/plant density	RGB	6–11	15–20	0.6–0. 9	88.6%	[59]
		16	10	0.3	$R^2 = 0.95$	[22]
		10–20	10	0.25	$R^2 =$ 0.82–0.97	[60]
		11–17	20	0.3	$R^2 =$ 0.48–0.98	[61]
	Hyperspectral	15	50	0.8	$R^2 = 0.61$	[17]
Canopy size	RGB	16	10	0.3	$R^2 = 0.95$	[22]
Seedling number	Hyperspectral	15	50	0.8	84.1%	[17]
Uniformity: plant spacing	Hyperspectral	15	50	0.8	$R^2 =$ 0.91–1.00	[17]

Abbreviations DAP = days after planting; GSD = ground sample distance; R^2 = coefficient of determination

[63]. For example, Feng et al. [22] assessed cotton emergence using a UAV-based hyperspectral imager for quantifying cotton plant density and uniformity. However, the accuracy for plant density could only achieve 0.61, which was lower than that of the studies using RGB cameras. The advantage of using hyperspectral imagers is the higher spectral resolution, which can be useful for other stress studies during the growing season, but they are limited by their higher cost and a large amount of data with proper data processing and analysis needed [64] as compared to simple RGB cameras.

Deep learning (DL) models are widely used to directly locate and detect each cotton seedlings [60, 61] and extract information such as average stand count and canopy size [22] from the UAV images. The DL models used included Resnet18, YOLOv3, MobileNet, and CenterNet and achieved the highest R^2 of 0.98 [22, 60, 61]. One example of the DL model used by Feng, Zhou, et al. [14] is illustrated in Fig. 3.4, where the DL model was able to extract "hidden" information (a subtle difference) using multiple convolution and pooling layers to distinguish seedlings and background information.

The commonly used image processing pipeline (Fig. 3.1) requires stitching collected images using commercial software. The image stitching process may take a long time when thousands of images are collected from high-resolution cameras and at low flight height in field-scale studies. This issue may restrict their usage for PA applications to conduct timely management practices at the right time with accurate data. To improve the efficiency, Feng, Zhou [22] proposed a novel pipeline, as illustrated in Fig. 3.5, to process and analyze each UAV image directly to avoid image stitching procedure. The pipeline can process one image (20 M pixels) in about 2 s to extract the information of emergence, which provides an alternative method to assess cotton emergence in near real-time. It is possible to implement the image processing pipeline to an edge computing system that is integrated with a UAV system for real-time and on-site data processing and decision making. To conclude,

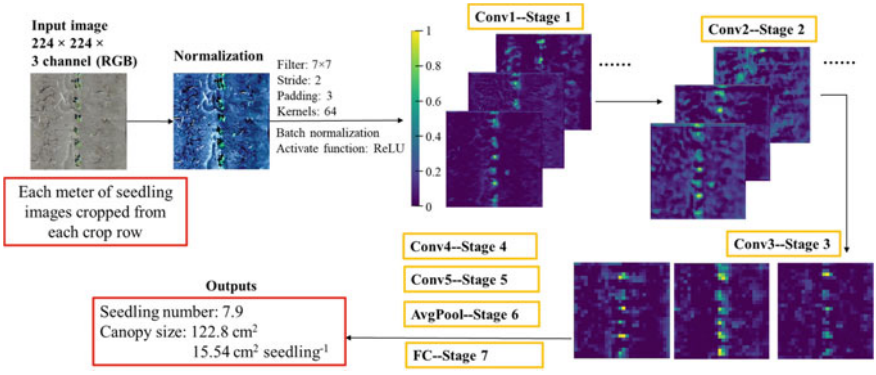

Fig. 3.4 The *Resnet18* deep learning model used for cotton stand count and seedling canopy size estimation in the study of [22]

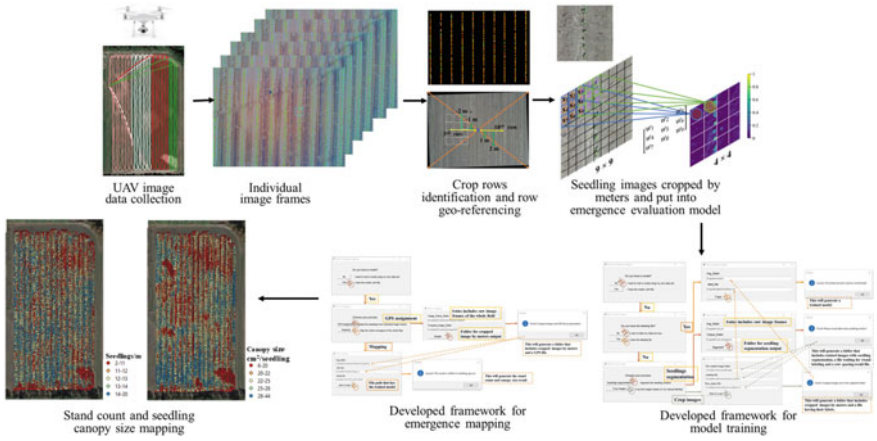

Fig. 3.5 A framework (pipeline) for processing single frame of UAV images in a near real-time manner. The pipeline was validated in the study of cotton emergence evaluation [22]

DL and real-time image processing will enhance the UAV-based imaging systems in the cotton emergence assessment in commercial farms in the future.

3.2.3 Cotton Growth Monitoring Using UAV-Based RS

Crop growth and production are complex and determined by many factors, including crop genotypes (varieties), environments (e.g., weather, soil, microclimate, and location), and agronomic management strategies [65]. During the cotton growing season, several field management practices, including irrigation and chemicals (fertilization, pesticides, and herbicides) applications, need to be optimized to achieve optimal production. High-resolution site-specific crop information is needed to determine crop stresses for variable rate applications.

Irrigation is one of the most important management practices in cotton production since cotton's growth and yield are sensitive to water deficit [66, 67]. The optimal irrigation schedule can be made according to the cotton water demand to replace the water loss due to evapotranspiration (ET), determined by cotton varieties, weather conditions, soil texture, and irrigation treatment [68, 69]. Infrared thermal cameras mounted on UAV had been widely used to detect cotton water stress by first estimating the canopy temperature and computing stress indices such as CWSI in Table 3.1 [44, 70–72]. Stomatal conductance has been used as one of the ground truth data to describe crop water stress response. Studies have shown a moderate to high correlation between stomatal conductance and CWSI computed using canopy temperature from UAV-based thermal cameras with r = -0.48 [71] and R^2 = 0.66 to 0.91 [44, 70]. One of the challenges in using thermal imagery from thermal cameras is the background (i.e., soil and residue) removal since the pixel numbers from the thermal

images are based on temperature values and not color information. Hence, some other image segmentation methods have been used, such as edge detection algorithms (Canny, Prewitt, and Roberts methods) [44]. Some thermal cameras have visible cameras attached, which could be used for the image segmentation based on visible images and creating a mask and co-registered with the thermal images to remove background [73]. These procedures are required to ensure that only crop canopy temperature is used in the crop water stress indices to improve the estimation accuracy.

Besides thermal cameras, some studies also demonstrated the usage of VIs computed from RGB and multispectral images in determining the cotton water stress and plant water content [44, 70, 74]. For instance, moderate to high correlations (significant $r = 0.3$ to 0.9 regardless of negative or positive correlation; $R^2 = 0.6$ to 0.9) were found between different VIs from multispectral cameras with plant water contents at different parts (leaves, petioles, buds and bolls, stalks) [74]. When relating the different VIs to stomatal conductance, mixed results were found with low to high R^2 (for example, NDVI ranged from 0.01 to 0.89) and their R^2s were mostly lower as compared to thermal images [44, 70]. However, RGB and multispectral cameras are frequently used for other purposes such as weed and pest detection and mapping for UAV-based variable-rate spraying during the growing seasons as delineated in the following.

Using UAV-based RS systems is a promising way for weed, pest, nutrient and disease control in commercial cotton fields [3, 50, 52, 75, 76] and harvest aids [77, 78]. The key to efficient UAV-based variable-rate spraying is to identify the right regions of the cotton field and the right volume and time of spraying [78–81]. Optimal crop managment decisions are usually made according to cotton plant growth status that can be quantified by VIs [82, 83], canopy coverage [80], boll opening rate [77–79, 84], and pressure of weed [17, 85, 86], disease [87–91] and pest [81] of cotton fields. Advanced image processing methods and ML models (such as support vector machine, *k*-means classification, maximum likelihood, and random forest) are still the key for weed and disease identification and management decision making [81, 85, 87, 88]. Considering the complexity in field background of the images, DL methods are also promising image processing tools for cotton leaves disease and stress identification [91, 92].

Overall, UAV-based imagery from RGB, multispectral, and thermal cameras has demonstrated their great potential for in-season cotton field management. Some applicaitons include irrigation scheduling through plant water content and stress detection, variable rate chemical applications through mapping weeds and pests, and UAV variable-rate spraying. Most of these studies only used a single factor when developing the estimation models, such as crop response to irrigation [93, 94] or fertilizer [95, 96]. Few studies have integrated the interaction effects of environment and management due to the lack of long-term data and efficient tools for developing reliable models [97]. With the advance in the UAV-based RS, high-resolution imagery data can quickly quantify characteristics of crops and soil, which brings challenges in efficiently processing and analyzing the big data of different variety,

resolution, and data structures. Hence, future studies will be focused on more integration of different UAV-based cameras with more advanced ML and DL modellings to explore the relationships between soil properties, weather conditions, and cotton growth variation [98].

3.2.4 Cotton Yield Estimation

Accurate cotton yield estimation could help farmers make better decisions on management, such as harvest, transportation, and storage [99]. Cotton yield estimation can also provide needed information to understand the interaction effect of environment and management on crop development and yield, which is important in developing precision management strategies for cotton production [14]. The UAV-based imagery has been used to predict cotton yield using different image features, including plant height, canopy cover, canopy temperature, VIs (NDVI and GNDVI), and open cotton bolls (Table 3.1) [14, 21, 100–103]. The UAV imagery data are typically collected on the critical stages, such as flowering and/or boll opening [14]. Research showed that the combination of the image features could estimate yield with $R^2 > 0.80$ [14].

Several studies used high-resolution RGB images to detect and count open cotton bolls [101, 102]. Yeom et al. (2018) used image processing techniques (e.g. Otsu automatic thresholding) to extract the cotton bolls from the UAV images collected in the boll opening stage, achieving an accuracy of R^2 close to 0.6. Xu et al. (2020) used two fully convolutional DL networks to extract the cotton bolls, obtaining a better accuracy of $R^2 = 0.8$.

Current studies in yield estimation based on UAV imagery usually used data within a single year, i.e., using data from the same year for both model training and validation [104–107]. Future studies should focus on developing models for predicting crop yield of the coming years using historical data, which may have higher values for farmers to make proper decisions in advance to maximize their profit. In recent years, ML and DL techniques have been used to predict crop yield of future years using historical data of environment, management, and crop production [108–111]. Integration of the soil, weather, and crop data with different spatial and temporal resolutions utilizing advanced data analytic methods has the potential to improve the performance in quantifying field-scale crop growth and yield in a future year. One such example is a study conducted by Feng et al. (2021) that used an improved recurrent neural network (RNN) [112] model known as Gated Recurrent Units (GRU) [113] to analyze sets of sequential data, including soil, weather, and time-series imagery, for predicting cotton yield. As shown in Fig. 3.6, the architecture of the GRU comprises a reset gate and an update gate to control how much information is needed to be forgotten and memorized through the sequence.

The architecture of the yield prediction model based on the GRU is shown in Fig. 3.7, which included four layers, *i.e.*, soil features (S_CNN) and weather features (W_CNN) pre-processed using CNN filters, GRU layers for NDVI prediction ('GRU'

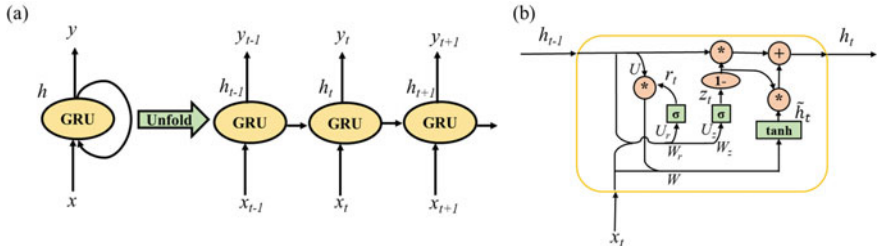

Fig. 3.6 Illustration of the Gated Recurrent Unit (GRU). **a** GRU continuously accepts inputs from a sequence. To easily understand the loop operation in the GRU, the GRU was drawn with the unfolded way. The '*t*' represented each time step. **b** The architecture of the GRU

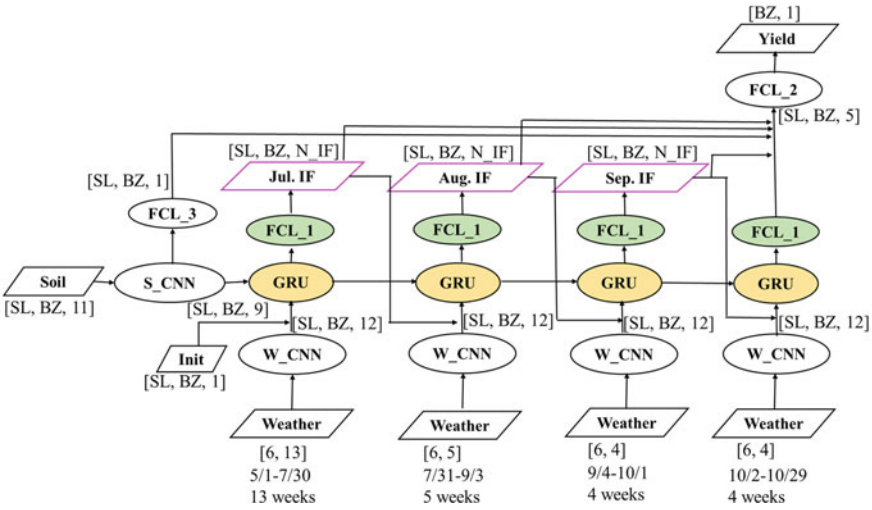

Fig. 3.7 The architecture of the GRU network. SL is sequence length, which was set to 1 in this study. BZ is the batch size for the training procedure. FCL means fully connected layer. IF is image feature (i.e., NDVI). All the GRUs highlighted with yellow color were the same loop processing unit in the network and had the same parameters. All FCL_1 units highlighted with green color were using the same parameters

in Fig. 3.7), and the fully connected layers for yield prediction ('FCL_2' in Fig. 3.7). The input parameters of the GRU network included eleven soil features processed by the S_CNN and weather data from May 1 to October 29, 2019, processed by the W_CNN. The initial hidden-input vector ('Init' in Fig. 3.7) of the GRU was set as zeros and the corresponding output was assumed to be the NDVI in July (the GRU output of its first loop). The hidden outputs of the July GRU were passed to the next loop of the GRU unit (i.e., the GRU in August). The processed weather data from July 31 to September 3 were also passed to the August GRU, which had an output assumed to be the NDVI in August. The NDVI in July was used to replace the 'Init'

to input to the August GRU. Similar procedures then defined the GRU processing units for September NDVI and for yield. The GRU unit was a three-month loop processing unit that each loop received the weather data from current month and the NDVI images from the previous month. The GRU was used to predict the NDVI spatial distribution of the current month based on the weather of the current month and the NDVI of the previous month.

The study indicates that the yield prediction model based on DL is able to integrate data of soil, weather, imagery, and yield that have different resolutions and data structures. The yield prediction model shows an improved performance compared to the models without the full integration of related environmental factors, which could explain 68–84% of yield measured with the yield monitor (ground truth data), with the prediction errors of MAE = 247 kg ha^{-1} (8.9%) - 345 kg ha^{-1} (12.3%) at different years. In summary, the study indicates the potential of predicting the cotton yield of a future year based on soil texture, weather conditions, and UAV imagery. Future research could investigate more leading methods in integrating multiple source data of multiple years to estimate field-scale yield in the following years.

3.3 Summary

This chapter introduced the UAV applications in cotton production, from stand count, growth monitoring to yield prediction. UAV-based RS systems, equipped with RGB, multispectral, hyperspectral and thermal cameras, provide a low-cost and efficient tool for monitoring cotton growth at different stages. The collected information will then be used to improve crop management, such as seedling replanting, weed and disease control, and irrigation. Future research would focus on integrating multiple source data (i.e., environmental, ground, and UAV data) to develop near real-time tools using advanced ML and DL modellings for more effective and accurate cotton emergence, growth, and yield estimation for commercial applications.

References

1. Johnson RM et al (2002) Variability in cotton fiber yield, fiber quality, and soil properties in a southeastern coastal plain. Agron J 94(6):1305–1316
2. Zhang J et al (2014) Genetics, breeding, and marker-assisted selection for Verticillium wilt resistance in cotton. Crop Sci 54(4):1289–1303
3. National Cotton Council of America (2021) Cotton: from field to fabric. [cited 2021 06/27]. https://www.cotton.org/pubs/cottoncounts/fieldtofabric/upload/Cotton-From-Field-to-Fabric-129k-PDF.pdf
4. Pennock D, McKenzie N, Montanarella L (2015) Status of the world's soil resources. Technical Summary FAO, Rome, Italy
5. Hatfield JL, Walthall CL (2015) Meeting global food needs: realizing the potential via genetics× environment× management interactions. Agron J 107(4):1215–1226

6. Holman FH et al (2016) High throughput field phenotyping of wheat plant height and growth rate in field plot trials using UAV based remote sensing. Remote Sens 8(12):1031
7. Zhang C, Kovacs JM (2012) The application of small unmanned aerial systems for precision agriculture: a review. Precision Agric 13(6):693–712
8. Lindblom J et al (2017) Promoting sustainable intensification in precision agriculture: review of decision support systems development and strategies. Precision Agric 18(3):309–331
9. Maes WH, Steppe K (2019) Perspectives for remote sensing with unmanned aerial vehicles in precision agriculture. Trends Plant Sci 24(2):152–164
10. Hunt ER et al (2013) A visible band index for remote sensing leaf chlorophyll content at the canopy scale. Int J Appl Earth Obs Geoinf 21:103–112
11. Bendig J et al (2015) Combining UAV-based plant height from crop surface models, visible, and near infrared vegetation indices for biomass monitoring in barley. Int J Appl Earth Obs Geoinf 39:79–87
12. Sudduth KA et al (2003) Comparison of electromagnetic induction and direct sensing of soil electrical conductivity. Agron J 95(3):472–482
13. Vories E et al (2020) Comparison of precision and conventional irrigation management of cotton and impact of soil texture. Prec Agricul, 1–18
14. Feng A et al (2020) Yield estimation in cotton using UAV-based multi-sensor imagery. Biosys Eng 193:101–114
15. Turner D et al (2014) Spatial co-registration of ultra-high resolution visible, multispectral and thermal images acquired with a micro-UAV over Antarctic moss beds. Remote Sens 6(5):4003–4024
16. Yang G et al (2017) Unmanned aerial vehicle remote sensing for field-based crop phenotyping: current status and perspectives. Front Plant Sci 8:1111
17. Feng A et al (2020) Evaluation of cotton emergence using UAV-based narrow-band spectral imagery with customized image alignment and stitching algorithms. Remote Sens 12(11):1764
18. Xie C, Yang C (2020) A review on plant high-throughput phenotyping traits using UAV-based sensors. Comput Elect Agricult 178:105731
19. Kolláth Z et al (2020) Introducing the dark sky unit for multi-spectral measurement of the night sky quality with commercial digital cameras. J Quant Spect Rad Transfer, 253
20. Chen Y, Mei X, Liu J (2015) Cotton growth monitoring and yield estimation based on assimilation of remote sensing data and crop growth model. In Geoinformatics, 2015 23rd International Conference on. IEEE. pp 1–4
21. Huang Y et al (2016) Cotton yield estimation using very high-resolution digital images acquired with a low-cost small unmanned aerial vehicle. Trans ASABE 59(6):1563–1574
22. Feng A et al (2020) Evaluation of cotton emergence using UAV-based imagery and deep learning. Comput Elect Agricul 177:105711
23. Hunt ER et al (2011) NIR-green-blue high-resolution digital images for assessment of winter cover crop biomass. GIScience & Remote Sens 48(1):86–98
24. Liu S et al (2017) A method to estimate plant density and plant spacing heterogeneity: application to wheat crops. Plant Methods 13(1):38
25. Steduto P et al (2012) Crop yield response to water, vol 1028. FAO Rome
26. Walton JT, Nowak DJ, Greenfield EJ (2008) Assessing urban forest canopy cover using airborne or satellite imagery. Arboricul Urban Forestry 38(6):334–340
27. Chang A et al (2017) Crop height monitoring with digital imagery from unmanned aerial system (UAS). Comput Electron Agric 141:232–237
28. Malambo L et al (2018) Multitemporal field-based plant height estimation using 3D point clouds generated from small unmanned aerial systems high-resolution imagery. Int J Appl Earth Obs Geoinf 64:31–42
29. Sharma K, Singhal A (2016) New algorithm for flower yield estimation and yield comparison using Matlab. Imp J Interdisc Res 2(8)
30. Friedman JM, Hunt ER, Mutters RG (2016) Assessment of leaf color chart observations for estimating maize chlorophyll content by analysis of digital photographs. Agron J 108(2):822–829

31. Reyes JF, Correa C, Zúñiga J (2017) Reliability of different color spaces to estimate nitrogen SPAD values in maize. Comput Electron Agric 143:14–22
32. Schwarz MW, Cowan WB, Beatty JC (1987) An experimental comparison of RGB, YIQ, LAB, HSV, and opponent color models. ACM Trans Grap (TOG) 6(2):123–158
33. Dalezios N et al (2001) Cotton yield estimation based on NOAA/AVHRR produced NDVI. Phys Chem Earth Part B 26(3):247–251
34. Moges S et al (2005) Evaluation of green, red, and near infrared bands for predicting winter wheat biomass, nitrogen uptake, and final grain yield. J Plant Nutr 27(8):1431–1441
35. Ren J et al (2008) Regional yield estimation for winter wheat with MODIS-NDVI data in Shandong, China. Int J Appl Earth Obs Geoinf 10(4):403–413
36. Barnhart I et al (2019) Evaluating sorghum senescence patterns using small unmanned aerial vehicles and multispectral imaging. Kansas Field Res 2019:166
37. Thompson CN et al (2019) Using normalized difference red edge index to assess maturity in cotton. Crop Sci 59(5):2167–2177
38. Ludovisi R et al (2017) UAV-based thermal imaging for high-throughput field phenotyping of black poplar response to drought. Front Plant Sci 8:1681
39. Rischbeck P et al (2016) Data fusion of spectral, thermal and canopy height parameters for improved yield prediction of drought stressed spring barley. Eur J Agron 78:44–59
40. Alganci U et al (2014) Estimating maize and cotton yield in southeastern Turkey with integrated use of satellite images, meteorological data and digital photographs. Field Crop Res 157:8–19
41. Jones HG (2004) Application of thermal imaging and infrared sensing in plant physiology and ecophysiology. Advances in Botanical Research. Academic Press, pp 107–163
42. Alchanatis V et al (2010) Evaluation of different approaches for estimating and mapping crop water status in cotton with thermal imaging. Precision Agric 11(1):27–41
43. Bajwa SG, Vories ED (2007) Spatial analysis of cotton (Gossypium hirsutum L.) canopy responses to irrigation in a moderately humid area. Irrig Sci 25(4):429–441
44. Bian J et al (2019) Simplified evaluation of cotton water stress using high resolution unmanned aerial vehicle thermal imagery. Remote Sens 11(3):267
45. Oosterhuis DM (1990) Growth and development of a cotton plant. Nitrogen nutrition of cotton: practical issues, pp 1–24
46. Ritchie GL et al (2007) Cotton growth and development. Cooperative Extension Service and the University of Georgia College of Agricultural and Environmental Sciences: Athens, GA, USA
47. Main CL (2012) W287 cotton growth and development. The University of Tennessee, Institute of Agriculture
48. Reinbott DL, Stevens G (2021) Cotton tillage and planting guidelines. [cited 2021 06/27]. https://extension.missouri.edu/publications/g4270
49. Celik A, Ozturk I, Way T (2007) Effects of various planters on emergence and seed distribution uniformity of sunflower. Appl Eng Agric 23(1):57–61
50. Sansone C et al (2002) Texas cotton production: emphasizing integrated pest management. Texas, USA: Texas Cooperative Extension Service, the Texas A & M University System
51. Supak J (1990) Making replant decisions. in 1990 Beltwide cotton production conference. National Cotton Council of America, pp 45–48
52. Goodell PB et al (2015) UC IPM pest management guidelines cotton. Oakland, CA
53. Vories E et al (2007) Estimating the impact of delaying irrigation for Midsouth cotton on clay soil. Trans ASABE 50(3):929–937
54. Vories E, Jones A (2016) Influence of irrigation patterns on the effectiveness of furrow irrigation of Cotton. In World Environmental and Water Resources Congress 2016
55. Vories ED et al (2015) Impact of soil variability on irrigated and rainfed cotton. J Cotton Sci 19(1):1–14
56. Forcella F et al (2000) Modeling seedling emergence. Field Crop Res 67(2):123–139
57. Ghassemi-Golezani K, Dalil B (2014) Effects of seed vigor on growth and grain yield of maize. Plant Breeding Seed Science 70(1):81–90

58. Wiles LJ, Schweizer EE (1999) The cost of counting and identifying weed seeds and seedlings. Weed Sci 47(6):667–673
59. Chen R et al (2018) Monitoring cotton (Gossypium hirsutum L.) germination using ultrahigh-resolution UAS images. Prec Agricul 19(1):161–177
60. Oh S et al (2020) Plant counting of cotton from UAS imagery using deep learning-based object detection framework. Remote Sens 12(18):2981
61. Lin Z, Guo W (2021) Cotton stand counting from unmanned aerial system imagery using mobilenet and centernet deep learning models. Remote Sens 13(14):2822
62. Huete AR (1988) A soil-adjusted vegetation index (SAVI). Remote Sens Environ 25(3):295–309
63. Zhao B et al (2018) Rapeseed seedling stand counting and seeding performance evaluation at two early growth stages based on unmanned aerial vehicle imagery. Front Plant Sci, 9
64. Adão T et al (2017) Hyperspectral imaging: A review on UAV-based sensors, data processing and applications for agriculture and forestry. Remote Sens 9(11):1110
65. Cobb JN et al (2013) Next-generation phenotyping: requirements and strategies for enhancing our understanding of genotype–phenotype relationships and its relevance to crop improvement. Theor Appl Genet 126(4):867–887
66. Perry C et al (2012) Cotton irrigation management for humid regions, in Cotton Incorporated, Cary, NC
67. Loka D (2012) Effect of water-deficit stress on cotton during reproductive development
68. Allen RG et al (1998) Crop evapotranspiration-Guidelines for computing crop water requirements-FAO Irrigation and drainage paper 56. Fao, Rome 300(9):D05109
69. Khan A et al (2018) Coping with drought: stress and adaptive mechanisms, and management through cultural and molecular alternatives in cotton as vital constituents for plant stress resilience and fitness. Biol Res 51(1):47
70. Ballester C et al (2019) Monitoring the effects of water stress in cotton using the green red vegetation index and red edge ratio. Remote Sens 11(7):873
71. Sullivan D et al (2007) Evaluating the sensitivity of an unmanned thermal infrared aerial system to detect water stress in a cotton canopy. Trans ASABE 50(6):1963–1969
72. Chang A et al (2020) Measurement of cotton canopy temperature using radiometric thermal sensor mounted on the unmanned aerial vehicle (UAV). J Sens, 2020
73. Zhou Z et al (2021) Assessment for crop water stress with infrared thermal imagery in precision agriculture: A review and future prospects for deep learning applications. Comput Elect Agricul 182:106019
74. Chen S et al (2020) Retrieval of cotton plant water content by UAV-based vegetation supply water index (VSWI). Int J Remote Sens 41(11):4389–4407
75. Nahiyoon SA et al (2020) Biocidal radiuses of cycloxaprid, imidacloprid and lambda-cyhalothrin droplets controlling against cotton aphid (Aphis gossypii) using an unmanned aerial vehicle. Pest Manag Sci 76(9):3020–3029
76. Kaivosoja J et al (2021) Reference measurements in developing UAV systems for detecting pests, weeds, and diseases. Remote Sens 13(7):1238
77. Meng Y et al (2019) Harvest aids efficacy applied by unmanned aerial vehicles on cotton crop. Indus Crops Prod 140:111645
78. Yi L et al (2019) Exploring the potential of UAV imagery for variable rate spraying in cotton defoliation application. Int J Prec Agricult Aviat 2(1)
79. Xin F et al (2018) Effects of dosage and spraying volume on cotton defoliants efficacy: a case study based on application of unmanned aerial vehicles. Agronomy 8(6):85
80. Lou Z et al (2018) Effect of unmanned aerial vehicle flight height on droplet distribution, drift and control of cotton aphids and spider mites. Agronomy 8(9):187
81. Yadav PK et al (2019) Assessment of different image enhancement and classification techniques in detection of volunteer cotton using UAV remote sensing. in Autonomous Air and Ground Sensing Systems for Agricultural Optimization and Phenotyping IV. 2019. International Society for Optics and Photonics

82. Puig E et al (2015) New developments in UAV remote sensing for pest management and the implications for cotton
83. Huang H et al (2018) A two-stage classification approach for the detection of spider mite-infested cotton using UAV multispectral imagery. Remote Sens Lett 9(10):933–941
84. Xu R et al (2018) Aerial images and convolutional neural network for cotton bloom detection. Front Plant Sci 8:2235
85. De Castro AI et al (2018) An automatic random forest-OBIA algorithm for early weed mapping between and within crop rows using UAV imagery. Remote Sens 10(2):285
86. Sapkota B et al (2020) Mapping and estimating weeds in cotton using unmanned aerial systems-borne imagery. Agri Eng 2(2):350–366
87. Wang T et al (2020) Automatic classification of cotton root rot disease based on UAV remote sensing. Remote Sens 12(8):1310
88. Xavier TW et al (2019) Identification of Ramularia leaf blight cotton disease infection levels by multispectral, multiscale UAV imagery. Drones 3(2):33
89. Wang T et al (2020) A plant-by-plant method to identify and treat cotton root rot based on UAV remote sensing. Remote Sens 12(15):2453
90. Thomasson J et al (2021) High-precision fungicide application for cotton disease based on UAV remote sensing. Precision agriculture'21. Wageningen Academic Publishers, pp 849–858
91. Deng X et al (2020) Detection and location of dead trees with pine wilt disease based on deep learning and UAV remote sensing. Agri Eng 2(2):294–307
92. Gao Z et al (2020) Deep learning application in plant stress imaging: a review. Agri Eng 2(3):430–446
93. Onder S et al (2005) Different irrigation methods and water stress effects on potato yield and yield components. Agric Water Manag 73(1):73–86
94. Bell JM et al (2018) Deficit irrigation effects on yield and yield components of grain sorghum. Agric Water Manag 203:289–296
95. Cuong TX et al (2017) Effects of silicon-based fertilizer on growth, yield and nutrient uptake of rice in tropical zone of Vietnam. Rice Sci 24(5):283–290
96. Schut AG et al (2018) Assessing yield and fertilizer response in heterogeneous smallholder fields with UAVs and satellites. Field Crop Res 221:98–107
97. Beres BL et al (2020) Towards a better understanding of Genotype× Environment× Management interactions–a global Wheat Initiative agronomic research strategy. Front Plant Sci 11:828
98. Feng A (2021) Quantifying the effect of environments on crop emergence, development and yield using sensing and deep learning techniques. University of Missouri--Columbia
99. Komm B, Moyer M (2015) Vineyard yield estimation
100. Feng A et al (2019) Cotton yield estimation from UAV-based plant height. Trans ASABE 62(2):393–404
101. Yeom J et al (2018) Automated open cotton boll detection for yield estimation using unmanned aircraft vehicle (UAV) data. Remote Sens 10(12):1895
102. Xu W et al (2020) Establishing a model to predict the single boll weight of cotton in northern Xinjiang by using high resolution UAV remote sensing data. Comput Electr Agricul 179:105762
103. Xu W et al (2021) Cotton yield estimation model based on machine learning using time series UAV remote sensing data. Int J Appl Earth Observ Geoinf 104:102511
104. Maimaitijiang M et al (2020) Soybean yield prediction from UAV using multimodal data fusion and deep learning. Remote Sens Environ 237:111599
105. Yang Q et al (2019) Deep convolutional neural networks for rice grain yield estimation at the ripening stage using UAV-based remotely sensed images. Field Crop Res 235:142–153
106. Zhang M et al (2020) Estimation of maize yield and effects of variable-rate nitrogen application using UAV-based RGB imagery. Biosys Eng 189:24–35
107. Ashapure A et al (2020) Developing a machine learning based cotton yield estimation framework using multi-temporal UAS data. ISPRS J Photogramm Remote Sens 169:180–194

108. Schwalbert RA et al (2020) Satellite-based soybean yield forecast: Integrating machine learning and weather data for improving crop yield prediction in southern Brazil. Agricult Forest Meteor 284:107886
109. Chu Z, Yu J (2020) An end-to-end model for rice yield prediction using deep learning fusion. Comput Elect Agricul 174:105471
110. Khaki S, Wang L (2019) Crop yield prediction using deep neural networks. Front Plant Sci, 10
111. Khaki S, Wang L, Archontoulis SV (2020) A cnn-rnn framework for crop yield prediction. Front Plant Sci 10:1750
112. Lipton ZC, Berkowitz J, Elkan C (2015) A critical review of recurrent neural networks for sequence learning. arXiv preprint arXiv:1506.00019
113. Lee SH et al (2020) Attention-based recurrent neural network for plant disease classification. Front Plant Sci, 11

Chapter 4
Time Effect After Initial Wheat Lodging on Plot Lodging Ratio Detection Using UAV Imagery and Deep Learning

Zhao Zhang, Cannayen Igathinathane, Paulo Flores, Yiannis Ampatzidis, Hu Liu, Jithin Mathew, and Anup Kumar Das

Abstract Wheat is an indispensable staple crop worldwide, and lodging is a key yield-limiting factor. Timely assessment of wheat lodging conditions in an accurate and objective manner is important for a number of stakeholders. Since the conventional approach based on visual observation during field visits is inefficient, laborious, subjective, and unreliable, there is a need for an automatic methodology to replace the manual approach. In this study, an excess green based approach developed for automatic dataset generation of field plots, extracted from the whole experimental field image collected through an unmanned aerial vehicle (UAV), can be readily applied to similar workflows. For the wheat lodging ratio (three grades considered) detection, from the comparison of the deep features by ResNet50 and GoogLeNet coupled with support vector machine (SVM) classifier, it was recommended to adopt the deep features by ResNet50 for its higher detection accuracy. The selected ResNet50 deep features compared with the handcrafted features showed that the deep features generated higher accuracy, while being simpler to apply and not requiring domain knowledge resulting in automatic features extraction for wheat

Z. Zhang (✉)
Key Lab of Smart Agriculture System Integration, Ministry of Education, China Agricultural University, Beijing 100083, P.R. China
e-mail: zhaozhangcau@cau.edu.cn

Key Lab of Agriculture Information Acquisition Technology, Ministry of Agriculture of China, China Agricultural University, Beijing 100083, China

C. Igathinathane · P. Flores · J. Mathew · A. K. Das
Department of Agricultural and Biosystems Engineering, North Dakota State University, Fargo, ND 58102, USA

Y. Ampatzidis
Agricultural and Biological Engineering Department, Southwest Florida Research and Education Center, University of Florida, IFAS, 2685 SR 29 North, Immokalee, FL 34142, USA

H. Liu
Northwest Institute of Eco-Environment and Resources, Chinese Academy of Sciences, Lanzhou 730000, China

Linze Inland River Basin Research Station, Chinese Ecosystem Research Network, Lanzhou 730000, China

Z. Zhang et al. (eds.), *Unmanned Aerial Systems in Precision Agriculture*,
Smart Agriculture 2, https://doi.org/10.1007/978-981-19-2027-1_4

lodging ratio detection. Time effect after initial lodging occurrence results indicate that the UAV mission data should be collected soon after lodging occurrence, which would generate higher detection accuracy due to better color contrast in the earlier stage and avoid the nature color loss during crop ripening leading to reduced detection accuracy. Unlike GoogLeNet and handcrafted features, the ResNet50 features produced a robust model, and the prediction accuracy did not reduce in the time frame of the first and second weeks after the initial lodging. This study has demonstrated that the application of automatic dataset generation method on UAV images of the experimental field, collected sooner (1–2 weeks) after the initial lodging, using deep features extracted by ResNet50 coupled with SVM classifier is an efficient approach for wheat lodging ratio detection, with an accuracy over 70%.

Keywords Wheat lodging · Support vector machine · ResNet50 · Handcrafted features · Deep features · Field crop

4.1 Introduction

As one of the most important staple crops worldwide, wheat provides a number of essential or beneficial nutrients for health, which include, but are not limited to, protein, vitamins (especially B), iron, and fibers [1]. A relationship between wheat consumption and reduced risk of cardiovascular disease, diabetes, and colorectal cancer has been established [2–4]. Although the global wheat production has been steadily growing since 2018, it hit a historical record high of 7.7×10^{11} kg in 2020 [5]; however, there are several factors limiting the wheat yield, such as crop diseases [6, 7], drought [8, 9], and lodging [10], among which lodging ranks the top [11].

Wheat lodging is defined as the displacement of plant stems from their upright position, which could be caused by strong winds, heavy rain, high planting density, or improper nutrient management [12]. After lodging occurs, crops underlying would be sunshine blocked, and this could reduce their photosynthesis rate. It has been reported that the lowered photosynthesis rate would reduce the yield by up to 80% [13]. In addition, the occurrence of lodging would cause harvest challenges as the lowered crops are difficult to be pulled into the combine header [14]. Obtaining wheat lodging information in a timely, accurately, and objectively manner would be beneficial for a variety of reasons: helping breeders with the selection of resistant cultivars, assisting agronomists to identify the proper nutrient management strategies (e.g., nitrogen rate), and providing a repeatable approach for crop insurance personnel in processing the insurance coverage [15].

Even though many state-of-the-art automation and sensing technologies have already been efficiently and successfully employed in several practical agricultural applications [16–22], the current approach for wheat lodging detection is still based on visual observation, and the raters (field inspectors) have to visit the fields to manually judge the lodging conditions [10, 23]. The manual approach is known

to have a number of shortcomings. First of all, the assessment process is time-consuming, as raters have to visit and evaluate each plot. Second, it is infeasible for raters to get access to the field under certain conditions, such as immediately after a heavy rain. Third, the tough working conditions (e.g., high temperature and humidity) and laboriousness of the process makes it impossible for workers to be exposed to the field for a long time. Fourth, the evaluation results are subjective as different raters may provide inconsistent (intra-rater difference) results [15]. To avoid all these shortcomings associated with manual evaluation, it is desirable to develop a quick, automatic, objective, and reliable approach for wheat lodging detection.

During the past decades, numerous researchers have explored and tested different approaches for automatic crop lodging detection [24]. Li et al. [25, 26], Yang et al. [27], and Zhao et al. [28] have explored the potential of using satellite images for crop lodging detection. Though the satellite images are able to cover a large field area, their practical application has been significantly limited by their both low spatial (tens of centimeter) and temporal (multiple days) resolution [10]. Furthermore, the satellite images mainly use spectral differences between lodging and non-lodging crops for the classification. However, due to the large distances between the satellite and crops, the spectral signal is generally weak, which would lower the classification accuracy [29]. Very recently, with the rapid technological progress on both hardware and its associated software program for data processing, unmanned aerial vehicles (UAVs) are gradually applied by researchers for crop lodging detection [10, 30, 31]. The UAVs can overcome some of the shortcomings of satellite images. Researchers can fly the UAV at any desired intervals and lower heights that greatly and significantly improves the temporal and image resolution; whenever the weather permits (e.g., no rain and wind speed $\leq$ 25 km/h). Moreover, researchers can collect UAV aerial images at the maximum height of 120 m [32], and the images can be of millimeter-level resolution, which is finer than that of satellite images. In addition, as the costs of UAVs and their associated data process software nowadays getting down rapidly and significantly, making it affordable and profitable for agricultural applications [10]. Hence, taking advantage of UAV technology for wheat lodging detection is a new approach that is worthy of exploration.

When testing the performance of different varieties on resistance to lodging, breeders would usually conduct a comprehensive and thorough study, in which way they usually grow hundreds or even thousands of plots as experimental trails. Using UAV aerial images for crop lodging detection starts with the preparation of datasets. After collecting and pre-processing individual aerial images to obtain orthomosaic maps, researchers usually use a manual approach for dataset (e.g., individual plot images) creation, which is time-consuming and inaccurate [22]. Only a few studies developed or tested an automatic method for dataset generation, and it is probably because of the challenging nature of the task. When the boundaries between plots are small (e.g., experimental field plots) and when the lodging occurs, the lodged crops would cover the small boundary—making it difficult to segment the plot using simple contour detection. An automatic plot dataset generation method was not developed and reported so far. In addition, a lot of existing studies treat wheat lodging as a

binary issue—lodging or non-lodging [10]. However, breeders are more interested in the lodging ratio (a range of scores) for each plot.

In the analysis, after obtaining the individual plot images, usually the image features are extracted and then different classifiers for training and testing are applied, in which proper feature selection is critical for the detection accuracy. If the selected features can represent the images satisfactorily, the trained model would have a good performance; otherwise, the model accuracy would be reduced. The selection of proper features requires domain knowledge, and this is a challenging task by users. In recently years, with the advent of deep learning, researchers started to test the performance of deep features extracted by deep learning models (convolutional neural network) on crop lodging detection. Even though a number of popular deep learning models that can be used for deep features extraction exist, only a few studies have been conducted to determine the model that gave the highest accuracy. Furthermore, the performance of handcrafted versus deep features on wheat lodging detection has not been compared and which choice to be made are not explored yet.

Current studies on crop lodging detection usually take the UAV mission immediately after the lodging occurs. Crop lodging, however, is a dynamic process, therefore information on the optimal time window after the initial lodging for the UAV mission is essential, and this could generate the aerial images leading to the highest detection accuracy.

Give these research opportunities, the objectives of this study were to: (1) develop an automatic approach for dataset generation for plot delineation in wheat lodging study, (2) identify the deep learning models that could extract deep features to generate the highest detection accuracy, (3) compare the accuracies generated by deep and handcrafted features coupled with support vector machine (SVM) classifier, and (4) explore the time effect after initial lodging on the model accuracy.

4.2 Materials and Methods

The various procedures followed in this study for developing an automatic plot dataset generation methodology, identifying the desirable deep learning models that could extract the deep features for higher detection accuracy, comparing the deep features versus handcrafted features on lodging ratio detection, and explore the optimal time after initial lodging for data collection are schematically shown in Fig. 4.1. After initial lodging, the UAV images were collected approximately on 1, 2, and 4 weeks after the event. For each date UAV mission, the images were first processed to generate orthomosaic maps, which was followed by the creation of the individual plot images as the dataset using a new dataset generation approach. Two deep learning models, namely ResNet50 and GoogLeNet, were used to extract deep features, and after applying the SVM classifier on extracted deep features, the model with a higher lodging detection accuracy was selected. Then, the accuracy comparison between the selected deep learning models and handcrafted features was conducted to select the more satisfactory one. The time effect after initial lodging was finally compared

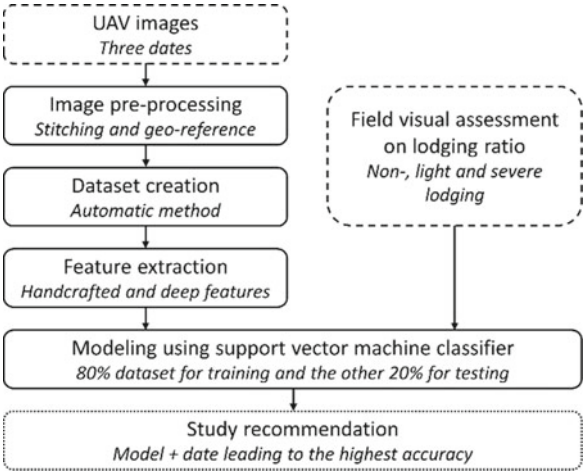

Fig. 4.1 General procedure flowchart of wheat lodging detection on different dates after it occurred using an unmanned aerial vehicle (UAVs) coupled with handcrafted and deep features associated with support vector machine classifier

on the three dates' dataset with the best time for UAV mission recommended. Details of the different processes of the study are described subsequently in the appropriate sections.

4.2.1 Experimental Field and Data Collection

The experimental trials used in this study were planted during the summer of 2020 in Thompson, ND, U.S. (Fig. 4.2). There are two plot sizes, namely short: 1.5 × 3.6 m (5 × 12 ft) and long: 1.5 × 14.6 m (5 × 48 ft). There are a total of 428 plots, consisting of 312 short and 116 long plots, among which 28 plots serving as borders

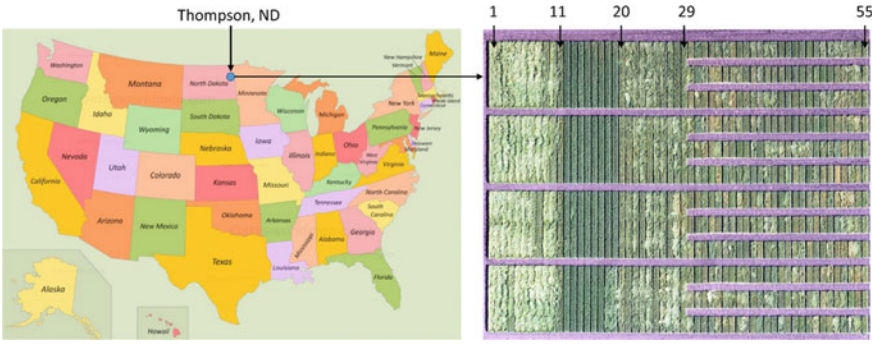

Fig. 4.2 Layout and location of experimental fields for wheat lodging study—312 short plots (1.5 × 3.6 m; columns 30 to 55) and 116 long plots (1.5 × 14.6 m; columns 1 to 29). The border plots (indicated by columns 1, 11, 20, 29, and 55) are not used in this study

(columns 1, 11, 20, 29, and 55 in the right photo of Fig. 4.2; and columns 1 and 55 are on the left and right borders of the experimental field, respectively) that were excluded from the analysis.

The lodging occurred roughly in the middle of July, 2020, and after the lodging occurred, three UAV missions were conducted on July 23, July 28, and Aug 11, 2020: approximately 1, 2, and 4 weeks after the initial lodging occurred. Hereafter, the three dates are indicated as date 1, 2, and 3, corresponding to July 23, July 28, and Aug 11, 2020, respectively, for nomenclature. A DJI Phantom 4D RTK UAV (DJI-Innovations, Inc., Shenzhen, China) was used for data collection, which is outfitted with a 20 megapixel (5,472 × 3,648 pixel) color camera. The mission speed was set to 2.5 m/s. Since the weather was sunny during the entire data collection time window, the balance mode was set as sunny. Both side and forward overlaps for image capture were set as 80%. For each date, the data collection was obtained between 10:00 AM and 12:00 PM. When the UAV mission height is low (e.g., 15 m), the collected images are finer (high resolution) but the data collection time is long; when the mission height is high (e.g., 91 m), the collected images are coarse (low resolution), but the data collection time is short. Our preliminary study results showed using the 91 m mission height would not hurt the detection accuracy on wheat lodging detection [24]. Therefore, to have a higher data collection efficiency for the purpose of wheat lodging identification, 91 m height was chosen as the UAV data collection height in this study.

After each flight, two inspectors visited the field and visually assessed each plot's lodging ratio. The inspectors were trained by an experienced expert before conducting the field evaluation. These inspectors worked independently without any communication between each other during the entire evaluation process to avoid influence on the other. For individual plot, each inspector provided one grade among the three categories: non-lodging (grade 1)—lodging does not occur; light lodging (grade 2)—lodging area accounting for < 50% of the total area; and severe lodging (grade 3)—lodging area accounting for > 50% of the total area. The visually evaluated results were used for model training and testing.

4.2.2 Data Pre-Processing and Auto Dataset Generation

After each UAV mission, all the images taken were pre-processed using Pixel4D (Pix4D V4.3.33, S.A., Prilly, Switzerland) to generate an orthomosaic map (Fig. 4.2 right image). Thus, for each date, an orthomosaic map was created, after which the three individual orthomosaic maps were geo-referred using ground control points as references.

The next step is to prepare the dataset based on the three orthomosaic maps, consisting of all the individual plots. In the vertical direction, the experiment field consists of four large blocks, and since the four blocks are similar and the automatic dataset creation method generated for either block can be used for all other three plots without modification, the top block in the right image of Fig. 4.2 is used to

explain the developed automatic dataset generation method. Additionally, since all the three dates' orthomosaic maps were geo-referred, indicating they are pixel-to-pixel matching, the automatic dataset generation method generated for either of the three orthomosaic maps could be directly used for the other two.

The crucial point is to identify and segment the individual plot, and there are a lot of algorithms that can be used for edge detection. However, the edge detection would not function as for the serious lodging plots, the lodged crops cover the boundary between the plots. Hence, instead of detecting the edges, the methodology developed in this study utilizes the excess green index (Eq. 4.1) to separate crops from the background, and then detect the general block boundary, based on which individual plot's coordinates would be obtained for automatic plot image generation (Fig. 4.3).

$$\text{Excess Green} = 2 \times \text{Green Channel} - \text{Red Channel} - \text{Blue Channel} \quad (4.1)$$

The automatic dataset generation starts from calculating the excess green index of each pixel, which has been demonstrated as a satisfactory index to distinguish crop from soil [33]. With the excess green monochrome image (Fig. 4.3b), a threshold of 0.01 is used to generate a binary image (Fig. 4.3c) with the pixel values as 0 or 1, after which the noises (holes in the image) indicated by black regions are removed. From the noise-removed binary image (Fig. 4.3d), the critical operation is to identify the main boundaries in the horizontal direction (denoted as R1-R6 in Fig. 4.3d) and vertical direction (denoted as C1 and C2 in Fig. 4.3d). After determining the C1 and C2 coordinates, coupled with the known information of plot numbers, each plot's horizontal coordinates (between C1 and C2) can be calculated. To obtain the R1-R6, each row's pixel value is added (black pixel = 0 and white pixel = 1), and row sums

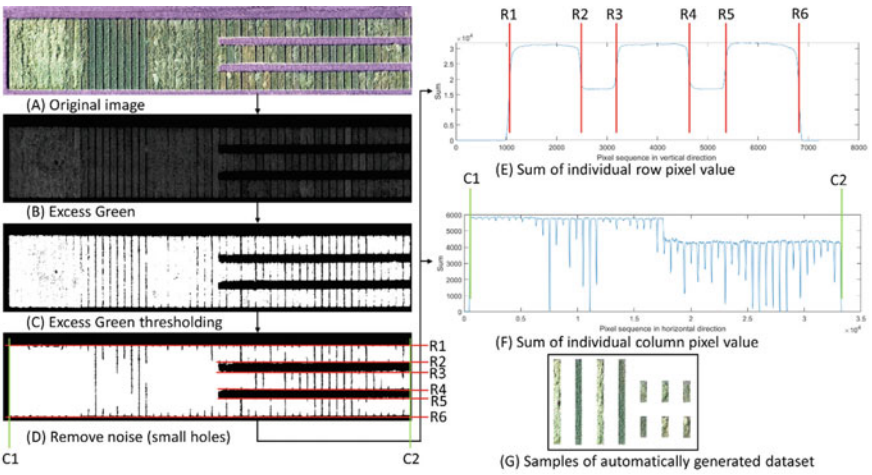

Fig. 4.3 Developed methodology for automatic dataset generation for individual wheat lodging plot from the experimental field

were computed. From top to bottom (Fig. 4.3d), when the row sum value changes suddenly (caused by the pathways black pixels: R2-R3 and R4-R5; Fig. 4.3d), the row number is determined as the boundary, which is graphically illustrated in Fig. 4.3e. Applying the same analogy, C1 and C2 values (left and right edge of the field) in Fig. 4.3d are obtained as well, with detailed column pixel sum process shown in Fig. 4.3f. Thus, each plot's coordinates are obtained, based on which individual plot's image is generated by cropping operation. Samples of automatically generated images are shown in Fig. 4.3g.

By manually removing the border plots from the total plots' image, the final dataset consisting of 400 plots (100 long and 300 short) is obtained. For the field evaluation results, after two inspectors completed the visual inspection and the orthomosaic map is generated, the two inspectors and a third personal together compared their inspection results: if the two results are the same, it would remain as the final ground truth data; if the two results are different, the three persons would use the plot image from the generated orthomosaic map to vote for the final grade of this plot. The 400 plots images, coupled with their corresponding ground truth data, combine the final dataset.

4.2.3 Handcrafted Features

The handcrafted features are indices that are extracted from the images to represent their characteristics based on the domain knowledge related to wheat lodging image analysis. Color features have been demonstrated to be able to describe the characteristics of lodged and non-lodged crops [34]. The original plot images are in RGB (red, green, and blue) format, and then they were converted into HSI (hue, saturation, and intensity) and Lab (L for the lightness and a and b for the color dimensions) formats, which lead to a total of 9 channel color features. In addition to the color features, a variety of vegetation fractions were extracted, including normalized difference index, excess green, excessive red index, color index of vegetation extraction, modified excessive index, and normalized excess green index. Moreover, texture features (e.g., correlation, contrast, dissimilarity, energy, entropy, and homogeneity) were extracted to improve the comprehensiveness of the features for better representation of the images. The definition of these common indices and their calculation formulas can be found elsewhere [16].

4.2.4 Deep Features

Compared to the handcrafted features that require domain knowledge for proper selection, the extraction of deep features is not involved with any domain knowledge, which is automatically extracted by a convolutional neural network (CNN). Since a number of deep learning models consisting of CNN have existed, the existing deep

Table 4.1 Detailed information of deep learning models used in this study for deep feature extraction

Model parameters	ResNet50	GoogLeNet
Pooling layer	Avg_pool	Pool-drop_7 × 7_s1
Number of features	2048	1024

learning models for deep feature extraction can be utilized. In this study, ResNet50 and GoogLeNet models were selected for deep feature extraction based on their satisfactory performance in previous studies [6, 35]. Detailed information, including the feature pooling layers and number of features, is shown in Table 4.1.

4.2.5 Classifier

A proper classifier for training and testing that uses all these features is essential. A large number of classifiers have been demonstrated to have a satisfactory performance, such as neural network, random forest, and support vector machine (SVM), among which SVM was selected for its demonstrated better performance [35].

The full dataset was divided into two parts as training and testing, with randomly selected 80% for training and the other 20% for testing. Since each time the 80% training dataset is randomly assigned, to have an objective comparison, in this study, 10 replications were run, with the average accuracy used to represent the model's performance. The above procedures for imaging processing, dataset generation, feature extraction, and modeling were performed in MATLAB® R2020a (The Mathworks, Inc., Natick, Mass., USA). A desktop computer was used for data processing, which had a configuration of Windows 10 OS, Intel(R) Core(TM) i7-8700 CPU, 32 GB RAM, Intel(R) UHD Graphics 630, and 16 G GPU memory.

4.3 Results and Discussion

4.3.1 Deep Learning Model Selection for Deep Feature Extraction

The accuracy comparison of deep features extracted by ResNet50 and GoogLeNet on three dates is presented in Fig. 4.4. For all the three dates, the deep features extracted by ResNet50 are consistently higher than that by GoogLeNet, and the accuracy differences are 7, 11, and 6%, for date 1, 2, and 3, respectively. A potential reason is that the RestNet50 has more deep layers than GoogLeNet, and more (deep) CNN layers would help extract finer features over shallow (less) layers. The fine features have a better representation of the image characteristics. Hence, it is better to choose ResNet50, not GoogLeNet for deep feature extraction for better detection

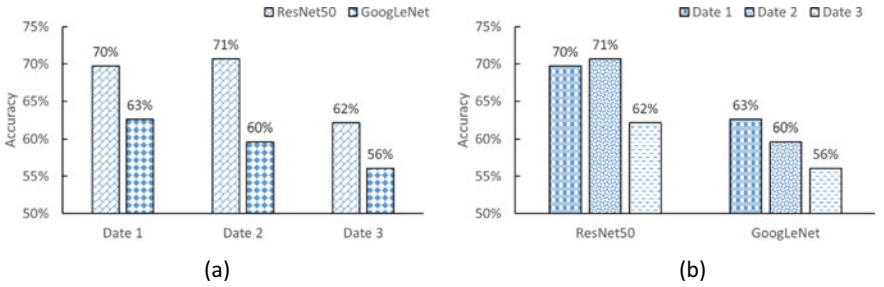

Fig. 4.4 Model accuracy comparison for deep features with support vector machine classifier in terms of dates (**a**) and different models (**b**). Date 1, 2, and 3 denotes July 23, July 28, and Aug 11, 2020, respectively

accuracy. When comparing the performance of deep features extracted from two models in terms of three dates (Fig. 4.4b), the last date would consistently generate the lowest accuracy, which would be probably caused by the ripening of the crop and associated natural color change. When the crops are not ripe, the stems (lodged part) represent different characteristics from the leave (non-lodged part). However, when crops are ripe, the feature difference caused by chlorophyll would be smaller due to the reduced chlorophyll content caused by ripening.

4.3.2 Comparison of Handcrafted and Deep Features

The model accuracy based on handcrafted features evaluated using the SVM classifier is presented in Fig. 4.5. With the progress of time, the detection accuracy goes down. The highest accuracy is generated by the first date's dataset (65%), and this is probably due to better contrast between the greener standing crop exposing the leaves and the lodged crop exposing the stems that are less green. Furthermore, with time the crops mature and the chlorophyll content goes down, thereby the difference in the contrast

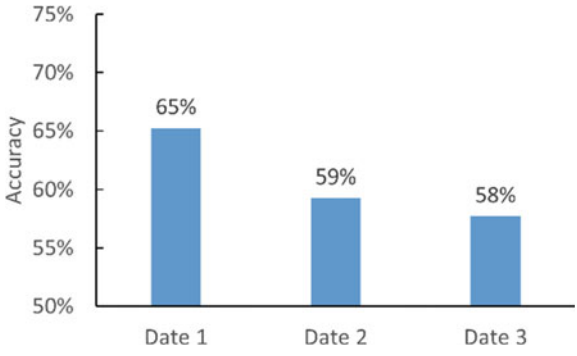

Fig. 4.5 Detection accuracy based on handcrafted features for three dates. Date 1, 2, and 3 denote July 23, July 28, and Aug 11, 2020, respectively

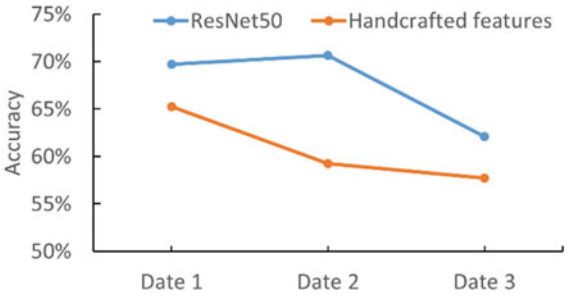

Fig. 4.6 Accuracy comparison between deep and handcrafted features using support vector machine classifier. Date 1, 2, and 3 denotes July 23, July 28, and Aug 11, 2020, respectively

of the regular and lodged crops also reduces. This result agrees with the deep features' results that the last date's dataset generated the lowest accuracy (58%). Thus it is desirable to take the aerial image one or two weeks (sooner) after the initial lodging of the crop, instead of 4 weeks after the event. In addition, this suggestion also provides early assessment and allows time for possible crop management or insurance-related processing.

The accuracy comparison between the deep features extracted by ResNet50 (best among deep learning models tested) and handcrafted features are compared for the three study dates (Fig. 4.6). For all the three dates' datasets, deep features by ResNest50 have better performance (higher accuracy) than the handcrafted features. A potential reason is that the deep features can extract finer features over the handcrafted features. This indicates that using deep features by ResNet50 would be a better choice than using handcrafted features. In addition to higher accuracy, application of the deep features would require minimal or no domain knowledge, making it an easy-to-use and reliable approach. Furthermore, the initial window of assessing the wheat lodging using ResNet50 is broader with no loss of accuracy (Dates 1 and 2) unlike handcrafted features with reducing accuracy with dates after initial lodging.

Regarding the time for data collection to result into higher accuracy, it is recommended to collect the aerial images sooner after the lodging occurs. In the early data collection, the crops are still green, and the extracted features would better represent the crop characteristics. With the time elapsed, crops are gradually maturing, and the crops are turning from green to yellow, making it difficult to distinguish the lodged from non-lodged crops. However, it is interesting to observe the ResNet50 prediction accuracy did not reduce in the time frame of the first and second weeks after the initial lodging (Fig. 4.6) unlike GoogLeNet (Fig. 4.4) and handcrafted features (Fig. 4.6), which may be due to the robustness of the ResNet50 and the inclusion of several additional features than the other methods.

4.4 Conclusion

To avoid a number of shortcomings of the widely adopted manual/visual method (e.g., inefficient, laborious, subjective, unreliable) in wheat lodging ratio detection,

a methodology of using aerial images by unmanned aerial vehicles (UAVs) coupled with the machine learning support vector machine (SVM) method was developed. A new approach for automatic dataset (plot images) generation was developed and tested in this study gave a satisfactory performance, and it can be extended/applied by others on similar workflows. Deep features extracted by ResNet50 performed more satisfactorily with higher accuracy than those by GoogLeNet. Between the selected deep features (ResNet50) and handcrafted features (color + texture + vegetation fraction), it is concluded to select the deep features due to their model higher accuracy and simplicity (free of domain knowledge). Regarding the data collection time after initial lodging, it is recommended to collect the UAV data sooner after the lodging occurrence for higher detection accuracies. The ResNet50 prediction accuracy did not reduce in the time frame of the first and second weeks after the initial lodging because of robustness unlike GoogLeNet and handcrafted features. This study has demonstrated that using deep features extracted by ResNet50 coupled with SVM classifier on UAV aerial images collected sooner (1–2 week) after the lodging occurs is an efficient approach for wheat lodging ratio detection, with an accuracy over 70%.

Acknowledgements Authors thanks Jensen Kenton for preliminary data processing of the UAV images, including stitching using Pixle4D and geo-referring the images using ArcGIS10. The authors would also like to thank Singh Shreya and Gurram Vikranth Reddy for field data collection, and Eisinger Darin and Chad Deplazes for preparing the experimental fields. This work was jointly supported by North Dakota Agricultural Experiment Station (NDAES) Precision Agriculture Graduate Research Assistantship and USDA Agricultural Research Service Project No. 6064-21660-001-32S. Project accession No. 435589.

References

1. Shewry PR, Hey SJ (2015) The contribution of wheat to human diet and health. Food Energy Sec 4(3):178–202
2. Humphreys KJ, Conlon MA, Young GP, Topping DL, Hu Y, Winter JM, ..., Le Leu RK (2014) Dietary manipulation of oncogenic microRNA expression in human rectal mucosa: a randomized trial. Cancer Prevent Res 7(8):786–795
3. Keenan MJ, Martin RJ, Raggio AM, McCutcheon KL, Brown IL, Birkett A, ... Zhou J (2012) High-amylose resistant starch increases hormones and improves structure and function of the gastrointestinal tract: a microarray study. Lifestyle Genom 5(1):26–44
4. Lobley GE, Holtrop G, Bremner DM, Calder AG, Milne E, Johnstone AM (2013) Impact of short term consumption of diets high in either non-starch polysaccharides or resistant starch in comparison with moderate weight loss on indices of insulin sensitivity in subjects with metabolic syndrome. Nutrients 5(6):2144–2172
5. Statista (2021) Global wheat production from 2011/2012 to 2020/2021. https://www.statista.com/statistics/267268/production-of-wheat-worldwide-since-1990/
6. Jahan N, Flores P, Liu Z, Friskop A, Mathew JJ, Zhang Z (2020) Detecting and distinguishing wheat diseases using image processing and machine learning algorithms. ASABE Paper No. 2000372. St. Joseph, MI: ASABE
7. Ma Z, Xie Q, Li G, Jia H, Zhou J, Kong Z, ... ,Yuan Y (2020) Germplasms, genetics and genomics for better control of disastrous wheat Fusarium head blight. Theoret Appl Genet 133(5):1541–1568

8. Webber H, Ewert F, Olesen JE, Müller C, Fronzek S, Ruane AC, ..., Wallach D (2018) Diverging importance of drought stress for maize and winter wheat in Europe. Nat Commun 9(1):1–10
9. Yang J, Wu J, Liu L, Zhou H, Gong A, Han X, Zhao W (2020) Responses of winter wheat yield to drought in the north China plain: spatial-temporal patterns and climatic drivers. Water 12(11):3094
10. Zhang Z, Flores P, Igathinathane CL, Naik D, Kiran R, Ransom JK (2020a) Wheat lodging detection from UAS imagery using machine learning algorithms. Remote Sens 12(11):1838
11. Chauhan S, Darvishzadeh R, Boschetti M, Pepe M, Nelson A (2019) Remote sensing-based crop lodging assessment: current status and perspectives. ISPRS J Photog Remote Sens 151:124–140
12. Wu W, Ma BL (2016) A new method for assessing plant lodging and the impact of management options on lodging in canola crop production. Sci Rep 6(1):1–17
13. Setter TL, Laureles EV, Mazaredo AM (1997) Lodging reduces yield of rice by self-shading and reductions in canopy photosynthesis. Field Crop Res 49(2–3):95–106
14. Islam MS, Peng S, Visperas RM, Ereful N, Bhuiya MSU, Julfiquar AW (2007) Lodging-related morphological traits of hybrid rice in a tropical irrigated ecosystem. Field Crop Res 101(2):240–248
15. Yang MD, Huang KS, Kuo YH, Tsai HP, Lin LM (2017) Spatial and spectral hybrid image classification for rice lodging assessment through UAV imagery. Remote Sens 9(6):583
16. Flores P, Zhang Z, Igathinathane C, Jithin M, Naik D, Stenger J, ..., Kiran R (2021) Distinguishing seedling volunteer corn from soybean through greenhouse color, color-infrared, and fused images using machine and deep learning. Ind Crops Prod 161:113223
17. Lu R, Zhang Z, Pothula AK (2017) Innovative technology for apple harvest and in-field sorting. Fruit Quart 25(2):11–14
18. Pothula AK, Zhang Z, Lu R (2018) Design features and bruise evaluation of an apple harvest and in-field presorting machine. Trans ASABE 61(3):1135–1144
19. Yao L, Hu D, Zhao C, Yang Z, Zhang Z (2021) Wireless positioning and path tracking for a mobile platform in greenhouse. Int J Agricult Biol Eng 14(1):216–223
20. Zhang J, Wan L, Igathinathane C, Zhang Z, Guo Y, Sun D, Cen H (2021a) Spatiotemporal heterogeneity of chlorophyll content and fluorescence response within rice (Oryza sativa L.) canopies under different nitrogen treatments. Front Plant Sci 12:499
21. Zhang Z, Heinemann PH, Liu J, Baugher TA, Schupp JR (2016) The development of mechanical apple harvesting technology: a review. Trans ASABE 59(5):1165–1180
22. Zhang Z, Igathinathane C, Li J, Cen H, Lu Y, Flores P (2020b) Technology progress in mechanical harvest of fresh market apples. Comput Elect Agricul 175:105606
23. Piñera-Chavez FJ, Berry PM, Foulkes MJ, Jesson MA, Reynolds MP (2016) Avoiding lodging in irrigated spring wheat. I. Stem and root structural requirements. Field Crop Res 196:325–336
24. Zhang Z, Igathinathane C, Flores P, Mathew J, Ransom J, Ampatzidis Y (2021b) UAV mission height effects on wheat lodging ratio detection. ASABE Paper No. 2100119. St. Joseph, MI: ASABE
25. Li X, Wang K, Ma Z, Wang H (2014) Early detection of wheat disease based on thermal infrared imaging. Transact Chinese Soc Agricult Eng 30(18):183–189
26. Li Z, Chen Z, Wang L, Liu J, Zhou Q (2014) Area extraction of maize lodging based on remote sensing by small unmanned aerial vehicle. Transact Chinese Soc Agricult Eng 30(19):207–213
27. Yang H, Chen E, Li Z, Zhao C, Yang G, Pignatti S, ..., Zhao L (2015) Wheat lodging monitoring using polarimetric index from RADARSAT-2 data. Int J Appl Earth Observ Geoinf 34:157–166
28. Zhao L, Yang J, Li P, Shi L, Zhang L (2017) Characterizing lodging damage in wheat and canola using Radarsat-2 polarimetric SAR data. Remote Sens Lett 8(7):667–675
29. Liu T, Li R, Zhong X, Jiang M, Jin X, Zhou P, ..., Guo W (2018) Estimates of rice lodging using indices derived from UAV visible and thermal infrared images. Agricult Forest Meteorol 252:144–154
30. Wilke N, Siegmann B, Klingbeil L, Burkart A, Kraska T, Muller O, ..., Rascher U (2019) Quantifying lodging percentage and lodging severity using a UAV-based canopy height model combined with an objective threshold approach. Remote Sens 11(5):515

31. Yang MD, Tseng HH, Hsu YC, Tsai HP (2020) Semantic segmentation using deep learning with vegetation indices for rice lodging identification in multi-date UAV visible images. Remote Sens 12(4):633
32. U.S. Federal Aviation (2021). https://www.faa.gov/
33. Flores P, Zhang Z, Mathew J, Jahan N, Stenger J (2020) Distinguishing volunteer corn from soybean at seedling stage using images and machine learning. Smart Agric 2(3):61
34. Wang A, Zhang W, Wei X (2019) A review on weed detection using ground-based machine vision and image processing techniques. Comput Electron Agric 158:226–240
35. Aballa A, Cen H, Wan L, Mehmood K, He Y (2020) Nutrient status diagnosis of infield oilseed rape via deep learning-enabled dynamic model. IEEE Trans Industr Inf 17(6):4379–4389

Chapter 5
UAV Mission Height Effects on Wheat Lodging Ratio Detection

Zhao Zhang, Cannayen Igathinathane, Paulo Flores, Jithin Mathew, Joel Ransom, Yiannis Ampatzidis, and Anup Kumar Das

Abstract Wheat is an important staple crop worldwide, and lodging is a negative factor contributing to yield reduction. Obtaining timely and accurate wheat lodging information is critical. Using unmanned aerial vehicle (UAV) images for wheat lodging detection is a relatively new approach, in which researchers usually apply the manual method for field plot dataset generation. Considering the manual method being inefficient, inaccurate, and subjective, the study developed an image processing-based new approach for automatic field plot dataset generation and tested. Since only a few studies explored the effects of different UAV mission heights on wheat lodging ratio detection, we conducted experiments at three mission heights (15, 45, and 91 m) and analyzed images using machine learning (support vector machine—SVM) and deep learning (Resnet50) algorithms for wheat lodging ratios (3 grades) detection. The results indicated that the collected images on 91 m (2.5 cm/pixel) mission height could generate a similar or even a little higher detection accuracy over the images collection at 45 m (1.2 cm/pixel) and 15 m (0.4 cm/pixel) height. Comparison of SVM and Resnet50 model results showed that SVM resulted in more satisfactory performance (67.6% accuracy) with slightly higher accuracy over Resnet50 (67.2% accuracy) at 2.5 cm/pixel resolution. This study recommends that UAV images collected at the height of about 91 m (2.5 cm/pixel resolution),

Z. Zhang (✉)
Key Lab of Smart Agriculture System Integration, Ministry of Education, China Agricultural University, Beijing 100083, China
e-mail: zhaozhangcau@cau.edu.cn

Key Lab of Agriculture Information Acquisition Technology, Ministry of Agriculture of China, China Agricultural University, Beijing 100083, China

C. Igathinathane · P. Flores · J. Mathew · A. K. Das
Department of Agricultural and Biosystems Engineering, North Dakota State University, Fargo, ND 58102, USA

J. Ransom
Department of Plant Sciences, North Dakota State University, Fargo, ND 58108, USA

Y. Ampatzidis
Agricultural and Biological Engineering Department, Southwest Florida Research and Education Center, University of Florida, IFAS, 2685 SR 29 North, Immokalee, FL 34142, USA

Z. Zhang et al. (eds.), *Unmanned Aerial Systems in Precision Agriculture*,
Smart Agriculture 2, https://doi.org/10.1007/978-981-19-2027-1_5

coupled with color and textural features and SVM classifier, is a useful approach for wheat lodging ratio detection. This study demonstrates the application of automatic plot extraction with low-resolution images produced by higher UAV mission height for plot scale (1.5 m × 3.6 to 14.6 m) studies such as wheat lodging forms a critical piece of information that could be adopted by users related to UAV applications and image analyses.

Keywords Wheat lodging ratio · Machine leaning · Deep learning · Mission height · UAV

5.1 Introduction

Wheat (*Triticum aestivum L.*) is an essential staple crop worldwide, which serves as a major source of starch, energy, protein, vitamins, dietary fiber, and phytochemicals [1]. There are a lot of factors limiting the yield of wheat, and lodging ranks among the top. Setter et al. [2] reported that lodging would lower the photosynthesis rate by 60–80% relative to non-lodged crops, which would significantly reduce the yield. In addition to deterioration in grain quality, yield losses exacerbate because the combine harvester could not or have difficulties to pull the lodged crops into the combine header, due to which much of the crops are left in the field [3, 4]. Accurate and timely information on wheat lodging plays an important role for breeders in cultivating/selecting resistant varieties, agronomists and plant physiologists in studying the reasons for lodging (e.g., too much nitrogen), and farmers and crop insurance personal in processing the insurance coverage [5, 6].

Though there is significant application progress of sensing and automation technologies in agriculture [6–11] inspection of crop lodging is still pursued by conventional field- and vision-based manual methods [5, 6, 12, 13], which are time-consuming, error-prone and unreliable [14]. Furthermore, under unfavorable weather conditions (e.g., heavy rain) or when the crops are tall (e.g., maize), it is infeasible for raters to get into the field for timely assessment [15]. Moreover, raters may generate different results (intra-rater inconsistency), and this has been reported to cause compensation disputes between insurance companies and wheat growers [16]. Therefore, there is a need for a new objective, quick, unbiased, and reliable approach for wheat lodging detection.

Researchers started to explore remote sensing techniques on wheat lodging detection in the past and tested satellite images on wheat and canola lodging detection [15, 17–20]. Though the satellite images can cover large areas, there are a number of limitations, including, but not limited to, low resolution images (tens of centimeters or meters) and coarse temporal resolution (several days for revisiting the same location). Very recently, with the rapid progress of unmanned aerial vehicles (UAVs) and new machine learning (ML) and deep learning (DL) algorithms, researchers started to take advantage of UAV images coupled with new algorithms for crop lodging detection [21, 22]. Compared to the satellite images, UAV images have much higher

pixel resolution (millimeter or centimeter level), and the images can be collected as long as the weather cooperates (not windy or rainy). Thus, the temporal resolution is finer than that of the images from satellites. The application of UAV images on wheat lodging detection is at a nascent stage, but recent results have already shown some promising results. Li et al. [23] took advantage of UAV visible image for sugar-beet lodging detection, with an accuracy of over 90%, and [24] achieved accuracies of 93% and 96% for canola and wheat lodging monitoring, respectively. Almost all these studies treated the lodging as a binary issue—lodging or non-lodging. However, some researchers are more interested in lodging ratio (percentage of the lodged area of the plot) of a certain plot, especially for breeders and growers. Few studies have been traced to specifically focus on the plot lodging ratio detection.

While modeling lodging detection using images, the first step is to create a dataset for lodging and non-lodging plots or areas. For a majority of the current studies, the mainstream approach is to manually crop the images for the dataset creation [5, 25]. The manual cropping approach is inefficient, inaccurate, and prone-to-error. The inefficiency comes from the need to crop one plot and then save the region of interest (ROI) as a new image. Considering breeders may cultivate hundreds to thousands of crop plots, it would be time-consuming. The inaccuracy is because some parts of the plots may be missed due to fatigue/carelessness, and the error may be caused by cropped images including noises (e.g., soil). Hence, it is desirable to develop a semi-automatic or even an automatic approach for image dataset creation.

Since crop lodging detection is a categorical classification problem, researchers usually extract features from the collected images, which would further be fed into ML algorithms. The proper selection of features that could represent the crop characteristics play a critical role in obtaining higher detection accuracy, and the feature selection or determination requires domain knowledge. Different researchers have demonstrated that color and textural features performed satisfactorily on crop lodging detection [25]. With the advent of DL, the manual feature selection could be replaced by deep conventional neural networks, which is free of domain knowledge and completed automatically. A number of DL models combine the automatic feature extraction and neural network to make the whole process (feature extraction and classification) fully automatic. However, only a few studies have compared the wheat lodging detection accuracies between DL and ML.

For a majority of current studies on wheat lodging detection, the mission height is empirically determined. For a high mission altitude (e.g., 100 m above ground level), the data collection takes less time, and the resolution of collected images is coarser; and for a low mission altitude (e.g., 15 m above ground level), the data collection requires more time, and the image had a finer resolution and also required more storage space. The empirical approach may have a good performance, but it is more desirable to conduct specific studies to explore and quantify the height effects on wheat lodging ratio detection.

To address the issues mentioned above, the objectives of this study were to: (1) develop an automatic approach for wheat plot dataset generation; (2) explore mission height effects on wheat lodging ratio detection; and (3) compare the performance of ML and DL models on wheat lodging ratio detection.

5.2 Materials and Methods

Different procedures in this study of developing a methodology for automatic dataset generation, comparing DL and ML models on wheat lodging detection, and exploring the mission height effects are outlined in Fig. 5.1. After lodging occurred, field missions of three different heights were completed, followed by immediate field visual evaluation of lodging conditions in terms of non-, light, and severe lodging. The collected images were first preliminarily processed to generate orthomosaic maps, followed by an automatic approach in generating individual plots as the dataset. Then, different ML and DL models were tested on plot images of different heights, with performance compared. All the detailed research process is described subsequently in appropriate sections.

5.2.1 Experimental Field and Data Collection

The experimental field used in this study was cultivated on May, 2020 near Thompson, ND, U.S., as shown in Fig. 2. The experimental area is about 64 × 100 m (210 × 330 ft.), with two sizes of plots—short: 1.5 × 3.6 m (5 × 12 ft) and long: 1.5 × 14.6 m (5 × 48 ft.). Among the total experimental 428 plots (short 312 and long 116), there are 28 plots that served as borders (columns 1, 11, 20, 29, and 55 in the right photo of Fig. 5.2) are eliminated to avoid the border effect, while the other 400 are considered for analysis in this study.

Approximately a week after the lodging occurred, drone flights at three heights were conducted on July 23, 2020: 15 m (50 ft), 45 m (150 ft), and 91 m (300 ft). A DJI Phantom 4D RTK UAV (DJI-Innovations, Inc., ShenZhen, China) was used for data collection, which is outfitted with a 20 megapixel (5472 × 3648 pixel) color

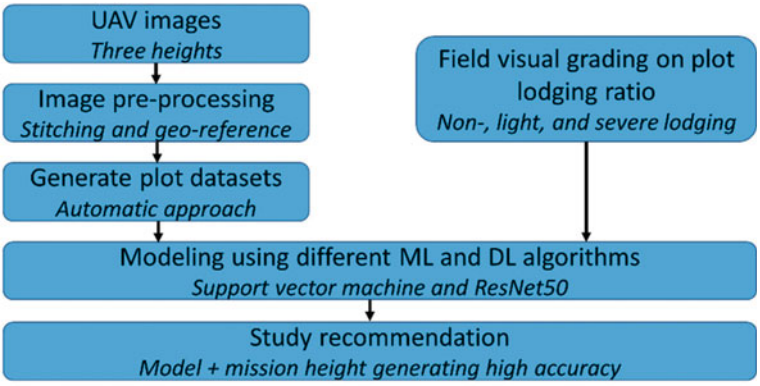

Fig. 5.1 Overall procedure flowchart of wheat lodging ratio detection on different unmanned aerial vehicle (UAV) mission heights based on machine learning (ML) and deep learning (DL) models

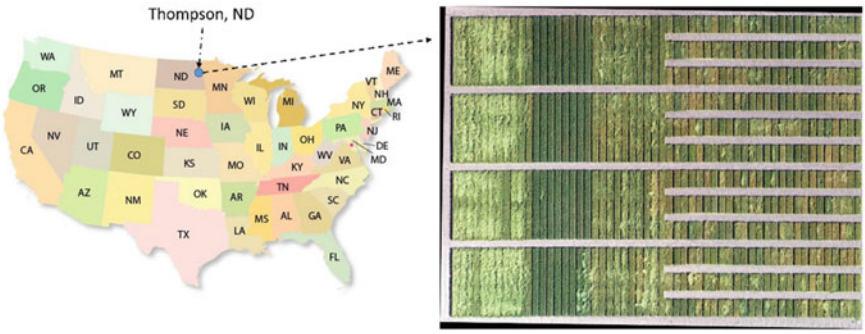

Fig. 5.2 Plot location and layouts. There are two sized plots—short (312): 1.5 × 3.6 m (5 × 12 ft.) and long (116): 1.5 × 14.6 m (5 × 48 ft.). On the right photo, starting from left to right, columns 1, 11, 20, 29, and 55 are border plots, which are not used in this study

camera. The mission speed was set to 2.5 m/s, and since the weather was sunny during the entire data collection time window, the balance mode was set as sunny. Additionally, both side and forward overlaps for image capture were set as 80%.

Immediately after all the three flights, two raters visited the field for manual evaluation. The two raters were trained by experts before the field experiments, and they graded each plot in terms of lodging ratio (percentage of the lodged area of the plot) evaluated as three grades as non-, light, and severe lodging. The lodging ratio grades are represented as non-lodging—lodging does not occur, light lodging –<45% area is lodged, and severe lodging –>45% is lodged. The two raters inspected independently and separately to avoid the rating results affected by each other. These manual evaluation results were used as labels while training and testing models.

5.2.2 Data Pre-Processing and Dataset Generation

For each mission height, the collected images were pre-processed using Pixel4D (Pix4D V4.3.33, S.A., Prilly, Switzerland) to generate an orthomosaic map (right photo in Fig. 5.2). Then, for each height, an orthomosaic map was generated. The three individual maps were geo-referred with ground control points, which were installed in the field before the experiment.

After obtaining the three individual and geo-referred orthomosaic maps, the next step was to generate the individual plot images automatically. To segment the individual plots from the background, it requires to determine individual plot's coordinates. A huge number of parameters have been used to segment crops from noisy infield backgrounds [26], and excess green (E × G, Eq. 5.1) have been selected in this study for its satisfactory performance in preliminary tests. After calculating the E × G for the individual pixel of the original image (Fig. 5.3i), the monochrome E × G image is obtained and shown in Fig. 5.3ii. After applying a threshold (0.01 used

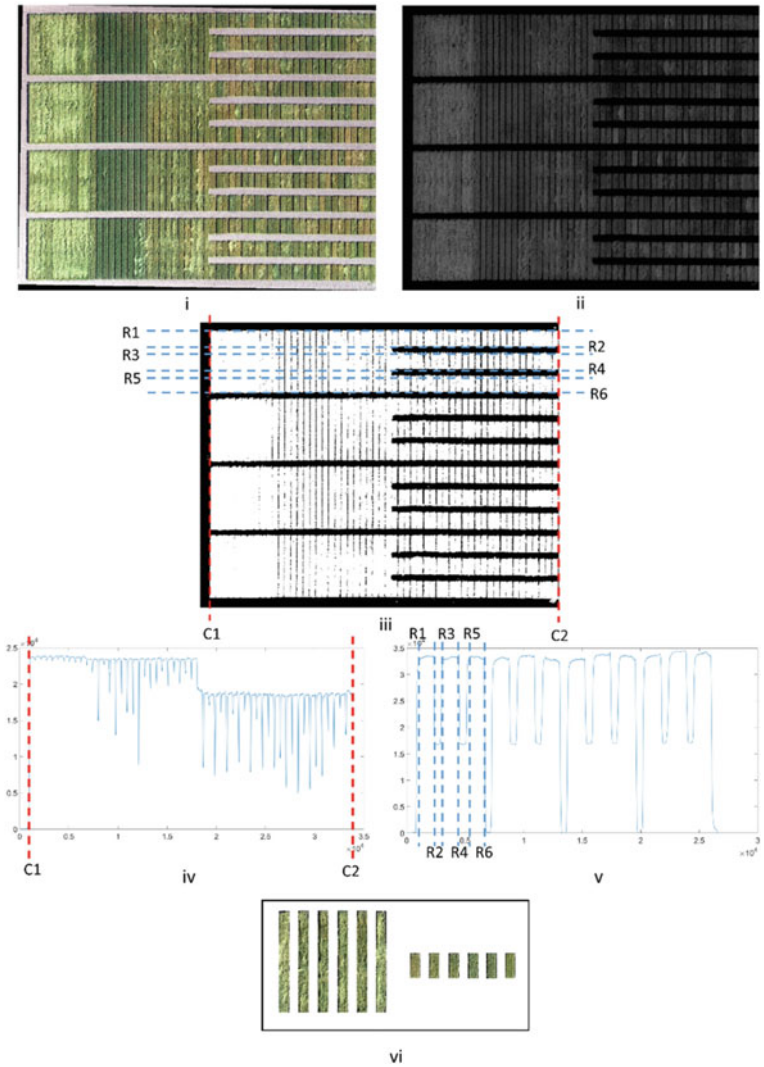

Fig. 5.3 Flowchart for dataset generation. (i) Original image; (ii) monochrome of excess green; (iii) binary image after thresholding (0.01) excess green image (ii); (iv) relationship between x coordinates (horizontal direction) and sum of each column; (v) relationship between y coordinates (vertical direction) and the sum of each row; and (vi) samples of automatically generated extracted images of the individual plots

in this study), a binary image is generated (Fig. 5.3iii), with white and black pixels representing 1 and 0, respectively.

$$\text{Excess Green} = 2 \times \text{Green (G)} - \text{Red(R)} - \text{Blue(B)} \tag{5.1}$$

The experimental field consists of 4 sub-plots (Fig. 5.3i) in the vertical direction. Since the four plots are very similar and the methodology used for any of the 4 sub-plots can be used/duplicated for others, we use the top sub-plot to explain the new methodology for automatic individual plot image dataset generation. For each subplot, the key information in the vertical direction is the top and bottom coordinates for both large the small plots. For the large plots, the top coordinates are denoted as R1 and the bottom as R6 (Fig. 5.3iii); for the small plots, the top and bottom coordinates are R1 and R2 (or R3 and R4 or R5 and R6), respectively. Compared to the vertical direction coordinates, the horizontal direction coordinates are relatively easy to obtain since all the plots are of the same width and the plots number in the horizontal direction is pre-known. Then, the problem of obtaining the horizontal coordinates is converted to a problem of finding the left edge (C1 in Fig. 5.3iii) and right edge (C2 in Fig. 5.3iii).

Based on the binary image (Fig. 5.3iii), for each column, the sum of pixel values is calculated, which is actually the number of white pixels (white pixel is equal to 1; black pixel is equal to 0). The relation between the image x coordinates (horizontal direction) and their corresponding sum of the individual column is shown in Fig. 5.3iv. Due to a sudden change from 0 to a very high value, the C1 value could be obtained, and the C2 value is actually the right edge of the image. Similarly, the relationship between the row coordinate (vertical direction) and each row's sum is presented in Fig. 5.3 v, with R1-6 values calculated automatically. After detecting each plot's coordinates, these coordinates were used to crop the original images automatically to generate the individual plot dataset. Sample images automatically generated are shown in Fig. 5.3vi.

Among the total 428 cropped plots, the 28 border plots were manually removed and the remaining 400 cropped plot image were considered as the dataset for further processing.

5.2.3 Machine Learning Algorithm

Traditional ML algorithms need to feed features into the model for training. Features are the properties that can represent the characteristics of a plot. Based on literature review and accumulated research experience, color (Table 5.1 #1–12) and texture (Table 5.1 #13) features are chosen. The color features are chosen as lodged crop plots would have soil and stems shown in the images, which may be less green from the normal crop growing area. For the texture features, the lodged crops may be not as uniform as non-lodged crops.

Table 5.1 Features selected based on domain knowledge for wheat lodging ratio detection

Feature number	Feature	Description
1	R	Red channel
2	G	Green channel
3	B	Blue Channel
4	H	Hue Channel
5	S	Saturation channel
6	I	Intensity channel
7	L	Luminosity channel
8	a	a channel
9	b	b channel
10	NDI	Normalized difference index
11	E × G	Excess green index
12	E × R	Excess red index
13	GLCM	Texture feature

Features 1–9 are all normalized; detailed information of these features can be referred to [26]

After these features are extracted, the next step is to choose a suitable classifier. There are a number of classifiers that have been used to address classification issues in agriculture, such as support vector machine (SVM), neural network, random forest [26–28]. In this study, based on our preliminary test and literature review [29–31], the SVM classifier was selected.

5.2.4 Deep Learning

Compared to the manual feature selection of the ML, DL would extract features automatically. During the past decades, DL has made the feature extraction automatic by using convolutional neural networks. A number of studies have validated Resnet50 to be a good performing model in addressing classification problems in agriculture [27], and this model was selected.

In this study, data processing was completed using Matlab® 2020b (The Mathworks, Inc., Natick, Mass., USA), including feature extraction and selection, and running ML and DL models. The desktop used for this study was configured with Windows 10 OS, Intel(R) Core(TM) i7-8700 CPU, 32 GB RAM, Intel(R) UHD Graphics 630, and 16 G GPU memory. For all the modeling processes, randomly selected 70% of the dataset was used for data training, and the other 30% for testing.

5.3 Results and Discussion

5.3.1 Machine Learning Classification Results

For the ML approach, the SVM classifier model was used (randomly selected data 70% training and the other 30% testing). Since the training dataset (70%) was randomly assigned for each run, the SVM model was run for 10 times, with the averaged detection accuracy shown in Fig. 5.4. The detection accuracy is not significantly different (Tukey; $p > 0.05$) from each other at different heights. Actually, the accuracy of 15 m altitude is 66.8%, which is a little lower than that of 46 m for 67.8% and 91 m for 67.7%. The image pixel resolutions of the 15 m, 46 m, and 91 m are 0.4, 1.2, and 2.5 cm/pixel, respectively, indicating that images with 2.5 cm/pixel resolution performing similarly to images with 0.4 cm/pixel. The reason for this observation is perhaps the analysis ROI is large and is about the plot scale (1.5 × 3.6 m and 1.5 × 14.6 m), and high-resolution image images are generally required at plant scale analysis. To collect high-resolution images, it requires more time for data collection, larger data size (increase storage) than the low-resolution ones, and requires higher computational resources and cost. Thus, in the future, researchers can use 2.5 cm/pixel image resolution (low-resolution), instead of 0.4 cm/pixel resolution (high-resolution) images for wheat lodging detection.

5.3.2 Deep Learning Results

Wheat lodging detection accuracy based on Resnet50 DL model is shown in Fig. 5.5. Since the DL model ran many iterations, and in each iteration using randomly selected data (70% training and the other 30% testing, there is no need to run the

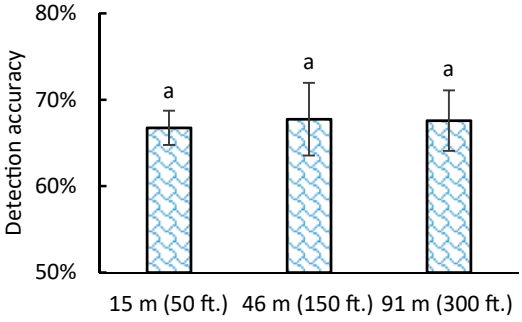

Fig. 5.4 Detection accuracy based on color and textural features coupled with support vector machine classifier on images of different height. Bars with the same letters are non-significantly different by Tukey's test at 0.05 significance level

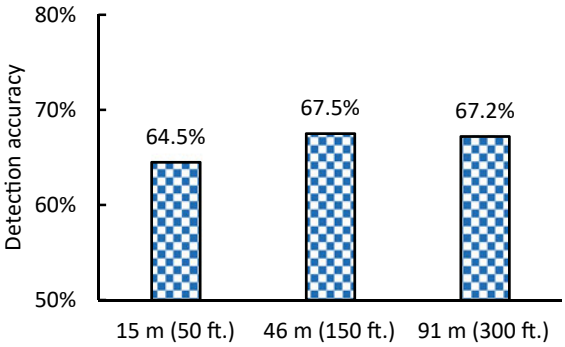

Fig. 5.5 Detection accuracy based on Resnet50 deep learning model on different mission heights

models multiple times. The detection accuracy of 64.5% on 15 m (image resolution 0.4 cm/pixel) above ground level is a little lower than that of 67.5% on 46 m (1.2 cm/pixel) and 67.2% on 91 m (2.5 cm/pixel). Generally, the detection accuracy pattern using Resnet50 is similar to using SVM—the higher mission height would actually increase the detection accuracy slightly.

5.3.3 Comparison of ML and DL

The detection accuracy comparison between ML (SVM) and DL (Resnet50) is shown in Table 5.2. It is obvious that SVM and Resnet50 results are of similar accuracies for the mission heights of 46 m and 91 m; while for the 15 m mission height, the SVM results a little higher accuracy over Resnet50. Since using high altitude mission would generate high detection accuracy, and simultaneously reduce the computation cost, it is recommended to use SVM with 91 m mission height for wheat lodging detection.

5.4 Conclusion

This study has tested the performance of the machine learning model (support vector machine - SVM) and deep learning model (Resnet50) on wheat lodging ratio detection at three different heights. A majority of studies followed the manual approach

Table 5.2 Detection accuracy comparison between support vector machine and Resnet50

	15 m (50 ft.)	46 m (150 ft.)	91 m (300 ft.)
Support vector machine	66.8%	67.8%	67.6%
Resnet50	64.5%	67.5%	67.2%

to generate the field plot dataset (individual plot images) from experimental field, and this method is time-consuming, inefficient, and inaccurate. This study developed a new approach for automatic field plot dataset generation, which is based on image pre-processing using excess green. This new and automatic dataset generation approach has been applied and validated in this study, and can be applied to a similar workflow. For both support vector machine and Resnet50 models, the detection accuracies (64.5–67.8%) are not significantly different for three different mission heights (15, 46, and 91 m) that had the corresponding 0.4, 1.2, and 2.5 cm/pixel image resolutions. Therefore, it is recommended to use 2.5 cm/pixel resolution, instead of the 0.4 and 1.2 cm/pixel resolutions, for wheat lodging ratio detection, which can collect and process data more efficiently while not lowering detection accuracies. Regarding the support vector machine and Resnet50, the SVM is recommended (coupled with color and texture features) to be used for wheat lodging detection for its high accuracy. This study has demonstrated that using low-resolution images (2.5 cm/pixel) coupled with SVM is an efficient approach for wheat lodging ratio detection, with an accuracy of 67%.

Acknowledgements Authors thanks Jensen Kenton for preliminary data processing of the UAV images, including stitching them together using Pixle4D and geo-referring the images using ArcGIS10. Additionally, the authors would thank Singh Shreya and Gurram Vikranth Reddy for field data collection, and Eisinger Darin and Chad Deplazes for preparing the experimental fields. This work was jointly supported by North Dakota Agricultural Experiment Station (NDAES) Precision Agriculture Graduate Research Assistantship and USDA Agricultural Research Service Project No. 6064-21660-001-32S. Project accession No. 435589.

References

1. Shewry PR, Hey SJ (2015) The contribution of wheat to human diet and health. Food Energy Secur 4(3):178–202. https://doi.org/10.1002/fes3.64
2. Setter TL, Laureles EV, Mazaredo AM (1997) Lodging reduces yield of rice by self-shading and reductions in canopy photosynthesis. Field Crops Res. 49(2–3):95–106. https://doi.org/10.1016/s0378-4290(96)01058-1
3. Islam MS, Peng S, Visperas RM, Ereful N, Bhuiya MSU, Julfiquar AW (2007) Lodging-related morphological traits of hybrid rice in a tropical irrigated ecosystem. Field Crops Res 101(2):240–248. https://doi.org/10.1016/j.fcr.2006.12.002
4. Pinthus MJ (1974) Lodging in wheat, barley, and oats: the phenomenon, its causes, and preventive measures. Adv Agron 25:209–263. https://doi.org/10.1016/s0065-2113(08)60782-8
5. Zhang Z, Flores P, Igathinathane C, L Naik D, Kiran R, Ransom JK (2020a) Wheat lodging detection from UAS imagery using machine learning algorithms. Remote Sens 12(11):1838.https://doi.org/10.3390/rs12111838
6. Zhang Z, Igathinathane C, Li J, Cen H, Lu Y, Flores P (2020b) Technology progress in mechanical harvest of fresh market apples. Comput Electron Agric 175:105606. https://doi.org/10.1016/j.compag.2020.105606
7. Zhang Z, Heinemann PH, Liu J, Baugher TA, Schupp JR (2016) The development of mechanical apple harvesting technology: a review. Trans ASABE 59(5):1165–1180. https://doi.org/10.13031/trans.59.11737

8. Zhang Z, Pothula A, Lu R (2019) Improvements and evaluation of an infield bin filler for apple bruising and distributions. Trans ASABE 62(2):271–280. https://doi.org/10.13031/aim.201800921
9. Lu R, Pothula AK, Mizushima A, VanDyke M, Zhang Z (2018) System for sorting fruit. U.S. Patent No. 9,919,345
10. Lu R, Zhang Z, Pothula AK (2017) Innovative technology for enhancing apple harvest and postharvest handling efficiency. Fruit Qtly 25(2):11–14
11. Yao L, Hu D, Zhao C, Yang Z, Zhang Z (2021) Wireless positioning and path tracking for a mobile platform in greenhouse. Int J Agric Biol Eng 14(1):216–223. https://doi.org/10.25165/j.ijabe.20211401.5627
12. Fischer RA, Stapper M (1987) Lodging effects on high-yielding crops of irrigated semidwarf wheat. Field Crops Res 17(3–4):245–258. https://doi.org/10.1016/0378-4290(87)90038-4
13. Piñera-Chavez FJ, Berry PM, Foulkes MJ, Jesson MA, Reynolds MP (2016) Avoiding lodging in irrigated spring wheat. I. Stem and root structural requirements. Field Crops Res 196:325–336. https://doi.org/10.1016/j.fcr.2016.06.009
14. Bock CH, Poole GH, Parker PE, Gottwald TR (2010) Plant disease severity estimated visually, by digital photography and image analysis, and by hyperspectral imaging. Crit Rev Plant Sci 29(2):59–107. https://doi.org/10.1080/07352681003617285
15. Chauhan S, Darvishzadeh R, Boschetti M, Pepe M, Nelson A (2019) Remote sensing-based crop lodging assessment: Current status and perspectives. ISPRS J Photogramm Remote Sens 151:124–140. https://doi.org/10.1016/j.isprsjprs.2019.03.005
16. Yang MD, Huang KS, Kuo YH, Tsai HP, Lin LM (2017) Spatial and spectral hybrid image classification for rice lodging assessment through UAV imagery. Remote Sens 9(6):583. https://doi.org/10.3390/rs9060583
17. Chauhan S, Darvishzadeh R, Lu Y, Boschetti M, Nelson A (2020) Understanding wheat lodging using multi-temporal Sentinel-1 and Sentinel-2 data. Remote Sens Environ 243:111804. https://doi.org/10.1016/j.rse.2020.111804
18. Vargas JQ, Khot LR, Peters RT, Chandel AK, Molaei B (2019) Low orbiting satellite and small UAS-based high-resolution imagery data to quantify crop lodging: a case study in irrigated spearmint. IEEE Geosci Remote Sens Lett 17(5):755–759. https://doi.org/10.1109/lgrs.2019.2935830
19. Yang H, Chen E, Li Z, Zhao C, Yang G, Pignatti S, …, Zhao L (2015) Wheat lodging monitoring using polarimetric index from RADARSAT-2 data. Int J Appl Earth Obs Geoinf 34:157–166https://doi.org/10.1016/j.jag.2014.08.010
20. Zhao L, Yang J, Li P, Shi L, Zhang L (2017) Characterizing lodging damage in wheat and canola using Radarsat-2 polarimetric SAR data. Remote Sens Lett 8(7):667–675. https://doi.org/10.1080/2150704x.2017.1312028
21. Chu T, Starek MJ, Brewer MJ, Murray SC, Pruter LS (2017) Assessing lodging severity over an experimental maize (Zea mays L.) field using UAS images. Remote Sens 9(9):923. https://doi.org/10.3390/rs9090923
22. Zhao B, Li J, Baenziger PS, Belamkar V, Ge Y, Zhang J, Shi Y (2020) Automatic wheat lodging detection and mapping in aerial imagery to support high-throughput phenotyping and in-season crop management. Agron 10(11):1762. https://doi.org/10.3390/agronomy10111762
23. Li X, Li X, Liu W, Wei B, Xu X (2021) A UAV-based framework for crop lodging assessment. Eur J Agron 123:126201. https://doi.org/10.1016/j.eja.2020.126201
24. Rajapaksa S, Eramian M, Duddu H, Wang M, Shirtliffe S, Ryu S, …, Parkin I (2018) Classification of crop lodging with gray level co-occurrence matrix. In: 2018 IEEE Winter Conference on Applications of Computer Vision (WACV). IEEE, pp 251–258. https://doi.org/10.1109/wacv.2018.00034
25. Mardanisamani S, Maleki F, Hosseinzadeh Kassani S, Rajapaksa S, Duddu H, Wang M, ... , Eramian M (2019) Crop lodging prediction from UAV-acquired images of wheat and canola using a DCNN augmented with handcrafted texture features. In: Proceedings of the IEEE/CVF conference on computer vision and pattern recognition workshops.https://doi.org/10.1109/cvprw.2019.00322

26. Flores P, Zhang Z, Igathinathane C, Jithin M, Naik D, Stenger J, …, Kiran R (2021) Distinguishing seedling volunteer corn from soybean through greenhouse color, color-infrared, and fused images using machine and deep learning. Ind Crops Prod 161:113223.https://doi.org/10.1016/j.indcrop.2020.113223
27. Flores P, Zhang Z, Jithin M, Jahan N, Stenger J (2020) Distinguishing volunteer corn from soybean at seedling stage using images and machine learning. Smart Agric. https://doi.org/10.12133/j.smartag.2020.2.3.202007-SA002
28. Zhang J, Wan L, Igathinathane C, Zhang Z, Guo Y, Sun D, Cen H (2021) Spatiotemporal heterogeneity of chlorophyll content and fluorescence response within rice (Oryza sativa L.) canopies under different nitrogen treatments. Front Plant Sci 12:499. https://doi.org/10.3389/fpls.2021.645977
29. Costa L, Ampatzidis Y, Rohla C, Maness N, Cheary B, Zhang L (2021) Measuring pecan nut growth utilizing machine vision and deep learning for the better understanding of the fruit growth curve. Comput Electron Agric 181:105964. https://doi.org/10.1016/j.compag.2020.105964
30. Costa L, Archer L, Ampatzidis Y, Casteluci L, Caurin GAP, Albrecht U (2020) Determining leaf stomatal properties in citrus trees utilizing machine vision and artificial intelligence. Precis Agric 1–13. https://doi.org/10.1007/s11119-020-09771-x
31. Jahan N, Flores P, Liu Z, Friskop A, Mathew JJ, Zhang Z (2020) Detecting and distinguishing wheat diseases using image processing and machine learning algorithms. In: 2020 ASABE annual international virtual meeting. American Society of Agricultural and Biological Engineers, p 1. https://doi.org/10.13031/aim.202000372

Chapter 6
Wheat-Net: An Automatic Dense Wheat Spike Segmentation Method Based on an Optimized Hybrid Task Cascade Model

JiaJing Zhang, An Min, Brian J. Steffenson, Wenhao Su, Cory D. Hirsch, James Anderson, Ce Yang, and Jian Wei

Abstract Precise segmentation of wheat spikes from a complex background is necessary for obtaining image-based phenotypic information of wheat traits such as yield estimation and disease evaluation. A new instance segmentation method based on a Hybrid Task Cascade model was trained and validated to improve previous attempts of wheat spike detection. In this study, wheat images were collected from fields where the environment varied both spatially and temporally. Res2Net50 was adopted as a backbone network, combined with multi-scale training, deformable convolutional networks, and Generic ROI Extractor for rich feature learning. The proposed methods were trained and validated, and the average precision (AP) obtained for the bounding box and mask was 0.904 and 0.907, respectively, and the accuracy for wheat spike counting was 99.29%. Comprehensive empirical analyses revealed that our method (Wheat-Net) performed well on challenging field-based datasets with mixed qualities, particularly those with various backgrounds and

J. Zhang
College of Information and Electronics Engineering, Institute of Automation at Chinese Academy of Science, China Agricultural University, Beijing 100083, China

A. Min · C. Yang (✉)
Department of Bioproducts and Biosystems Engineering, University of Minnesota, Saint Paul, MN 55108, USA
e-mail: ceyang@umn.edu

B. J. Steffenson · C. D. Hirsch
Department of Plant Pathology, University of Minnesota, Saint Paul, MN 55108, USA

W. Su
College of Engineering, Department of Bioproducts and Biosystems Engineering, China Agricultural University, University of Minnesota, Saint Paul, MN 55108, USA

J. Anderson
Department of Agronomy and Plant Genetics, University of Minnesota, Saint Paul, MN 55108, USA

J. Wei
College of Information and Electronics Engineering, China Agricultural University, Beijing 100083, China

Z. Zhang et al. (eds.), *Unmanned Aerial Systems in Precision Agriculture*,
Smart Agriculture 2, https://doi.org/10.1007/978-981-19-2027-1_6

wheat spike adjacence/occlusion. These results provide evidence for dense wheat spike detection capabilities using the latest date deep learning algorithms, which can be useful for improving wheat breeding and disease screening efforts.

Keywords Hybrid task cascade model · Challenging dataset · Non-structural field · Wheat spike detection · Instance segmentation

6.1 Introduction

Wheat is the most widely cultivated cereal crop and also one of the most important food sources for humans in the world. The spike is the most important component of the wheat plant because it contains the seeds that are harvested and ultimately consumed. Thus, the spike is an essential component for studies focusing on yield estimation, morphology assessments, and disease detection (e.g. Fusarium head blight). With respect to FHB assessment in wheat, conventional scoring methods rely on visual estimations, which are costly, laborious, error-prone, and time-consuming. Therefore, developing an automated method to increase detection of spikes and the percentage of florets infected within each spike is important to reduce labor costs and increase efficiency and accuracy. In-field automated wheat spike detection based on remote sensing is an important step toward the detection of diseases infecting this part of the wheat plant.

Deep learning (DL) with strong feature learning abilities has spawned a multitude of applications in computer vision. It encodes the composition of lower-level features into more discriminative higher-level features [1]. DL can solve more complex problems with higher precision and has been successfully used in disease and pest detection [2–4], plant classification [5–7], yield prediction [8–10], and growth monitoring [11, 12]. Thus, DL, with its advantages of high precision and intelligence, is an attractive alternative to conventional wheat spike detection methods.

Recently, DL has been shown to perform well in a wide variety of wheat spike detection studies. Some previous works involving wheat detection have been conducted under laboratory conditions and controlled environments [13–16]. Laboratory based experiments have good lighting conditions and a clean background, which is not the case for field-based research, which is more complicated and yields images where the background usually contains a lot of disturbances (including soil and weeds). The complicated background greatly increases the difficulty of resolving individual wheat spikes, but represents the actual growing environment of wheat. Thus models developed from the field are more realistic of real-world conditions for wheat cultivation. Several in-field spike detection and counting studies have been conducted [17–21]. However, the detection results from these studies were based on bounding boxes, which are insufficient for discriminating diseased florets on the spikes, where precise pixel areas are required for segmentation. Some researchers have used semantic segmentation algorithms to segment wheat spikes in the field with a simpler environment by controlling some factors in the experiment. For example,

in implementing a Fully Convolutional Network (FCN) segmentation model of individual wheat spikes, [22] positioned spikes to avoid occlusion–an intervention which does not simulate the actual growing conditions of wheat in the field. Alkhudaydi et al. [23] employed FCN to segment multiple wheat spikes, which achieved a Mean Accuracy (MA) of classification of >76%. However, their model performed poorly under challenging conditions caused by variable lighting and weather. Tan et al. [24] performed simple linear iterative clustering (SLIC) for superpixel segmentation of digital wheat images, which resulted in a high accuracy (94.01%) under high nitrogen fertilizer level and a lower accuracy (80.8%) under no nitrogen fertilizer application. Ma et al. [25] developed EarSegNet to segment multiple wheat spikes from canopy images captured under field conditions and realized a precision of 79.41%. However, semantic segmentation algorithms cannot segment wheat spikes out individually when they are obstructed by other spikes, leaves or stems, which is a common situation o under field conditions.

Instance segmentation can effectively segment partially obstructed wheat spikes. This method localizes objects of interest in an image at the pixel-level, which achieves both object detection and semantic segmentation [26, 27]. With instance segmentation, the segmented objects are generally represented by masks and a bounding box (bbox); however, few studies have been advanced using instance segmentation for detecting individual plant organs under field settings. Qiu et al. [28] used a Mask RCNN model to reliably detect wheat spikes (mean average precision is 0.9201) with different shapes and features in the field. However, to achieve these results, they used a background plate to block complex backgrounds and also a shade shed to provide even lighting, which reduced the complexities of image capture and subsequent annotation. They also divided the original image into many smaller images, which resulted in image distortion. This, in turn, resulted in images with only partial objects or no objects at all, which would destroy the integrity of the wheat spikes.

In summary, most of the current methods of wheat spike detection focus on spike detection or semantic segmentation in the laboratory, which may not be suitable for phenotyping diseased spikes under complex field environment. Therefore, it is necessary to explore a more applicable and efficient approach for segmenting wheat spikes under field conditions. In this study, a new instance segmentation model (called Wheat-Net) based on a multi-task Hybrid Task Cascade (HTC) model [26] was used to segment individual wheat spikes in high densities in the field. The HTC model has a powerful cascade structure that enhanced performance on various tasks. It solved the problem of insufficient information flow between mask branches at different stages in Cascade Mask R-CNN, which is a direct combination of Cascade R-CNN [29] and Mask R-CNN [30]. The HTC model effectively integrated cascade into instance segmentation by interweaving detection and segmentation for joint multi-stage processing, achieving outstanding performance on COCO (Common Objects in COntext) test-dev and test-challenge [31]. In this paper, the HTC model achieved excellent performance on a challenging dataset with various complex backgrounds and a high level of obstruction. In a complex, unstructured environment, our method not only accurately detected the wheat spikes with bounding boxes, but also extracted spike regions from the background at the pixel level.

The subsequent parts of this paper are organized as follows: Sect. 6.2 describes the dataset and presents the adopted approach, Sect. 6.3 indicates the experimental results, Sect. 6.4 discusses the performance of our method, and Sect. 6.5 gives conclusions and suggestions for future research.

6.2 Materials and Methods

6.2.1 Data Collection

Wheat genotypes were sown in field plots on the St. Paul campus of the University of Minnesota (UMN) in 2019. These genotypes included mostly breeding lines from the UMN hard red spring wheat breeding program, which can vary for different spike morphology traits such as color, shape types as well as spike density. Images of spikes from many wheat genotypes were collected from 11 July 2019 (late flowering stage) to 2 August 2019 (milk stage). In the complex field environment, we used an autofocus single-lens reflex (SLR) camera (Canon EOS Rebel T7i) to collect image data under ambient weather conditions. During image collection, the weather was mostly clear with few clouds and the winds very light; therefore, image distortion due to weather conditions was kept at a minimum. The wheat images (effective pixels: 6000 $\times$ 4000) collected had complex backgrounds, including weeds, soil, blurred wheat, blue sky, and white clouds. To increase the diversity of the image set, we used different shooting angles, focal lengths, and camera to object distances. Wheat is typically a dense crop and the images collected contained as many as 124 spikes per image. In addition, it was common that portions of images had insufficient illumination (blue box with zoom-in shown in Fig. 6.1b). Moreover, the above factors also resulted in many problems such as spike adjacence (Red box with zoom-in shown in Fig. 6.1c), occlusion, variation in spike size, and partial spikes on the image edge (Yellow box with zoom-in shown in Fig. 6.1d). The spike occlusion problem was the most serious problem and included various scenarios such as spikes over spikes (Fig. 6.2a), leaves over spikes (Fig. 6.2b), stems over spikes (Fig. 6.2c), and awns over spikes (Fig. 6.2d). Although the above factors greatly increase the segmentation difficulty in spike detection, they encompass the true field environment and are helpful to improve the robustness of the spike segmentation model.

The artificial image annotation software, Labelme [32], was used to label the ground truth for wheat spikes using polygons (Fig. 6.3). To obtain high-quality annotated datasets, dense points along the outside edge of every spike were selected to form an accurate spike region. These annotated images were used to calculate the loss and optimized the model parameters during model training. The training set (524 images including 12,591 spikes) and the testing set (166 images including 4,749 spikes) were divided according to commonly used ratios in deep learning modeling.

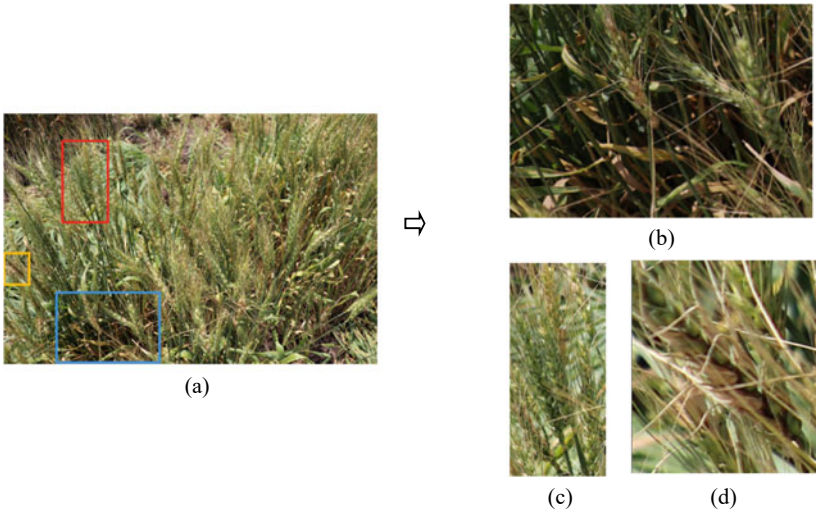

Fig. 6.1 **a** An example of an original image of a wheat plot indicating sections (blue, red and yellow boxes) enlarged to show **b** an area with incomplete illumination, **c** adjacent spikes in close proximity, and **d** partial spikes on the edge of the images

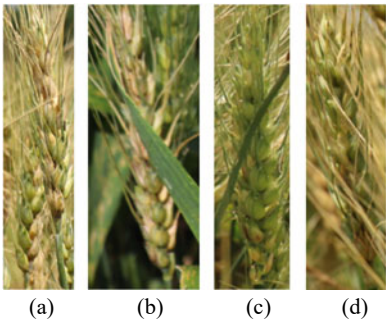

Fig. 6.2 Examples of various spike occlusion scenarios: **a** spike over spike, **b** leaf over spike, **c** stem over spike, and **d** awns over spike

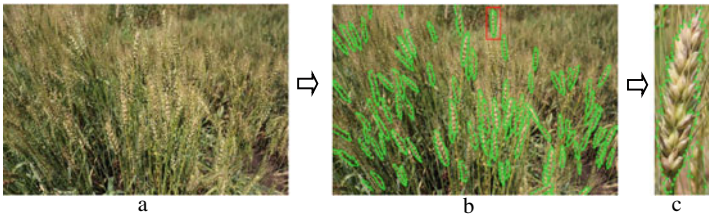

Fig. 6.3 Annotation of wheat spikes: **a** the original image of a wheat plot, **b** the image with annotated wheat spikes, and **c** details of a single annotated spike

6.2.2 Methods of Wheat Instance Segmentation

6.2.2.1 Architecture of Wheat-Net

In this study, instance segmentation was the key protocol implemented to reliably detect and segment wheat spikes in a complex non-structural environment. We built the wheat spike instance segmentation model, Wheat-Net, for our high-complexity dataset based on the HTC model [26], which is a novel cascade architecture for instance segmentation. We cascaded three Mask R-CNN networks to build the HTC architectures (Fig. 6.4). The advantages of this model can be ascribed to three key aspects. (1) It interleaved the box and mask branches (the green lines in Fig. 6.4) based on Cascade Mask R-CNN. This improvement allowed the mask branch to take advantage of the updated bbox. (2) It made full use of the mask feature of the preceding stage by adding a direct information flow between mask branches (the blue lines in Fig. 6.4). This design further improved the accuracy of mask detection. (3) It explored more contextual information by adding a semantic segmentation branch (the red lines in Fig. 6.4). The above optimizations are combined for better predictions, which effectively improved the utilization of information and enhanced performance.

$$r_t = B_t\left(x_t^{box}\right), \tag{6.1}$$

$$x_t^{box} = p(x, r_{t-1}) + p(S(x), r_{t-1}), \tag{6.2}$$

$$x_t^{mask} = p(x, r_t) + p(S(x), r_t,) \tag{6.3}$$

$$m_t = M_t(\mathcal{F}\left(x_t^{mask}, m_{t-1}^{-}\right),) \tag{6.4}$$

$$\mathcal{F}\left(x_t^{mask}, m_{t-1}^{-}\right) = x_t^{mask} + g_t(m_{t-1}^{-}) \tag{6.5}$$

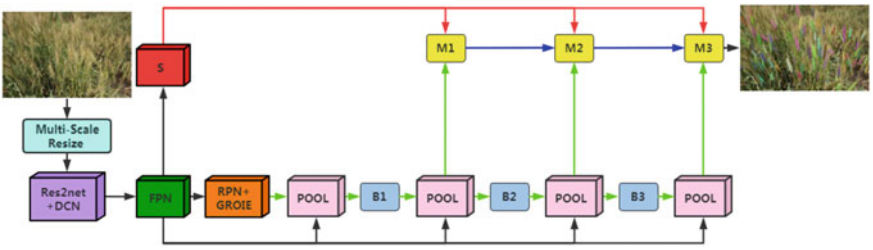

Fig. 6.4 The architectures of Wheat-Net. "POOL" region-wise feature extraction, "B" bounding box, and "M" mask. 'S' is semantic segmentation branch

where x is the feature of backbone network, x_t^{box} and x_t^{mask} denote box and mask features of x and the input Region of Interest (RoI). S indicates the semantic segmentation head. The box and mask heads of each stage take the RoI features extracted from the backbone as input. $p(\cdot)$ is a pooling operator, B_t and M_t indicate the box and mask head at the t-th stage.r_t and m_t represent predictions of box and mask, respectively. m_{t-1}^{-} indicates the intermediate feature of M_{t-1}. $\mathcal{F}$ is a function that combines the features of the current stage and the preceding one. g_t denotes a 1×1 convolutional layer.

6.2.2.2 Optimization of Wheat-Net

Different backbones have an important effect on the performance of the model because of their differences in feature extraction ability. Res2Net50 (Fig. 6.5b) [33] represents multi-scale features at a granular level and increases the range of receptive fields for each network layer, which is different from the concurrent bottleneck structure shown in Fig. 6.5a, such as ResNet [34]. Specifically, it replaces the 3×3 filters of n channels with a set of smaller filter groups, which are connected in a hierarchical residual-like style to increase the number of scales that the output features can represent. It can capture more details and global features without increasing calculations. ResNeXt is an improved model of ResNet, (Fig. 6.5c) [35] and is constructed by repeating a building block and the transformations to be aggregated, all of the same topology. It is a simple, homogeneous and multi-branch architecture, which can extend to any large number of transformations without specialized designs. In the experimental part of this paper, we compare the performance of above-mentioned backbones in our dataset.

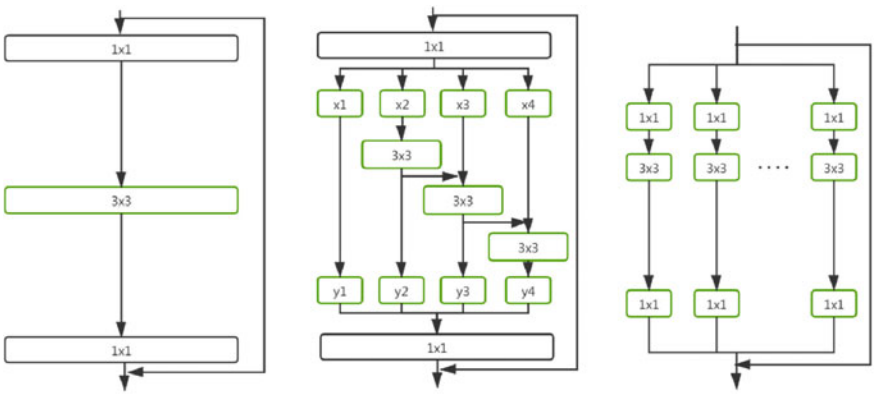

(a) A block of ResNet (b) A block of Res2Net (c) A block of ResNeXt

Fig. 6.5 Comparison between different backbones for Wheat-Net

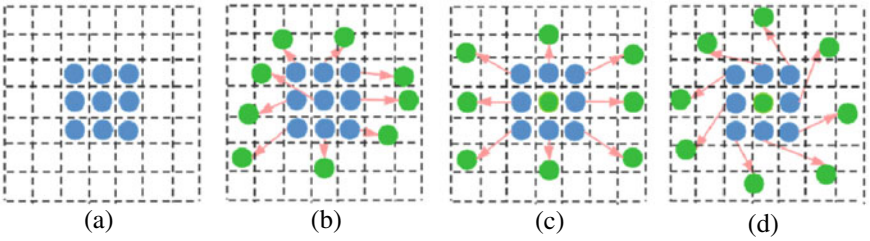

Fig. 6.6 Different calculation positions under: **a** standard convolution (blue points); **b** deformable convolution (with green points). **c** and **d** are special cases of (**b**), showing that the deformable convolution generalizes scale and rotation transformations

Deformable convolutional networks (DCN) [36] were integrated into our model because they provide a solution to model dense spatial transformations and are effective for sophisticated vision tasks. DCN allowed free deformation of the sampling grid as shown in Fig. 6.6, which added offsets learned from target tasks to the regular sampling grid of standard convolution without additional supervision.

In our model, feature pyramid networks (FPN) [30] extracted RoI features from different levels of the feature pyramid by using a top-down architecture. These different features, generated and fused by FPN, comprised the inputs of the Region Proposal Network (RPN) [37]. RPN predicted object bounds and objectness scores to efficiently generate region proposals with a wide range of scales and aspect ratios. Generic RoI Extractor (GRoIE) [38] was used to extract the RoI. Since all layers of FPN retain useful information, they introduce non-local building blocks and attention mechanisms to overcome the limitations of existing RoI extractors, which select only one (the best) layer from FPN. They also can be integrated seamlessly with the two-stage architectures for instance segmentation tasks for superior performance compared to traditional RoI extractors [39]. In addition, we used multi-task learning [40] to achieve both target detection and semantic segmentation of wheat spikes. Multi-task learning combined all tasks into a single model: that is, what is learned for each task can help other tasks be learned better. Hence, Multi-task learning can improve learning efficiency and prediction accuracy by learning multiple objectives from a shared representation.

As an important part of the object detection pipeline, non-maximum suppression (NMS) could sort the detection bbox based on their scores [41], select the detection bbox with the highest score and suppress all other bbox that had significant overlap (using a pre-defined threshold) with it. However, NMS might lose the objects that are within the predefined overlap threshold. Bodla et al. [42] proposed a Soft-NMS algorithm to prevent objects from being eliminated. It decayed the detection scores of all other objects as a continuous function of their overlap. In the experimental part of this paper, we conducted a comparative experiment between NMS and Soft-NMS.

The size of the input image had a significant impact on model performance. Moreover, the feature map generated by the network was much smaller than the original image, which caused the loss of small object features. Because we collected

images with various shooting distances and angles, the dataset contained many small spikes. They were difficult to detect and affected the performance of the model. Multi-scale training [43], which defines several fixed scales in advance and randomly selects a scale for training in each epoch, can effectively improve this limitation. Therefore, we used images of multiple scales for training to improve the robustness and accuracy of the model. Due to memory constraints, the short-side of the input images was randomly selected from 416 to 1184, and the another side's size was calculated according to the aspect ratio of the original image's size.

Learning rate (LR) was one of the most important hyperparameters in training. If the LR is large at the beginning of training, the model may become unstable, making it difficult to reach the optimal solution. To address this, we used warm-up LR [34] to improve the training situation. Warm-up LR allows the LR to gradually increase from a small value in the first few epochs until the initial LR is reached. In this way, the model can gradually stabilize, and the convergence speed becomes faster after stabilization.

As an important hyperparameter in deep learning, LR could determine whether and when the model can converge. A large LR will make the model fluctuate greatly, and it is difficult to reach the optimal solution. In addition, as the number of iterations increases, the LR will continue to decay to reduce fluctuations of model. We chose two popular LR decay methods and compared them in the experimental chapter: one was MultiStepLR, which used the dynamic step to update the LR, and the other was CosineAnnealingLR, which decayed the LR periodically based on the cosine function. Hyperparameters of the model were adjusted and optimized based on multiple experiments. Finally, the initial LR was set to 0.0025 and adjusted every 20 epochs with a decay factor of 0.5. The other hyperparameters of the model are shown in Table 6.1.

Eventually, a new wheat spike segmentation method based on the HTC model combined with the backbone of Res2Net50, deformable convolutional networks, and Generic RoI Extractor was constructed (Fig. 6.4). During the model training, each image was flipped horizontally to augment the data and the Res2Net-50 backbone was pre-trained based on the ImageNet dataset [44] using transfer learning, which was suitable for solving the problem of a small training dataset.

Table 6.1 Hyperparameter values which optimized through training

Parameter	Value
Optimization algorithm	SGD
Momentum	0.9
Initial learning rate	0.0025
Warmup_iterations	500
Warmup_ratio	0.001
Warmup_ratio	0.001
Optimal Epoch	38
Batch size	1

The overall loss function takes the form of multi-task learning and was defined as function (6).

$$\mathrm{L} = \sum_{t=1}^{T} a_t \left(L_{bbox}^t + L_{mask}^t \right) + \beta L_{seg} \tag{6.6}$$

where L_{bbox}^t is the loss of the bounding box predictions at stage t. L_{mask}^t is the loss of mask prediction at stage t. L_{seg} is the semantic segmentation loss in the form of cross-entropy. Because we cascade 3 Mask R-CNN networks to build the HTC architectures, T was set to 3. In addition, to balance the contributions of different stages and tasks, we set $\alpha = [1, 0.5, 0.25]$ and $\beta = 1$ by default [26].

6.2.3 Evaluation Metric

The performance of Wheat-Net was evaluated by average precision (AP), which is the area under the curve of precision-recall (PR). A high AP value indicates that a model has both high precision and high recall. AP stood out as the most-used metric due to its representativeness and simplicity. AP was calculated by using the method of the COCO dataset, which interpolated through all points. The evaluation metrics are defined as follows:

$$Precision = \frac{TP}{TP + FP} \tag{6.7}$$

$$Recall = \frac{TP}{TP + FN} \tag{6.8}$$

$$p_{interp}(r_{n+1}) = \max_{\tilde{r}:\tilde{r} \geq r_{n+1}} p(\tilde{r}) \tag{6.9}$$

$$\mathrm{AP} = \sum_{n=0} (r_{n+1} - r_n) p_{interp}(r_{n+1}) \tag{6.10}$$

$$IoU(A, B) = \left| \frac{A \bigcap B}{A \bigcup B} \right| \tag{6.11}$$

where TP indicates the correct detection, FP is the wrong detection, and FN represents the ground truth not detected. $p(\tilde{r})$ is the measured precision at recall $\widetilde{r}$. IOU is the intersection over union between two bboxes. A represents the bbox labeled manually and B represents the bbox generated based on Wheat-Net. In this research, we evaluated the performance of Wheat-Net based on the IOU threshold of 0.5, which is commonly used for instance segmentation model.

6.3 Results

The data analysis was performed with the deep learning development framework of PyTorch. An Intel (R) Core (TM) i7-6700 processor, a 16 GB random-access memory card and a graphic card (NVIDIA GeForce GTX1080Ti 11GB) were used for the modeling process.

In order to determine the appropriateness of the model, a test set of 166 images was used to assess the model. The AP of bbox and mask reached 0.904 and 0.907, respectively. In the case of dense wheat spike detection from complex backgrounds, false positives tended to happen more often than false negatives. Therefore, we used the PR curve (Fig. 6.7), which emphasized the evaluation of the prediction model on positive examples to evaluate the performance of the model. This step confirmed the effectiveness of Wheat-Net for detecting wheat spikes in the complex field environment.

In addition, we visualized the detection results of the complex image shown in Fig. 6.8a. As shown in Fig. 6.8, in the non-structural field, the model showed outstanding performance for complex backgrounds, dense spikes, adjacence and occlusion (Fig. 6.8b), insufficient illumination (Fig. 6.8d), and incomplete spikes on the edge of images (Fig. 6.8c).

The model can effectively solve the problem of various occlusion scenarios, which is one of the most challenging areas in the field of object detection. Figure 6.9 demonstrated the detection results of various occlusion scenarios including: when a spike is obstructed by another spike; when a spike is occluded by a leaf; when a spike

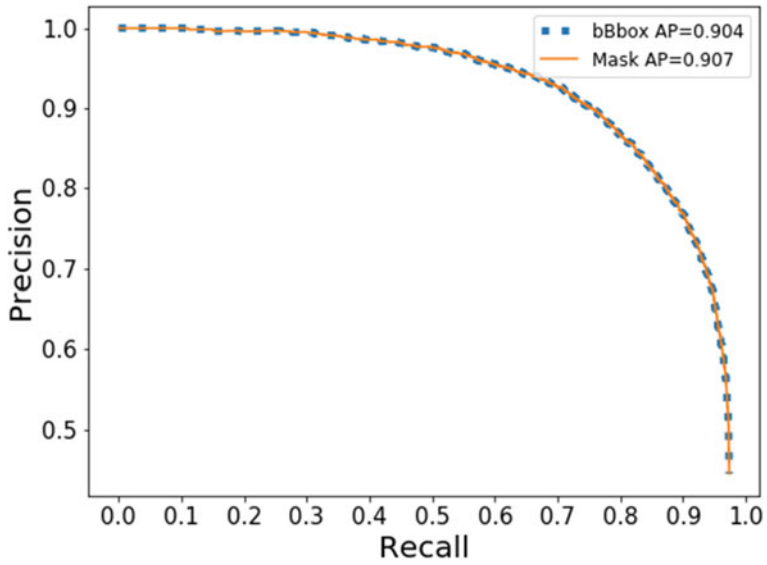

Fig. 6.7 The curve of precision and recall

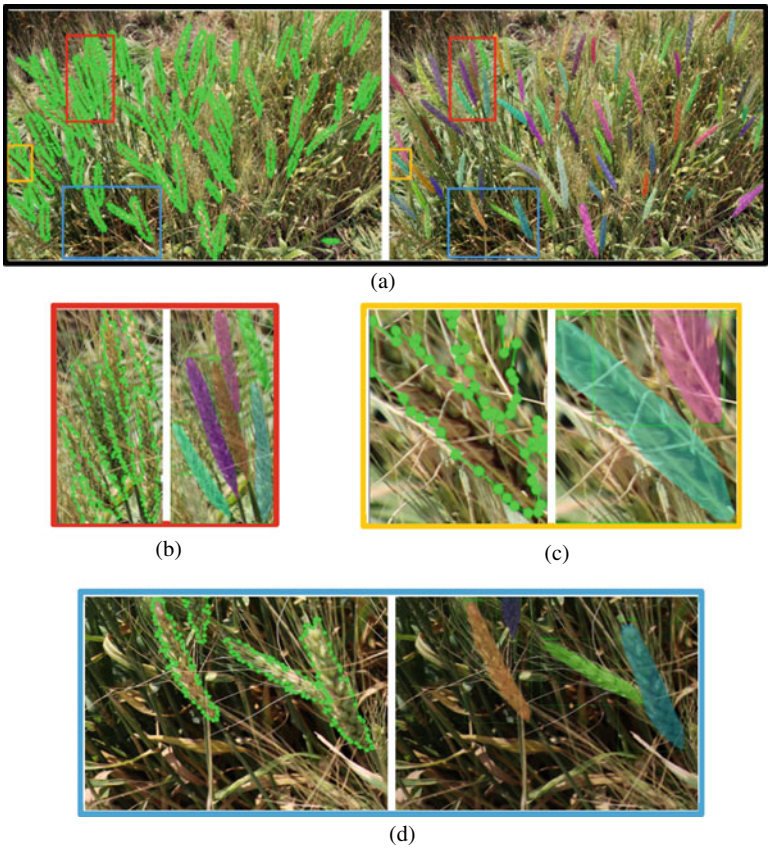

Fig. 6.8 Annotation images versus detection results. **a** Overall detection results, **b** detail 1—area of adjacence and occlusion, **c** detail 2—area of incomplete spikes in image, **d** detail 3—area of insufficient illumination of spikes

is occluded by a stem; and when a spike is occluded by awns from another spike. Comparing the total number of spikes (4,933) detected by the model with the actual number of spikes manually labeled (4,899), the accuracy of the wheat spike counting was 99.29%. This demonstrates that Wheat-Net was effective for automatic wheat spike counting under complex field conditions.

6.3.1 Comparative Evaluation

In order to evaluate the performance of the HTC model, we conducted a comparative experiment with other CNNs. The test results (Table 6.2) show that the box AP and mask AP of the HTC model are better than Mask RCNN and Cascade Mask RCNN.

Fig. 6.9 Detection results of various occlusions. **a** one spike (under purple mask) is occluded by another spike, **b** one spike (under red mask) is occluded by a wheat leaf, **c** one spike is occluded by a wheat stem, **d** One spike (under orange mask) is occluded by awns from another spike

Table 6.2 Comparison of the performances of HTC model versus other models

Model	AP (IOU = 0.5)		AP (IOU = 0.75)		Epoch	Train time (h)	Test time (s)
	Bbox	Mask	Bbox	Mask			
HTC	0.904	0.907	0.790	0.747	38	16	2560
Mask RCNN	0.884	0.884	0.755	0.690	60	10	3186
Cascade Mask RCNN	0.899	0.900	0.785	0.754	40	14	2673

In addition, although the train time of the HTC model was slightly longer than the other two models, the HTC model was more satisfactory in terms of test time and converged in the lowest number of epochs, which also proved the effectiveness of the HTC structure. Therefore, considering accuracy and speed, we decided to use the HTC model to detect wheat spikes.

To make full use of the advantages of the HTC model to achieve better performance, we conducted experiments to select the backbone to build the HTC model. As shown in Table 6.3, we selected ResNet, ResNeXt, and Res2Net for comparative

Table 6.3 Comparison of the performance of different Res2Net backbones

Backbone	AP (IOU = 0.5)		AP (IOU = 0.75)		Epoch	Train time/h	Test time/s
	Bbox	Mask	Bbox	Mask			
ResNet50	0.894	0.897	0.761	0.693	60	17	2393
ResNet101	0.871	0.876	0.696	0.632	20	7	3302
ResNeXt50	0.893	0.897	0.788	0.733	66	18	2299
ResNeXt101	0.872	0.875	0.706	0.624	40	14	2251
Res2Net50	**0.904**	**0.907**	**0.790**	**0.747**	38	16	2560

Table 6.4 The segmentation results using the HTC model based on suppression algorithms: NMS and Soft-NMS

Type	AP (IOU = 0.5)		AP (IOU = 0.75)		epoch	Train time/h	Test time/s
	Bbox	Mask	Bbox	Mask			
NMS	**0.904**	**0.907**	0.790	0.747	38	16	**2560**
Soft-NMS	0.903	0.906	**0.795**	**0.750**	38	16	3385

Table 6.5 The results based on MultiStepLR and CosineAnnealingLR

Type	AP (IOU = 0.5)		AP (IOU = 0.75)		epoch	Train time/h	Test time/s
	Bbox	Mask	Bbox	Mask			
CosineAnnealingLR	0.891	0.895	0.786	0.753	70	18	3134
MultiStepLR	**0.904**	**0.907**	**0.790**	0.747	**38**	**16**	**2560**

experiments. By comparing the results of ResNet50 and ResNet101 (or ResNeXt50 and ResNeXt101), we found that increasing the depth of the backbone could not improve the performance of wheat detection. The test results (Table 6.3) showed that Res2Net50 and ResNeXt50 have more outstanding performance than other backbone networks. Furthermore, ResNeXt50 required a shorter test time, while Res2Net50 had higher AP values. Both of the two networks can be used as the backbone of the model based on different criteria.

We also conducted a comparative experiment between NMS and Soft-NMS. As shown in Table 6.4, the HTC model with NMS achieved a higher AP with IOU = 0.5 within a much shorter test time compared to Soft-NMS. Therefore, although Soft-NMS could help the HTC model to achieve slightly higher AP with IOU = 0.75, we chose to use NMS based on the best balance between precision and speed.

The decay of LR is extremely important to make the model more stable. Therefore, we conducted a comparative experiment between MultiStepLR and CosineAnnealingLR to select the suitable LR decay method for Wheat-Net. From Table 6.5, we can see that the MultiStepLR was superior to CosineAnnealingLR in terms of AP. In addition, MultiStepLR required a shorter test time than CosineAnnealingLR. Therefore, MultiStepLR was better than CosineAnnealingLR for our model, and we therefore chose MultiStepLR to decay the learning rate.

6.3.2 Ablation Study

Ablation study is an effective way to see how a method affects performance of the entire model by removing that specific method from the model. To perform this analysis, we used multi-scale training, DCN, and GRoIE methods to improve the performance of the model. To more accurately evaluate the effect of each method, we

Table 6.6 The results of ablation study regarding the combination of Multi-scale, DCN and GRoIE

Multi-scale	DCN	GRoIE	AP(IOU = 0.5)		AP(IOU = 0.75)		Epoch	Train time/h	Test time/s
			Bbox	Mask	Bbox	Mask			
–	–	–	0.868	0.872	0.722	0.677	20	7.5	2988
√	–	–	0.891	0.899	0.772	0.745	40	14	4775
√	√	–	0.897	0.904	**0.794**	**0.768**	40	14	4791
√	√	√	**0.904**	**0.907**	0.790	0.747	38	16	**2560 s**

conducted the ablation study experiments with the HTC model based on Res2net50 (LR = 0.0025, batch size = 1, image scale = 2100*1184) and compared the performances on the test set.

The experimental results (Table 6.6) showed that multi-scale training, DCN, and GRoIE had various effects on the performance of Wheat-Net. Specifically, the AP (both IOU = 0.5 and IOU = 0.75) were significantly improved by multi-scale training, although it increased some test times. The improvement of DCN for IOU = 0.75 was greater than that for IOU = 0.5, which showed that DCN had a more significant effect on a large IOU threshold. In addition, GRoIE increased AP with IOU = 0.5 and decreased AP with IOU = 0.75. The experimental results showed that GRoIE did not work for our dataset when using a larger threshold of IOU.

6.4 Discussion

6.4.1 Analysis of Experimental Error

Although Wheat-Net showed excellent performance for wheat segmentation in the complex environment, there were still errors, which we subsequently analyzed. As shown in Fig. 6.10a, the model had some segmentation errors at the bottom of the wheat spikes. The sparse florets at the bottom of the spike led to some differences between the texture characteristics of the bottom and other parts. This in turn caused inaccurate segmentation for the bottom of the spikes.

Due to the complexity of our dataset, the problem of adjacence and occlusion of wheat was very common in most images. Segmentation of adjacent objects was one of the most challenging tasks in the field of crop phenotyping. From Fig. 6.10b, we can see that the two spikes were adhesive and the lower one was occluded by a wheat stem. Our method achieved a good segmentation result in such a complex situation, but there were still errors at the junction. The color, texture, and shape of the adherent spikes were very similar, which made the dividing line unclear. As a result, this made the positive objects at the junction annotated as negative, which increased the number of False Negatives (FN) and reduced Recall. When only multi-scale training was used (DCN and GROIE are not used), the AP value with IOU of

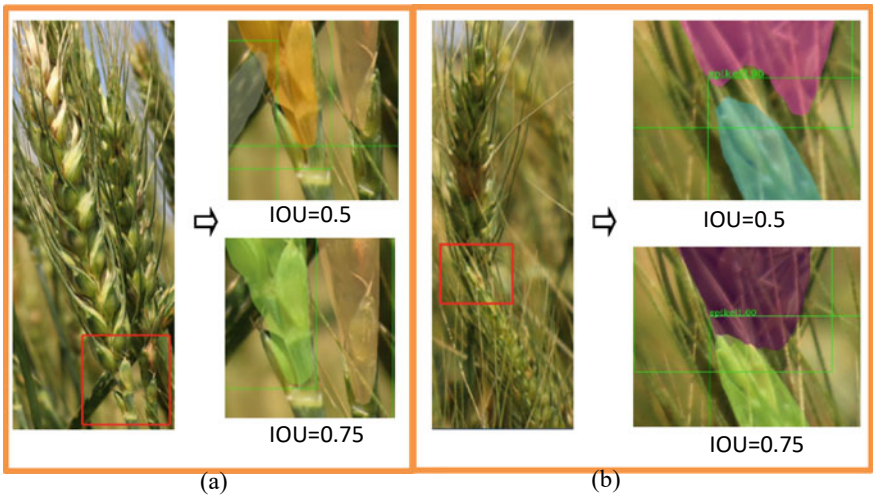

Fig. 6.10 The Demonstration of experimental error. **a** The error of spike bottom. **b** The error at the junction of different spikes

0.75 was the highest (Table 6.6). We chose this model for visual testing (shown in Fig. 6.10) and found that it could greatly reduce the above-mentioned experimental errors (including the bottom and junction errors) compared to when IOU = 0.5. Regardless of the ability to detect wheat spikes, it achieved a better performance for accurately segmenting the wheat spike.

6.4.2 Evaluation of Wheat-Net on Barley Spike Detection

The phenotypic characteristics of wheat and barley are quite different in both the shape and size of the kernel and the length of awn. In order to verify the generalized applicability of the model, we constructed a test set containing 29 barley images to test the detection ability of the model to barley spikes. The experimental results showed that the AP of bbox and mask for barley detection achieved 0.799 and 0.812, respectively. From Fig. 6.11, we can see that the model achieved acceptable visualization results for barley, especially for the detection of adjacence and occlusion (red boxes in Fig. 6.11). Thus, our model has the potential to segment barley spikes as well demonstrating strong robustness to a variety of spike shapes and colors. However, due to the similar phenotypic characteristics of adhesive spikes, there were still errors at the junction of spikes. In addition, similar to the errors encountered with wheat spike detection, there were also some errors at the top and bottom of barley spikes. It is expected that the performance of segmenting barley spikes will be improved by

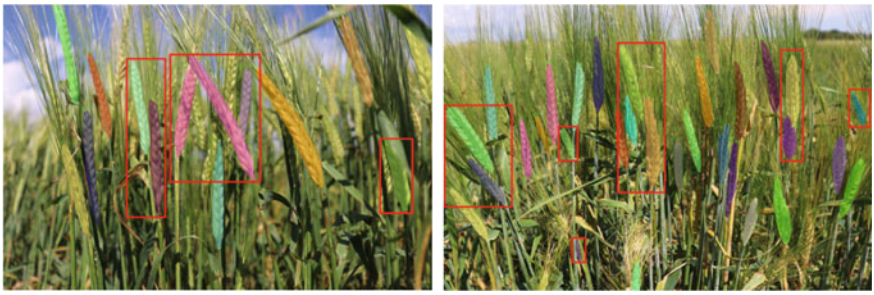

Fig. 6.11 The visualization results of barley detection

retraining our model using a barley training dataset. This study also established the protocol of a pre-training model for the detection of other inflorescences of small grain cereal crops such as the panicles of oat and rice.

6.5 Conclusion

Development of an automatic and accurate wheat spike segmentation protocol can improve wheat yield estimation, disease evaluation (especially to Fusarium head blight). A wheat spike image set was collected from unstructured fields where the environment varied spatially and temporally, and accurate labels were created for use in the training and testing of a wheat spike detection and segmentation model. To realize wheat spike detection and segmentation in dense and complex, non-structural field environments, an effective HTC-based method was evaluated, which overcame the difficulties of complex backgrounds, serious occlusion, and incomplete spikes on the edge in dense wheat instance segmentation. The proposed method used the HTC model with a hybrid cascade structure to make full use of rich mask and box information. With Res2Net50 as the backbone network, multi-scale training was used to learn features of different scales, and deformable convolutional networks (DCN) and Generic RoI Extractor (GRoIE) were trained to improve model accuracy. Eventually, high-accuracy automatic wheat spike detection and segmentation were achieved. An AP of 0.904 and 0.907 was found for bbox and mask, respectively, based on the optimized HTC model. Our method was particularly effective for the detection of wheat spikes with frequent adjacence, overlapping, occlusion, and other complex growth states. The accuracy rate for wheat spike counting was 99.29%. Comprehensive empirical analyses revealed that the proposed method achieved excellent performance and outperformed in a non-structural environment. Therefore, our method has important reference significance and value for improving the efficiency of wheat breeding for improved yield and also disease resistance, particularly to Fusarium head blight [45]. For future research, we intend to further improve the segmentation ability for the junctions between spikes. Additionally, the improvement of modeling

speed will also be considered. We expect that our proposed method will be expanded to the broader agricultural research area, including detection of the seed-bearing inflorescences of other crops.

Acknowledgements This work was supported by the USDA-ARS United States Wheat and Barley Scab Initiative (grant numbers 58-5062-8-018), the Lieberman-Okinow Endowment at the University of Minnesota, and the State of Minnesota Small Grains Initiative.

References

1. Ni C, Wang D, Vinson R, Holmes M, Tao Y (2019) Automatic inspection machine for maize kernels based on deep convo-lutional neural networks. Biosys Eng 178:131–144. https://doi.org/10.1016/j.biosystemseng.2018.11.010
2. Da Silva LA, Bressan PO, Gonçalves DN, Freitas DM, Machado BB, Gonçalves Wesley N (2019) Estimating soybean leaf defoliation using convolutional neural networks and synthetic images. Comput Electron Agric 156:360–368. https://doi.org/10.1016/j.compag.2018.11.040
3. Desai SV, Balasubramanian VN, Fukatsu T, Ninomiya S, Guo W (2019) Automatic estimation of heading date of paddy rice using deep learning. Plant Methods 15(1):76. https://doi.org/10.1186/s13007-019-0457-1
4. Senthilkumar T, Jayas DS, White NDG, Fields PG, Gräfenhan T (2017) Detection of ochratoxin A contamination in stored wheat using nearinfrared hyperspectral imaging. Infrared Phys Techn 81:228–235. https://doi.org/10.1016/j.infred.2017.01.015
5. Aich S, Josuttes A, Ovsyannikov I, Strueby K, Ahmed I, Duddu HS, Pozniak C, Shirtliffe S, Stavness I (2018) DeepWheat: estimating phenotypic traits from crop images with deep learning. In: 2018 18th IEEE winter conference on applications of computer vision (WACV), pp 323–332. https://doi.org/10.1109/wacv.2018.00042
6. Momeny M, Jahanbakhshi A, Jafarnezhad K, Zhang YD (2020) Accurate classification of cherry fruit using deep cnn based on hybrid pooling approach. Postharvest Biol Technol 166:111204. https://doi.org/10.1016/j.postharvbio.2020.111204
7. Suresh G, Gnanaprakash V, Santhiya R (2019) Performance analysis of different CNN architecture with different optimisers for plant disease classification. In: 2019 5th international conference on advanced computing and communication systems (ICACCS), Coimbatore, India. 916–921. https://doi.org/10.1109/ICACCS.2019.8728282
8. Khaki S, Wang L, Archontoulis SV (2020) A cnn-rnn framework for crop yield prediction. Front Plant Sci. https://doi.org/10.3389/fpls.2019.01750
9. Sun J, Di L, Sun Z, Shen Y, Lai Z (2019) County-level soybean yield prediction using deep cnn-lstm model. Sensors 19(20):4363. https://doi.org/10.3390/s19204363
10. Yang Q, Shi L, Lin L (2019) Plot-scale rice grain yield estimation using UAV-based remotely sensed images via CNN with time-invariant deep features decomposition. In: IGARSS 2019–2019 IEEE international geoscience and remote sensing symposium, Yokohama, Japan, 7180–7183. https://doi.org/10.1109/IGARSS.2019.8898061
11. Luna RG de, Dadios EP, Bandala AA, Vicerra RRP (2020) J Agric Sci 42:24–36. https://doi.org/10.17503/agrivita.v42i1.2499
12. Zhuang S, Wang P, Jiang B, Li M (2020) Learned features of leaf phenotype to monitor maize water status in the fields. Comput Electron Agric 172. https://doi.org/10.1016/j.compag.2020.105347
13. Kovalchuk N, Laga H, Cai J, Kumar P, Parent B, Lu Z et al (2017) Phenotyping of plants in competitive but controlled environments: a study of drought response in transgenic wheat. Funct Plant Biol 44(3):290. https://doi.org/10.1071/FP16202

14. Misra T, Arora A, Marwaha S, Chinnusamy V, Goel S (2020) Spikesegnet-a deep learning approach utilizing encoder-decoder network with hourglass for spike segmentation and counting in wheat plant from visual imaging. Plant Methods. https://doi.org/10.1186/s13007-020-00582-9
15. Qiongyan L, Cai J, Berger B, Okamoto M, Miklavcic SJ (2017) Detecting spikes of wheat plants using neural networks with laws texture energy. Plant Methods 13(1):83. https://doi.org/10.1186/s13007-017-0231-1
16. Pound MP, Atkinson JA, Wells DM, Pridmore TP, French AP (2017) Deep learning for multi-task plant phenotyping. In: 2017 IEEE international conference on computer vision workshops (ICCVW). IEEE
17. Chandra AL, Desai SV, Balasubramanian VN, Ninomiya S, Guo W (2020) Active learning with point supervision for cost-effective panicle detection in cereal crops. Plant Methods 16(1). https://doi.org/10.1186/s13007-020-00575-8
18. David E, Madec S, Sadeghi-Tehran P, Aasen H, Zheng B, Liu S et al (2020) Global wheat head detection (gwhd) dataset: a large and diverse dataset of high resolution rgb labelled images to develop and benchmark wheat head detection methods. Plant Phenomics. https://doi.org/10.34133/2020/3521852
19. Hasan MM, Chopin JP, Laga H, Miklavcic SJ (2018) Detection and analysis of wheat spikes using convolutional neural networks. Plant Methods 14(1):100. https://doi.org/10.1186/s13007-018-0366-8
20. Sadeghi-Tehran P, Virlet N, Ampe EM, Reyns P, Hawkesford MJ (2019) Deepcount: in-feld automatic quantifcation of wheat spikes using simple linear iterative clustering and deep convolutional neural networks. Front Plant Sci 10:1176. https://doi.org/10.3389/fpls.2019.01176
21. Xu X, Li H, Yin F, Xi L, Ma X (2020) Wheat ear counting using k-means clustering segmentation and convolutional neural network. Plant Methods 16(1). https://doi.org/10.1186/s13007-020-00648-8
22. Zhang D, Wang D, Gu C, Jin N, Liang D (2019) Using neural network to identify the severity of wheat fusarium head blight in the field environment. Remote Sens 11(20):2375. https://doi.org/10.1016/10.3390/rs11202375
23. Alkhudaydi T, Reynolds D, Griffiths S, Zhou J, Iglesia BDL (2019) An exploration of deep-learning based phenotypic analysis to detect spike regions in field conditions for uk bread wheat. Plant Phenomics (1, article no. 45):1–17. https://doi.org/10.34133/2019/7368761
24. Tan C, Zhang P, Zhang Y, Zhou X, Wang Z, Du Y, Mao W, Li W, Wang D, Guo W (2020) Rapid recognition of field-grown wheat spikes based on a Superpixel segmentation algorithm using digital images. Front Plant Sci 11:259. https://doi.org/10.3389/fpls.2020.00259
25. Ma J, Li Y, Liu H, Du K, Zhang L (2020) Improving segmentation accuracy for ears of winter wheat at flowering stage by semantic segmentation. Comput Electron Agric 176:105662.https://doi.org/10.1016/j.compag.2020.105662
26. Chen K, Pang J, Wang J, Xiong Y, Li X, Sun S et al (2019) Hybrid task cascade for instance segmentation. https://doi.org/10.1109/CVPR.2019.00511
27. Li X, Liu Z, Luo P, Loy CC, Tang X (2017) Not all pixels are equal: difficulty-aware semantic segmentation via deep layer cascade.https://doi.org/10.1109/CVPR.2017.684
28. Qiu R, Yang C, Moghimi A, Zhang M, Steffenson BJ, Hirsch CD (2019) Detection of fusarium head blight in wheat using a deep neural network and color imaging. Remote Sens 11:2658. https://doi.org/10.20944/preprints201910.0056.v1
29. Cai Z, Vasconcelos N (2019) Cascade r-cnn: high quality object detection and instance segmentation. IEEE Trans Pattern Anal Mach Intell. https://doi.org/10.1109/TPAMI.2019.2956516
30. Kaiming H, Georgia G, Piotr D, Ross G (2017) Mask r-cnn. In: IEEE international conference on computer vision. https://doi.org/10.1109/TPAMI.2018.2844175
31. Lin TY, Maire M, Belongie S, Hays J, Perona P, Ramanan D, Dollár P, Zitnick CL (2014) Microsoft COCO: common objects in context. In: Fleet D, Pajdla T, Schiele B, Tuytelaars T (eds) Computer vision–ECCV 2014. Springer International Publishing, Cham, Switzerland, pp 740–755

32. Russell BC, Torralba A, Murphy KP, Freeman WT (2008) Labelme: a database and web-based tool for image annotation. Int J Comput Vis 77(1–3). https://doi.org/10.1007/s11263-007-0090-8
33. Gao S, Cheng MM, Zhao K, Zhang XY, Torr PHS (2019) Res2net: a new multi-scale backbone architecture. IEEE Trans Pattern Anal Mach Intell PP(99):1–1. https://doi.org/10.1109/TPAMI.2019.2938758
34. He K, Zhang X, Ren S, Sun J (2016) Deep residual learning for image recognition. In: Proceedings of the IEEE conference on computer vision and pattern recognition, pp 770–778. https://arxiv.org/abs/1512.03385
35. Xie S, Girshick R, Dollár P, Tu Z, He K (2017) Aggregated Residual Transformations for Deep Neural Networks. 2017 IEEE Conference on Computer Vision and Pattern Recognition (CVPR). IEEE. arXiv:1611.05431
36. Dai J, Qi H, Xiong Y, Li Y, Zhang G, Hu H, Wei Y (2017) Deformable convolutional networks. https://doi.org/10.1109/ICCV.2017.89
37. Ren S, He K, Girshick R, Sun J (2015) Faster r-cnn: towards real-time object detection with region proposal networks. IEEE Trans Pattern Anal Mach Intell 39(6). https://doi.org/10.1109/TPAMI.2016.2577031
38. Rossi L, Karimi A, Prati A (2020) A novel region of interest extraction layer for instance segmentation. arXiv:2004.13665
39. Pont-Tuset J, Pablo A, Barron JT, Marques F, Malik J (2016) Multiscale combinatorial grouping for image segmentation and object proposal generation. IEEE Trans Pattern Anal Mach Intell 39(1). https://doi.org/10.1186/10.1109/TPAMI.2016.2537320
40. Caruana R (1998) Multitask learnin. https://doi.org/10.1007/978-1-4615-5529-2_5
41. Rosenfield A, Thurston M, Lee YH (1971) Edge and curve detection for visual scene analysis. IEEE Trans Comput C 20(5):562–569. https://doi.org/10.1109/T-C.1971.223290
42. Bodla N, Singh B, Chellappa R, Davis LS (2017) Soft-nms—improving object detection with one line of code. arXiv:1704.04503
43. He K, Zhang X, Ren S, Sun J (2014) Spatial pyramid pooling in deep convolutional networks for visual recognition. https://doi.org/10.1007/978-3-319-10578-9_23
44. Deng J, Dong W, Socher R, Li LJ, Li FF (2009) ImageNet: a large-scale hierarchical image database. In: IEEE conference on computer vision & pattern recognition. https://doi.org/10.1109/CVPR.2009.5206848
45. Su WH, Zhang J, Yang C, Page R, Steffenson BJ (2021) Automatic evaluation of wheat resistance to fusarium head blight using dual mask-rcnn deep learning frameworks in computer vision. Remote Sens 13(1):1–21. https://doi.org/10.3390/rs13010026

Chapter 7
UAV Multispectral Remote Sensing for Yellow Rust Mapping: Opportunities and Challenges

Jinya Su, Cunjia Liu, and Wen-Hua Chen

Abstract Wheat is threatened by various crop stresses in its life-cycle, where yellow rust is a severe disease significantly impacting wheat yield. This work aims to investigate the use of Unmanned Aerial Vehicle based multispectral remote sensing for winter wheat stress mapping caused by yellow rust disease. A simple unsupervised wheat yellow rust mapping framework is initially proposed by integrating Spectral Vegetation Indices generation, mutual information analysis and Otsu's thresholding. A field experiment is carefully designed by infecting winter wheat with different levels of yellow rust inoculum, where UAV multispectral images are collected at the diseased stage with visible symptoms. Experimental results on the labelled dataset initially show the effectiveness of the proposed unsupervised framework for yellow rust disease mapping. Limitations of the proposed algorithm and challenges of yellow rust detection for real-life applications are also discussed.

Keywords Precision agriculture · Remote sensing · Unsupervised learning · Unmanned Aerial Vehicle (UAV)

This work was supported by Science and Technology Facilities Council (STFC) under Newton fund with Grant No. ST/V00137X/1.

J. Su (✉)
School of Computer Science and Electronic Engineering, University of Essex, Colchester CO4 3SQ, UK
e-mail: j.su@essex.ac.uk; sujinya1990@163.com

C. Liu · W.-H. Chen
Department of Aeronautical and Automotive Engineering, Loughborough University, Loughborough LE11 3TU, Loughborough, UK
e-mail: C.Liu5@lboro.ac.uk

W.-H. Chen
e-mail: W.Chen@lboro.ac.uk

Z. Zhang et al. (eds.), *Unmanned Aerial Systems in Precision Agriculture*, Smart Agriculture 2, https://doi.org/10.1007/978-981-19-2027-1_7

7.1 Introduction

Crops are threatened by various stresses (e.g., pests, diseases, drought, nutrient deficiencies) in their life-cycle. Wheat, the most widely grown cereal crop in the world, is able to provide 20% of protein and food calories for 4.5 billion people worldwide, but is also facing severe challenges from abiotic stresses, pathogens and pests due to climate changes and inappropriate management strategies, posing serious threats on food security. Among various crop diseases, wheat yellow (or stripe) rust is a devastating global wheat disease, particularly in the regions with temperate climates [1]. This disease is able to develop and spread very quickly under favourable conditions such as a suitable temperature of 5–24 °C, a moderate precipitation in spring (for winter wheat) and suitable wind conditions (for spore spread) [2].

Generally speaking, there are two available approaches to control yellow rust disease including chemical control and genetic resistance (please refer to [3] and the references therein). Conventional chemical control methods for yellow rust disease rely on calendar-based (timing) and uniform (blanket) application of pesticides regardless of the current disease status (e.g. stress level and its spatial distribution), which not only results in a higher cost (more pesticide) but also inevitably increases the likelihood of ground water contamination and pesticide residues in agricultural products, generating significantly economical, environmental and social burdens. It is highly desirable to develop an automated and non-destructive wheat disease mapping system so that a decision-based precision (site-specific) management strategy can be implemented [4] at the right time/location while with the right amount of pesticides.

Wheat yellow rust disease generally results in certain physical and chemical changes on wheat leaves such as ChlorophyII content reduction, water loss, and even visible rust symptoms at later stages (i.e. yellow-orange to reddish-brown spores) [5]. It is noted that when visible rust symptoms appear on wheat canopy, the chemical treatment is to stop its spread to surrounding areas. These changes can be observed by human eyes and can also be captured by optical sensors such as RGB [3, 6], multispectral [4] and hyperspectral cameras [1, 7]. Human inspection is time-consuming, labour-intensive, prone to error, and so not suitable for real-life applications at large scales. Different cameras also have pros and cons in terms of price, weight, flexibility and performance. In this study, multispectral camera is adopted since compared against RGB camera, it possesses spectral bands beyond the three visible bands (e.g. NIR band), and in comparison to hyperspectral camera [8], it is much easier to operate (e.g. imaging, calibration and orthomosaic) and is usually with a much lower price.

In addition, different sensing platforms are also available for crop stress monitoring, which range from ground proximity sensing [3] to aircraft (or even satellite) remote sensing [4]. It is shown in the existing studies that UAV based remote sensing is able to provide a user-defined spatial-temporal image resolution (e.g., imaging period, flight height), a low cost and a high flexibility, and therefore is drawing ever-increasing popularity for field-scale applications since 2010 in different application

domains such as disease monitoring [1], weed mapping [9], stress detection [10], crop parameter extraction [11] among many others. Therefore, this work aims to adopt UAV based multispectral remote sensing for the automated wheat yellow rust disease mapping for the purpose of target treatment.

There are also studies on using UAV based multispectral remote sensing for wheat yellow rust disease mapping [2, 4, 12]. For example, yellow rust disease mapping is formulated as a supervised classification problem, and both conventional machine learning (i.e. random forest) and state-of-the-art deep learning algorithm (e.g. U-net) [13] are adopted to address the semantic segmentation problem in [2, 4], respectively. It is also shown that deep Convolutional Neural Network (CNN) outperforms the random forest approach due to its capability in learning both spectral and spatial information concurrently in an end-to-end manner. Although this method is able to obtain a good result in small local areas, its generalization performance (location-wise, season-wise, variety-wise) is unclear as the model is trained by using the dataset from one variety and a small area in a supervised manner.

This work aims to initially develop a simple unsupervised yellow rust disease mapping framework by integrating UAV based remote sensing, multispectral imaging, Spectral Vegetation Indices (SVIs) generation, spectral analysis and Otsu's thresholding. The proposed framework is initially validated by field experiments, where multispectral images and ground data are recently collected on yellow rust infected wheat field using a small UAV at about 20 m above ground with a spatial resolution of 1.3 cm in 2019. To the best of the authors' knowledge, this work is the first attempt to develop a unsupervised learning framework to address the problem of wheat yellow rust disease mapping. To be more precise, the main contributions are summarized as below.

(1) A unsupervised learning framework is proposed for wheat yellow rust disease mapping based on SVI analysis and thresholding, and is initially validated by field experiments;
(2) The best SVIs for wheat segmentation from background pixels, and yellow rust disease segmentation from healthy wheat pixels are obtained based on SVI generation and mutual information analysis;
(3) The challenges of wheat yellow rust disease mapping in real-life applications are also discussed in terms of early detection, image resolution, disease identification, model generalization, time window for disease management.

7.2 UAV Remote Sensing

7.2.1 Wheat Yellow Rust Experiment

The field experiments are carried out at Caoxinzhuang experimental station of Northwest Agriculture and Forestry (A&F) University, Yangling, China in 2019 (please refer to Fig. 7.1 for the geographic location). Background information about the

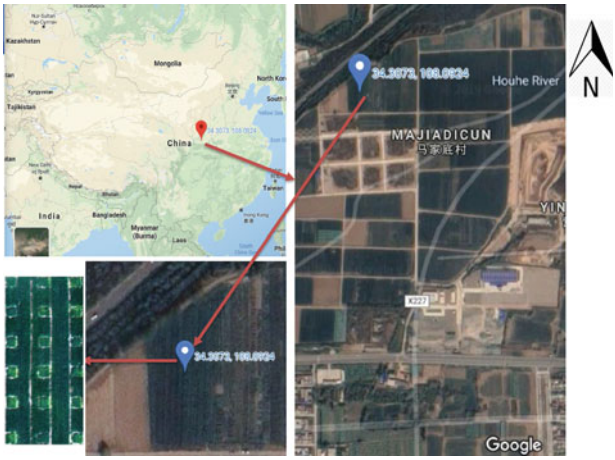

Fig. 7.1 Geographic location of the experimental wheat field

region is referred to the previous studies [4]. In this study, wheat variety Xiaoyan 22 is chosen since it is easily susceptible to yellow rust disease. The yellow rust inoculation is done at wheat seedlings stage in March/2019, where more detailed information such as inoculation method is available in [2]. In term of experiment layout, as displayed in Fig. 7.2, letters A, B, and C represent the three replicates to reduce random errors; numbers 0–5 denote the different levels of yellow rust inoculum with 0 being empty (no inoculum) and 5 being the highest level of inoculum; each plot with a size of 2 m × 2 m in each replicate is randomly inoculated with one of the six levels of yellow rust inoculum: 0 g (health wheat plots for blank comparison), 0.15 g, 0.30 g, 0.45 g, 0.6 g and 0.75 g corresponding to the level of 0–5, respectively. Disease cross-infection was maximally avoided by separating all 18 wheat plots from each other via healthy wheat gaps.

7.2.2 UAV Remote Sensing

7.2.2.1 UAV Imaging Platform

Different commercial UAVs (e.g. fixed-wing UAV [14] for large-scale operation, multi-rotor UAV for small areas with flexible/low flight heights) and multispectral cameras (e.g. Parrot Sequoia, RedEdge and Altum from MicaSense, P4 Multispectral from DJI) can be integrated to be the UAV imaging platform. In this study, a commercial off-the-shelf aircraft named DJI Matrice 100 (M100) Quad-copter (DJI Company, Shenzhen, China) and a 5-band multispectral camera (RedEdge, MicaS-

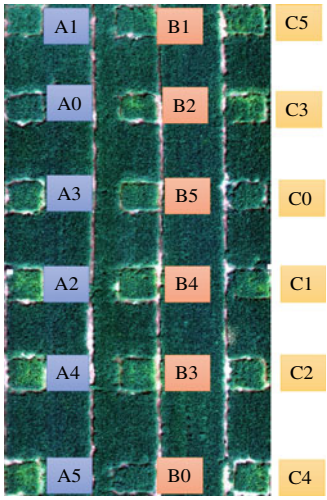

Fig. 7.2 Wheat yellow rust inoculum experiment: three replicates (column-wise) with various levels of yellow rust inoculum in the range of 0–5, where the false-color RGB image from [2] is at diseased stage on 02/May/2019

ense Inc., Seattle, USA) are integrated to be the low-altitude UAV remote sensing platform (please refer to [2] for the graphic illustration) for yellow rust disease mapping.

7.2.2.2 Data Collection

In this study, data collection is done on 02/May/2019, when yellow rust is in diseased stage with visible symptoms (e.g., yellow color by spores). The UAV flight height is set to be about 20 m above ground, where the ground spatial resolution of the image is about 1.3 cm/pixel after image stitching. Commercial free-of-charge software, Pix4DCapture, is used to plan, monitor and control the UAV for data collection. In particular, the mode of Polygon for 2D maps in Pix4DCapture is chosen with an image overlap and sidelap up to 75%, the UAV forward speed is set at 1 m/s and the camera triggering period is also 1 sec. In addition, before the flight, reflectance calibration panel is also imaged at 1 meter height so that an accurate reflectance data can be obtained for the follow-up image calibration even under environmental (including lighting) variations. The UAV flight track along with camera triggering points, the overlapping images under the defined flight track and the calibrated NIR orthomosaic are shown in Fig. 7.3, respectively.

RedEdge camera is equipped with GPS module and is able to capture five raw narrow bands simultaneously including Blue, Green, Red, RedEdge and NIR bands (please refer to Fig. 7.4 for one sample image of the RedEdge camera). All necessary information for the follow-up image stitching is embedded in each image such as GPS information and camera information (e.g. camera model, exposure time, focal length).

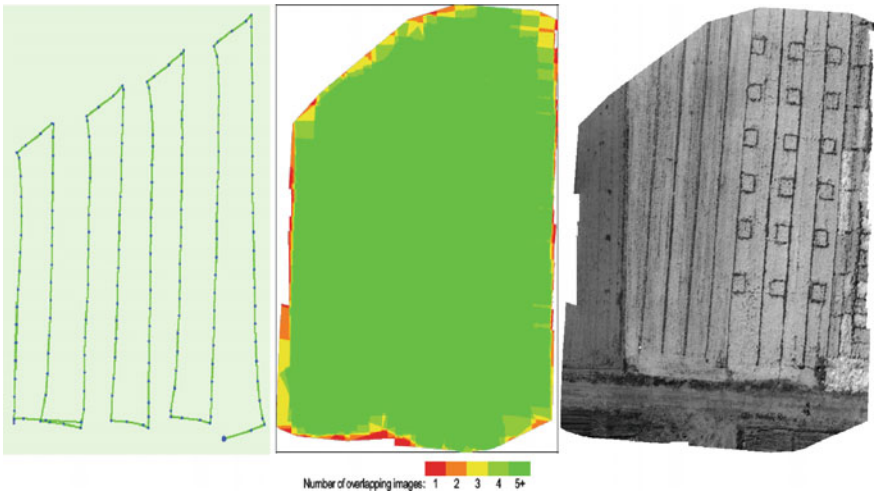

Fig. 7.3 UAV flight track and camera triggering points (left); the number of overlapping images at each points (middle); and the raw calibrated NIR orthomosaic (right)

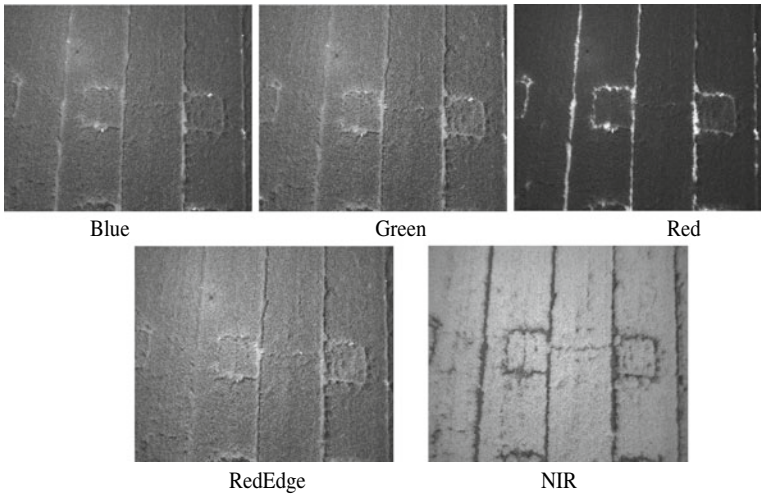

Fig. 7.4 Sample RedEdge image including five raw spectral bands

7.2.3 Image Pre-processing and Data Labelling

After all images are collected, a number of image preprocessing steps are then conducted offline to generate the calibrated (using CRP panel) and georeferenced reflectance data for each spectral band and different SVIs. This can be achieved in commercial (e.g. Pix4DMapper, Agisoft Metashape, DroneDeploy) or open-source

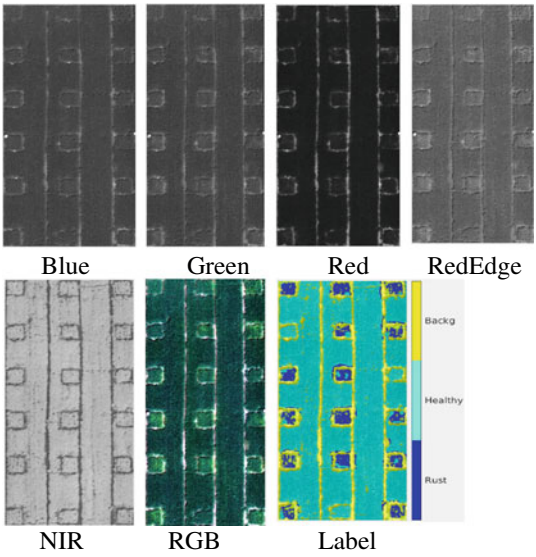

Fig. 7.5 ROI for different spectral bands, false-color RGB image and the final Label image from [2]

software (e.g. WebODM). In this study, Pix4DMapper is adopted, where the detailed steps are referred to [2, 4] such as initial processing, orthomosaic generation and reflectance calibration for each band. The outputs include five GeoTIFF images and the defined SVIs of the covered area, where the NIR orthomosaic is displayed in Fig. 7.3 as an example. All orthomosaic images of the five spectral bands and SVIs can be then input into MATLAB environment, where image rotation (by using the function "imrotate") and region of interest (ROI) can be performed and defined for the follow-up analysis. The ROI for five spectral bands, the false-color RGB image and data labelling process are shown in Fig. 7.5.

To achieve yellow rust disease mapping (e.g., spectral analysis and SVI selection in this study) for wheat field, image labelling is required. In this study, three classes are defined for the field of interest, which include plants with visible yellow rust lesions pixels (Rust class), healthy wheat pixels (Healthy class) and background pixels (Backg class, i.e. non-vegetation soil background). The details for image labelling is referred to [2], which mainly relies on low-altitude high-resolution RGB image and manual visual labelling. The main steps for this labelling method are summarized for the purpose of completeness : (1) false-color RGB image (see Fig. 7.5) is first generated by using the calibrated Red, Green and Blue bands in Matlab with function "imadjust" for brightness adjustment, on this basis, the yellow rust regions can be manually and visually defined; (2) the classical spectral index Optimized Soil Adjust Vegetation Index (OSAVI) [15] generated from the five spectral bands is first used to segment wheat pixels from the background pixels; surely other vegetation segmentation methods can also be adopted including machine learning based methods [11]; (3) the yellow rust infected wheat pixels, healthy wheat pixels and the background pixels can be then defined (see the final Label image in Fig. 7.5).

7.3 Yellow Rust Disease Mapping

This section considers the problem of yellow rust disease mapping, where the overall framework is displayed in Fig. 7.6 such as feature definition, spectral and mutual information (MI) analysis, wheat segmentation and rust segmentation. Different elements in the proposed framework are introduced in the following subsections, respectively.

7.3.1 Spectral Analysis

Spectral analysis of the three selected classes is first performed to see the differences for three classes. It has been shown in many previous studies that some SVIs calculated from the five raw spectral bands may be able to provide an even better ability in mapping yellow rust disease [4, 12] against the healthy wheat and background pixels. Therefore, in addition to the five raw spectral bands, 18 widely used SVIs are also calculated to see whether they are able to provide better yellow rust disease mapping performance (please refer to [4] for the definitions of the 18 widely used SVIs). The mean reflectance values of the original five bands and 18 SVIs for the three classes are calculated respectively in MATLAB2020b and displayed in Figs. 7.7 and 7.8.

It can be visually seen from Figs. 7.7 and 7.8 that different classes have different reflectance values at the five bands and SVIs. For example, Healthy wheat pixels have the highest NIR values but the lowest red values, which is mainly due to the high ChlorophyII content in healthy plants over diseased wheat or background. It is, however, noted that the mean value is NOT sufficient for quantitatively evaluating the capabilities of different bands/SVIs in wheat yellow rust disease mapping as the uncertain information (e.g. variance) is missing. And so feature ranking method will be introduced in the next subsection.

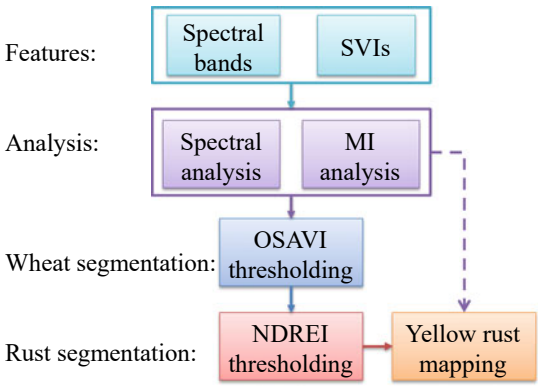

Fig. 7.6 Overall framework for the proposed wheat yellow rust disease mapping system including feature definition, spectral and MI analysis, wheat and rust segmentation

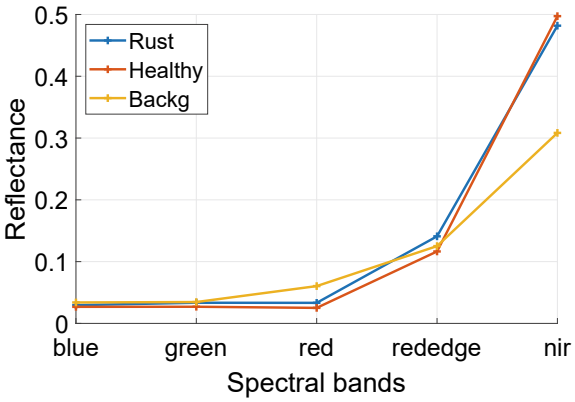

Fig. 7.7 Spectral reflectance of the five bands for the three classes including rust infected wheat (Rust), healthy wheat (Healthy) and background (Backg) pixels

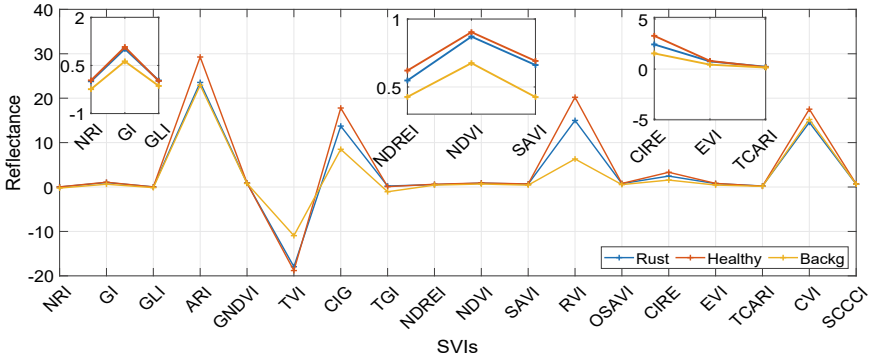

Fig. 7.8 Spectral reflectance of the 18 SVIs for three classes including Rust, Healthy and Backg classes

7.3.2 Mutual Information Ranking

In order to test the different discriminating capabilities of the five spectral bands and 18 SVIs in yellow rust disease mapping, MI based feature ranking is adopted (please refer to [16] and the references therein for different feature selection methods). The class label is defined into three categories, where *Category 1* contains three classes including Rust, Healthy and Backg, *Category 2* contains two classes including Rust and Healthy with Backg being removed, *Category 3* contain two classes including Wheat (the Rust and Healthy classes are integrated into Wheat) and Backg. The MI values between each band/SVI and the class label (Category 1 with three classes) are calculated and displayed in Fig. 7.9, while the MI values between each band/SVI and the class label (Category 2 and Category 3) are displayed in Fig. 7.10

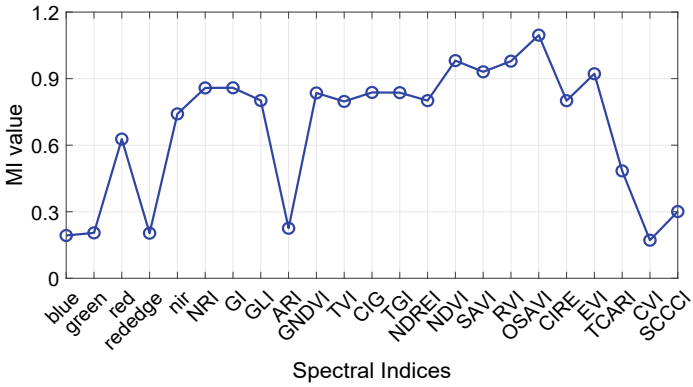

Fig. 7.9 MI values between bands/SVIs and Category 1 class label

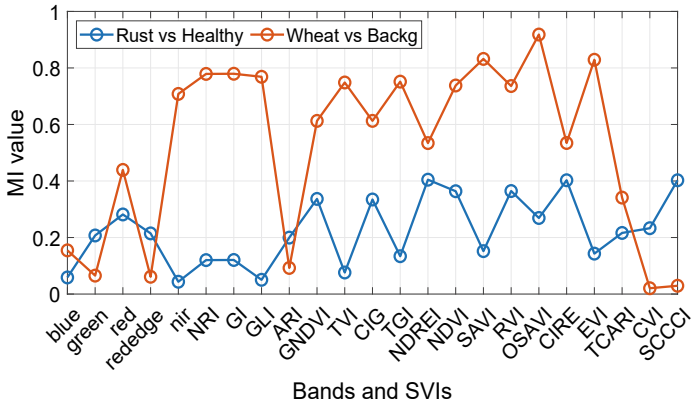

Fig. 7.10 MI values between bands/SVIs and Category 2/3 class labels

It follows from Figs. 7.9 and 7.10 that

(1) Different spectral bands/SVIs have different MI values with different class labels and therefore with different discrimination capabilities;
(2) OSAVI has the best discrimination capability for the three classes (Fig. 7.9), this is mainly due to its strongest capability in discriminating wheat pixels from background pixels (red line of Fig. 7.10).
(3) Red band is the best one among the five spectral bands for both wheat pixel segmentation from the background pixels, and yellow rust disease pixel segmentation from the healthy wheat pixels.
(4) SVIs may have a better discrimination capability (i.e. with a higher MI value) than the raw spectral bands, although the capabilities of different SVIs differ a lot. And NDREI has the strongest discrimination capability for separating Rust class from Healthy class.

7.3.3 Unsupervised Classification

Based on the ranking results via mutual information in Sect. 7.3.2, this section develops a simple unsupervised classification approach based on SVI thresholding. Considering the fact that the best discrimination SVIs for Rust vs Healthy, and Wheat vs Backg are different, wheat segmentation and rust segmentation are done one by one based on their best SVIs.

7.3.3.1 Wheat Segmentation

The first step is wheat segmentation. It follows from Fig. 7.10 that OSAVI has the strongest discrimination capability in separating Wheat class from Backg class, where its histogram for Wheat and Backg class is shown in Fig. 7.11. Then the well-known Otsu's method can be adopted to automatically choose the optimal thresholding for wheat segmentation where the wheat pixels have higher OSAVI values.

7.3.3.2 Yellow Rust Segmentation

After the Wheat class is separated from the Backg class, the yellow rust separation from wheat class is then considered. It follows from Fig. 7.10 that NIR and NDREI have the weakest and strongest discrimination capability in separating Rust class from Healthy class, where their histograms for Rust and Healthy class are shown in Fig. 7.12. Therefore, the NDREI index is chosen for Rust segmentation, where the well-known Otsu's method is adopted again to automatically choose the optimal thresholding, where the healthy wheat pixels have higher NDREI values.

Following these two supervised segmentation steps, the final classification result is shown in Fig. 7.13. The quantitative classification results are not provided in this initial study.

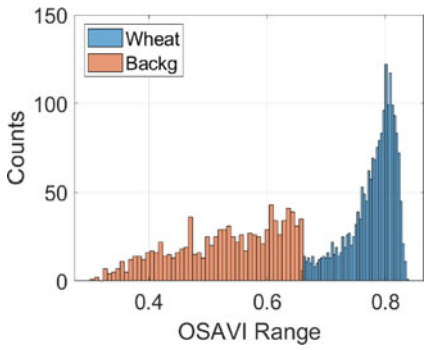

Fig. 7.11 Histogram of OSAVI for Wheat and Backg class

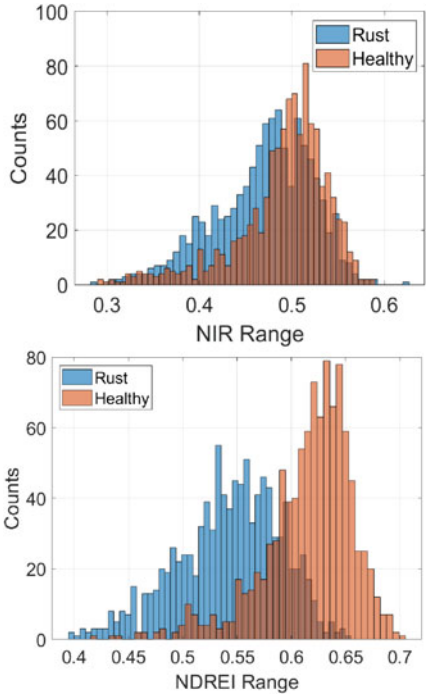

Fig. 7.12 Histogram of NIR and NDREI for Rust and Healthy class

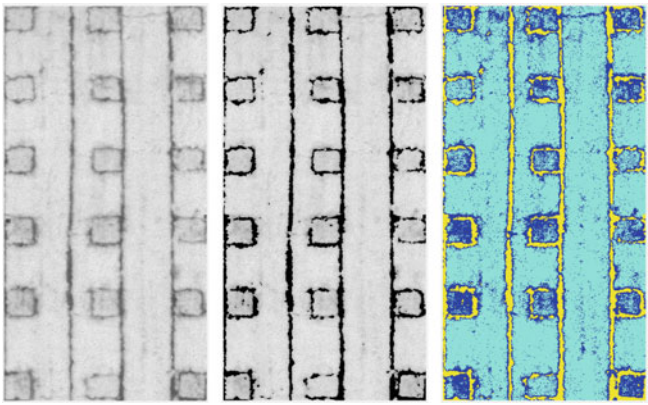

Fig. 7.13 NDREI (left), NDREI with Backg (middle) and the classification results based on the simple unsupervised approach (right)

7.4 Discussion

In this section, the pros and cons of the proposed method are discussed against the state-of-the-art methods. On this basis, the challenges of UAV remote sensing for yellow rust disease mapping are discussed in the context of real-life field applications.

7.4.1 Pros and Cons

7.4.1.1 Supervised Versus Unsupervised Learning

In this study, data labelling is to assess the reflectance differences of various classes and evaluate the different discriminating capabilities of various spectral bands and SVIs. Then unsupervised method is proposed in Sect. 7.3.3 for wheat yellow rust disease mapping based on automated thresholding of different SVIs. It is noted that most existing methods for wheat yellow rust disease mapping are based on supervised learning by using conventional machine learning ([4]) or state-of-the-art deep learning ([2]).

(i) Unsupervised approach is simple to implement, and does not require labelled dataset for model training. This is attractive for crop disease mapping, since obtaining a large amount of high-quality (and representative) labelled dataset is costly, labour-intensive and time-consuming and so not practically feasible for yellow rust disease mapping. However, the disease mapping performance of the unsupervised approach (particularly the one in this study) is relatively limited (mainly due to the limited information used in the approach). In this regards, more advanced supervised approaches should be further developed to embed more useful information.

(ii) Supervised approach, particularly the state-of-the-art deep Convolutional Neural Network, is able to provide better performance than unsupervised ones. However, this approach generally requires a large volume of high-quality labelled dataset for its model training. Obtaining raw UAV remote sensing images is not hard, however, *obtaining a representative and high-quality labelled dataset under different crop varieties, crop growth and disease development stages, and under various environmental condition is a challenge. In this regards, developing semi-automatic labelling approach to generate labelled dataset may be a feasible and promising solution.*

7.4.1.2 Spectral Information Versus Spatial Information

For (yellow rust) disease mapping in wheat field, different types of information can be adopted which may include spectral information (different spectral bands), spatial information (disease usually appears from small regions and spreads to the sur-

rounding areas), or even temporal information (combining different measurements together).

(i) Disease mapping based on purely spectral information may result in a high proportion of false positives (pepper and salt noises as shown in Fig. 7.13) due to the absent of spatial information in the algorithm.
(ii) Different methods for embedding spatial information are available in the literature including at feature stage or post-processing stage. Fusing spectral and spatial information by using deep CNNs (e.g. FCN [17], SegNet, U-Net [2, 18] would be the trend. However, deep learning approach generally requires more labelled data (a representative pixel-wise labelled dataset is even harder than image level labelled dataset) than conventional machine learning approaches, which is a challenge as highlighted in Sect. 7.4.1.1 for supervised methods.

7.4.2 Challenges for Real-Life Applications

The challenges of wheat yellow rust disease mapping system in real-life applications are summarized as below.

(1) **Early disease detection** of wheat (yellow rust) is paramount so that early intervention can be conducted to stop its spread to the surrounding areas. However, early disease detection is generally not easy. UAV remote sensing, as a top viewing method, can only see the crop canopy information. Diseases start from the bottom leaf layers can not be detected until the changes appear on the top leaf layers, which may be too late for its treatment although still useful for stopping its spread. In this regards, hyperspectral imaging which does not rely on visual symptoms may be a proposing solution, however, this method is still costly, not easy to operate, and poses challenges for follow up image processing.
(2) **Image resolution** is important for (early) wheat disease mapping. However, image resolution highly relies on UAV flight altitude and therefore there is a trade-off between image resolution and working efficiency. As flying higher is more efficient but with a lower image resolution, while flying lower obtains a higher image resolution but is generally inefficient. The required image resolution for yellow rust disease mapping (at different disease development stages) should be investigated.
(2) **Disease identification** is also challenging. This is because different crop stresses (e.g., diseases/pests) may result in very similar (top viewing) symptoms on the crop (wheat) such as the ChlorophyII content reduction, water loss, and visual symptoms at later stages. Therefore, disease/pest habitat (environmental) information (e.g. temperature, humidity, season) may be useful to reduce the scope of crop stresses for the purpose of disease identification.
(3) **Model generalization** is important but at the same time challenging for wheat (yellow rust) disease mapping. This is because the developed algorithms (particularly supervised learning algorithms) are actually facing very complex oper-

ating environments. How to guarantee the algorithm performance under different wheat varieties, wheat growth stages, disease development stages, lighting/environmental conditions is generally challenging. As a result, it is yet to be tested whether an algorithm trained from one wheat variety can work in other varieties (variety-wise), an algorithm trained from history dataset can work in future seasons (season-wise), or an algorithm trained in one location can work in other locations (location-wise). This validation method should be considered in future publications in addition to conventional random splitting of the lumped dataset.

(4) **Time window** for wheat (yellow rust) disease control is generally short, as a result, the issue that covering a large area of interest within a short time period should also be considered in real-life applications. Multiple UAVs and parallel processing may provide the solution in terms of data collection and data processing.

7.5 Conclusions

This work considers the problem of wheat yellow rust disease mapping by using UAV based multispectral remote sensing. A simple unsupervised yellow rust disease mapping framework is developed based on spectral analysis, mutual information analysis and Otsu's thresholding. Field study is conducted to generate a dataset to initially validate the developed framework. It is shown that (i) OSAVI is the best SVI for segmenting wheat from background pixels; (ii) NDREI is the best SVI for segmenting yellow rust infected wheat from healthy wheat pixels. The pros and cons of the simple unsupervised algorithm is discussed by comparing against supervised algorithms and the ones with both spectral and spatial information. Moreover, the challenges of yellow rust disease mapping in real-life applications are also discussed.

References

1. Zhang X, Han L, Dong Y, Shi Y, Huang W, Han L, González-Moreno P, Ma H, Ye H, Sobeih T (2019) A deep learning-based approach for automated yellow rust disease detection from high-resolution hyperspectral uav images. Remote Sens 11(13):1554
2. Su J, Yi D, Su B, Mi Z, Liu C, Hu X, Xu X, Guo L, Chen W-H (2020) Aerial visual perception in smart farming: field study of wheat yellow rust monitoring. IEEE Trans Ind Inform 17(3):2242–2249
3. Mi Z, Zhang X, Su J, Han D, Su B (2020) Wheat stripe rust grading by deep learning with attention mechanism and images from mobile devices. Front Plant Sci 11
4. Su J, Liu C, Coombes M, Hu X, Wang C, Xu X, Li Q, Guo L, Chen W-H (2018) Wheat yellow rust monitoring by learning from multispectral uav aerial imagery. Computers and electronics in agriculture 155:157–166

5. Zhang J, Pu R, Loraamm RW, Yang G, Wang J et al (2014) Comparison between wavelet spectral features and conventional spectral features in detecting yellow rust for winter wheat. Comput Electron Agric 100:79–87
6. Liu W, Yang G, Xu F, Qiao H, Fan J, Song Y, Zhou Y (2018) Comparisons of detection of wheat stripe rust using hyperspectral and uav aerial photography. Acta Phytopathol Sin 48(2):223–227
7. Guo A, Huang W, Dong Y, Ye H, Ma H, Liu B, Wu W, Ren Y, Ruan C, Geng Y (2021) Wheat yellow rust detection using uav-based hyperspectral technology. Remote Sens 13(1):123
8. Adão T, Hruška J, Pádua L, Bessa J, Peres E, Morais R, Sousa JJ (2017) Hyperspectral imaging: A review on uav-based sensors, data processing and applications for agriculture and forestry. Remote Sens 9(11):1110
9. Su J, Yi D, Coombes M, Liu C, Zhai X, McDonald-Maier K, Chen W-H (2022) Spectral analysis and mapping of blackgrass weed by leveraging machine learning and uav multispectral imagery. Comput Electron Agric192:106621
10. Zhang C, Kovacs JM (2012) The application of small unmanned aerial systems for precision agriculture: a review. Precis Agric 13(6):693–712
11. Zhang T, Su J, Liu C, Chen W-H (2019) Bayesian calibration of aquacrop model for winter wheat by assimilating uav multi-spectral images. Comput Electron Agric 167:105052
12. Su J, Liu C, Hu X, Xu X, Guo L, Chen W-H (2019) Spatio-temporal monitoring of wheat yellow rust using uav multispectral imagery. Comput Electron Agric 167:105035
13. Wang Y, Su J, Zhai X, Meng F, Liu C (2022) Snow coverage mapping by learning from sentinel-2 satellite multispectral images via machine learning algorithms. Remote Sens 14(3)
14. Smith J, Su J, Liu C, Chen W-H (2017) Disturbance observer based control with anti-windup applied to a small fixed wing uav for disturbance rejection. J Intell Robot Syst 88(2):329–346
15. Rondeaux G, Steven M, Baret F (1996) Optimization of soil-adjusted vegetation indices. Remote Sens Environ 55(2):95–107
16. Su J, Yi D, Liu C, Guo L, Chen W-H (2017) Dimension reduction aided hyperspectral image classification with a small-sized training dataset: experimental comparisons. Sensors 17(12):2726
17. Huang H, Deng J, Lan Y, Yang A, Deng X, Zhang L (2018) A fully convolutional network for weed mapping of unmanned aerial vehicle (uav) imagery. PloS One 13(4):e0196302
18. He K, Gkioxari G, Dollár P, Girshick R (2017) Mask r-cnn. In: Proceedings of the IEEE international conference on computer vision, pp 2961–2969

Chapter 8
Corn Goss's Wilt Disease Assessment Based on UAV Imagery

Anup Kumar Das, Jithin Mathew, Zhao Zhang, Andrew Friskop, Yuxiang Huang, Paulo Flores, and Xiongzhe Han

Abstract Goss Wilt is a common and serious disease during corn production. With a goal of automatic disease monitoring, this study assessed Goss's Wilt disease severity using machine (ML) and deep learning (DL) algorithms. A dataset containing 200 corn plot images was generated from an unmanned aerial vehicle (UAV) flying at five

A. K. Das · J. Mathew · Z. Zhang (✉) · P. Flores
Department of Agricultural and Biosystems Engineering, North Dakota State University, Fargo, ND, USA
e-mail: zhao.zhang.1@ndsu.edu

A. K. Das
e-mail: anup.das@ndsu.edu

J. Mathew
e-mail: jithin.mathew@ndsu.edu

P. Flores
e-mail: paulo.flores@ndsu.edu

Z. Zhang
Key Lab of Modern Precision Agriculture System Integration Research, Ministry of Education of China, China Agricultural University, Beijing 100083, China

Key Lab of Agriculture Information Acquisition Technology, Ministry of Agriculture and Rural Affairs of China, China Agricultural University, Beijing 100083, China

A. Friskop
Department of Plant Pathology, North Dakota State University, Fargo, ND 58102, USA
e-mail: andrew.j.friskop@ndsu.edu

Y. Huang
College of Mechanical and Electronic Engineering, Northwest A & F University, Yangling, Shaanxi, China
e-mail: hyx@nwsuaf.edu.cn

X. Han
Department of Biosystems Engineering, College of Agriculture and Life Sciences, Kangwon National University, Chuncheon 24341, Korea
e-mail: hanxiongzhe@kangwon.ac.kr

Interdisciplinary Program in Smart Agriculture, College of Agriculture and Life Sciences, Kangwon National University, Chuncheon 24341, Korea

Z. Zhang et al. (eds.), *Unmanned Aerial Systems in Precision Agriculture*,
Smart Agriculture 2, https://doi.org/10.1007/978-981-19-2027-1_8

different mission heights (15, 30, 45, 60, and 75 m) above the ground level (AGL). Three different datasets including non-augmentation, segmentation and augmentation were prepared. The augmentation dataset consisting of 6200 images was prepared using geometric augmentation techniques, such as rotation, and flip. Eight different ML algorithms (i.e., Logistic Regression, Ada Boost, Gradient Boosting, Support Vector Machine, Multilayer Perceptron, Random Forest, Naive Bayes, K-Nearest Neighbors) and two different DL algorithms (i.e., GoogLeNet and ResNet18) were implanted to classify Goss Wilt severity as a binary issue (i.e., high and low). Two different types of features, including textural (contrast, dissimilarity, homogeneity, angular second moment) and color (hue, saturation, value, lightness, chromatic components: a* and b*, red, green, blue) features were extracted from individual plot image. For ML, the Random Forest yielded 0.99 precision, 0.99 recall and 0.99 F-score in augmented dataset and outperformed all other classifiers. For DL, Resnet18 achieved slightly better results: 0.81 precision, 0.78 recall and 0.79 F-score than GoogleNet, which has 0.75 precision, 0.70 recall, and 0.73 F-score. The ML model (Random Forest) performed satisfactorily by resulting in higher precision, recall and F-score in augmented dataset. However, ML models underperformed on segmentation dataset. Therefore, Random Forest coupled with UAV imagery is a potential valuable tool for automatic assessment of Goss Wilt disease.

Keywords Corn · Goss's Wilt · Machine learning · Deep learning

8.1 Introduction

Corn (*Zea mays L.*) accounts for more than 95% of the feed grain produced in the United States [27]. Goss's Wilt, a corn leaf disease, has been recognized as one of the most yield-limiting diseases, causing up to 50% production losses in North Dakota [5]. Field visits coupled with visual observation are used to assess Goss Wilt, which is time consuming (inefficiency), subjective, and leading to incorrect assessments due to evaluator's fatigue. As a result, developing an automated, quick, and reliable approach for Goss Wilt disease monitoring has been a top priority.

Unmanned aerial vehicles (UAVs) appear in a number of agricultural applications due to rapid and high-quality collected data, and ability to replace human labor for data collection [17]. The UAV imagery is now extensively used in agriculture for crop disease detection, such as citrus canker [1], vine disease [9, 10], yield monitoring for rice grain [12], glyphosate-resistant and glyphosate-susceptible weed and pest management [26], crop health monitoring of winter corn and barley [21]. Kerkech et al. [9] also used UAV imagery to develop automatic grape vine detection using a convolutional neural network (CNN) and achieved 96% detection accuracy.

Kerkech et al. [10] proposed UAV based automated vine disease detection system using deep learning (DL) techniques and achieved more than 92% detection accuracy. A majority of the existing studies focus on the identification of diseases. However, very few researchers extended the detection problem to the disease severity levels.

Liu et al. [14] developed a relationship between image parameters and wheat powdery mildew severity and achieved positive correlations. They extracted several features from the UAV images and found color features had a positive correlation with powdery mildew severity. Salgadoe et al. [23] used two different types of images (RGB and eight bands satellite image) for quantifying the severity of root rot disease of avocado and found promising results generated from the satellite images. However, limited study has been conducted using RGB color images for determining the severity of Goss's Wilt diseases.

Progress and applications of sensing and automation technology in agriculture have benefitted the agricultural production [7, 8, 15, 29, 30, 33–35]. The current advances in drone technology provide new ways in collecting crop information and assisting growers in decision making [3, 4, 31]. Researchers used machine learning (ML) techniques to detect corn leaf disease. Supervised ML pipeline involves data preparation, feature extractions, feature selection, training, testing, and validation. For ML algorithms, features (e.g., color, textural, and shape) are usually extracted manually, after which they are generally selected using selection algorithms and used for training. Ren et al. [22] extracted 129 features, including 30 color features, 9 shape features, and 90 textural features and observed shape features highly contributing to classify spot diseases in corn leaves. Panigrahi et al. [18] used ML techniques, including random forest (RF), decision tree (DT), and naive bayes (NB), to accurately identify corn leaf diseases. Support vector machine (SVM) classifier was used for corn leaf disease classification, which generated a high success rate of 87% by Meng et al. [16], 96% by Liu et al. [14] and 89% by Ren et al. [22]. Kusumo et al. [11] used SVM, DT, RF, and NB to distinguish healthy leaves from corn gray leaf spot, common rust, and leaf blight and achieved good performance from SVM with color features and RF with local features (Speeded Up Robust Features). Many studies utilized ML systems to predict the severity of plant leaf diseases [2, 13, 19, 24]. However, few studies on the severity of Goss Wilt disease in corn have been conducted.

In recent years, the use of DL in agriculture has grown considerably. Deep neural networks consisting of layers can learn high-level features from data. For feature extraction, ML needs domain knowledge, while DL can extract features automatically, and eliminate the need for human feature extraction and selection. Wang et al. [28] presented an automated plant disease severity assessment system based on VGG16, VGG19, Inception-v3, and ResNet50. They categorized apple leaf images into four groups: healthy, early, middle, and end stage of apple leaf black rot. They reported that the VGG16 model outperformed the VGG19, Inception-v3, and ResNet50 models, yielding a 90% accuracy. For categorizing and evaluating the severity of coffee leaf biotic into four categories (i.e., healthy, low, and very low), Esgario et al. utilized AlexNet, GoogLeNet, VGG16, ResNet50, and MobileNetV2 and effectively evaluated severity with 87% accuracy. DL methods, on the other hand, are data hungry and computationally expensive. With small dataset, training DL algorithms may easily result in model overfitting. Several studies trained DL algorithms using augmentation datasets to cope with small datasets and reduce the risk of model overfitting. Data augmentation is an artificial data enlargement technique that optimizes parameters and reduces model overfitting.

Researchers utilized data augmentation techniques including random rotation, shearing, zooming, and flipping, horizontal and vertical mirroring, rotation, and color brightness, contrast, and saturation (Esgario et al. 2020) [28] and observed uses of the techniques improved system accuracy. Zhang et al. [32] also observed 5% of accuracy improvement using data augmentation techniques. Thus, for small dataset, it is desirable to conduct data augmentation before training models.

With a final goal of realizing automatic corn Goss's Wilt disease detection, this study focuses on testing different ML and DL algorithms and then recommend the desirable one. Specific research objectives are to: (1) collect UAV images and then prepare the dataset, (2) train, test and compare different ML and DL algorithms, (3) Recommend a model for assessing Goss's Wilt disease.

8.2 Material and Methodology

8.2.1 Data Collection and Data Preprocessing

A field, located in Horace, North Dakota, U.S., was rented from a local farmer (Fig. 8.1). A DJI Phantom 4D RTK (DJI-Innovations, Inc., ShenZhen, China) drone equipped with a 20-megapixel 2.54 cm CMOS camera with 4864 × 3648 resolution and a high-precision (±10 cm) RTK GNSS system was utilized to capture image data on August 11, 2020, at 1:00 PM (local time; sunny). A total of five missions were carried out at five different flying heights, including 15, 30, 45, 60, and 75 m above ground level (AGL). The flights were set 80% of the side and front overlap and at a speed of 2.5 m/s. Following data collection, a plant pathologist visited each plot to manually and visually inspect the Goss's Wilt severity, which was categorized into two grades (high and low severity). The experimental plots (40 in total) were divided into two categories: high severity (23 in total) and low severity (17 in total).

The individual images obtained from the UAV for the five flight altitudes were automatically stitched using Pix4D software (Pix4D SA, Lausanne, Switzerland)

Fig. 8.1 Location of the field in Google Maps™ (Adapted from Google LLC., 2021)

and then cropped in ImageJ (ImageJ version 1.50e, USA; http://rsbweb.nih.gov/ij). Plots from the cropped images were generated using a plot splitting tool developed in this study (Fig. 8.2). A total of 200 plot images (40 plots/height × 5 heights) were generated. The developed tool took an image as input and divided it into a grid (4 × 10) for given input (column: 4 and row: 10) automatically where each cell represented a plot. The plot image dimensions (i.e., length and width) were calculated using Eqs. (8.1) and (8.2). A region of interest (ROI) was calculated by Eqs. (8.3) and (8.4) and placed in each cell using the function setRoi (xx, yy, roiw, roih) method. The function creates a rectangular selection on the image for cropping and saving plots.

$$ROI\ witdh = \frac{Image\ width}{Total\ number\ of\ column} \tag{8.1}$$

$$ROI\ height = \frac{Image\ height}{Total\ number\ of\ row} \tag{8.2}$$

$$ROI\ position\ (xx) = i * ROI\ witdh \quad where\ i < Total\ number\ of\ column \tag{8.3}$$

$$ROI\ position\ (yy) = i * ROI\ height \quad where\ i < Total\ number\ of\ row \tag{8.4}$$

$$Excess\ Green = 2 \times Green\ (G) - Red(R) - Blue(B) \tag{8.5}$$

After obtaining the plot image, the next work is to segment plants from the noisy background. Soil and shadows in the plot images were eliminated using excess green (E × G) thresholding (Eq. 8.5). The pixel with an E × G value less than the cutoff (25) was replaced with black (255, black). The cutoff value was chosen empirically and through visual observation of segmented images. Then the three middle rows of each plot were manually cropped for further investigation since they had been chemically treated differently by plant pathologists (Fig. 8.3).

(a) (b) (c)

Fig. 8.2 Dataset generation process **a** stitched image of corn filed for feeding to a plot splitting tool developed in ImageJ; **b** the plot spitting tool for generating plots from stitched image; **c** output of the plot splitting tool: samples plot images

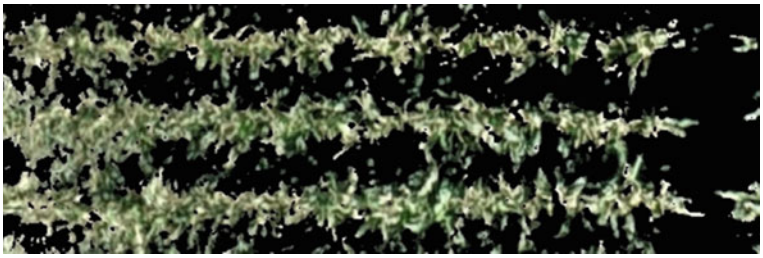

Fig. 8.3 Segmentation of plot images using excess green with threshold of 25

8.2.2 Preparation of Datasets

Three different datasets were prepared using the original plot images including non-augmentation, segmentation, augmentation. Non-augmentation dataset was prepared using 200 original plot images. Segmentation dataset also contained 200 plot images in which plants were segmented from backgrounds using E × G then cropping middle three rows of plants. Another dataset augmentation was prepared using original plot images in which geometric transformation techniques were used such as rotation, and flip (i.e., right, top, and random) (Table 8.1). The image rotation probability was set to 100%, implying that every image produced through augmentation was rotated slightly with a random chance. The parameters for rotation to the left were set to a maximum of 5 degrees and 10 degrees to the right (random rotation). With a probability of 50%, images were flipped to the left and right at random. Similarly, random flips from the top and bottom of the images were done with a 0.5 likelihood. Finally, images were zoomed randomly with a frequency of 30%, at a minimum scaling factor of 1.1, and a maximum scaling factor of 1.6. Augmentation dataset containing 6200 images, consisting of 3015 for high severity and 3185 for low severity. The parameters and techniques used for data augmentation is shown in Table 8.2. Photometric transformations were not used with the consideration that it might generate unreliable data with changed color values on individual pixels.

Table 8.1 Dataset description

Dataset	Description	Total	Training	Testing
Non augmentation	Original images	200	160	40
Segmentation	Original segmented images	200	160	40
Augmentation	Using augmentation techniques	6200	4960	1240

Table 8.2 Techniques used for preparing augmentation dataset

Augmentation techniques	Parameters	Values
Rotation	Probability, Angle	100%, 5°
Flipping (vertical, horizontal)	Probability	50%
Zooming	Probability, Scaling factors	30%, 1.1–1.6

8.2.2.1 Dataset for Training and Testing ML Algorithms

Features were extracted from all three datasets. A total of five textural features (i.e., contrast, dissimilarity, homogeneity, angular second moment, energy), nine color-based features (hue, saturation, value, red, green blue, lightness, and chromatic components *a and *b) were extracted. Gray-Level Co-occurrence Matrices (GLCMs) [6] based textural features were extracted. The code for textural were run in python (v3.8) using skimage python library. A function greycomatrix (image, distances, angles, levels, symmetric = False, normed = False) from the texture module was implemented. At first RGB images were converted into gray images using OpenCV. Images were fed to the function with 1-pixel distance offset, angle value of 90 and maximum 255 level to obtain GLCM matrices. Then the textural properties of the GLCM, such as contrast, dissimilarity, homogeneity, angular second moment was calculated using Eqs. (8.6), (8.7), (8.8), (8.9) and (8.10) respectively. Where i and j indicated the row and column number of the image window respectively; P_{ij} is the probability value in the cell i, j. Levels indicates number of rows or columns.

$$Contrast = \sum_{i,j=0}^{levels-1} P_{ij}(i-j)^2 \tag{8.6}$$

$$Dissimilarity = \sum_{i,j=0}^{levels-1} P_{ij} \mid i-j \mid \tag{8.7}$$

$$Homogeneity = \sum_{i,j=0}^{levels-1} \frac{P_{i,j}}{1+(i-j)^2} \tag{8.8}$$

$$Angular\,Second\,Moment(ASM) = \sum_{i,j=0}^{levels-1} P_{i,j}^2 \tag{8.9}$$

$$Energy = \sqrt{ASM} \tag{8.10}$$

Color features such red (R), green (G), and blue (B) pixel values were extracted from the datasets. Similarly, hue (H), saturation (S) value (V) features and lightness (L), chromatic components (*a and *b) were extracted images after converting RGB to HSV and L*a*b respectively. A total of 80% a dataset was used for training and remaining 20% were used for testing ML algorithms.

8.2.2.2 Dataset for Training and Testing DL Algorithms

The DL can extract features from the images automatically and it doesn't require handcrafted feature during training. Thus, features were not extracted from the datasets. All three datasets were used for modeling ML algorithms, but only augmentation dataset was used for modeling DL algorithms. The reason for excluding non-augmentation, and segmentation dataset for training DL was the insufficient number of training images. To avoid overfitting problem, only augmentation dataset were used for training DL algorithms.

8.2.3 Training and Validation of ML and DL Algorithms

ML algorithms were trained and validated on a computer configured with Intel® core™ i5-4300U CPU @ 1.90 GHz. Eight different machine learning classifiers were used to classify disease severity levels: Logistic Regression (LR), Ada Boost (AB), Gradient Boosting (GB), Support Vector Machine (SVM), Multilayer Perceptron (MLP), Random Forest (Rnaïveaive Bayes (NB), K-Nearest Neighbors (KNN). Machine learning algorithms were implemented using Scikit-learn [20] in python (v3.8). Parameters of ML algorithms were set default however the solver type and kernel for the LR and SVM was set to 'liblinear' and 'linear' respectively.

Two popular used DL algorithms (e.g., GoogLeNet and ResNet) were used for Goss's Wilt disease severity classifications. The DL algorithms were trained and validated on a computer configured with Intel® Core™ i7-4770 CPU @ 3.40 GHz. For consistency, both models' training epochs were set to 100. Cross entropy loss was used as the loss function, and stochastic gradient descent was used as the optimizer. The learning rate was set to 0.001, the momentum was set to 0.9, the step size was set to 7 and the gamma value was set to 0.1.

The performance of ML and DL algorithms were evaluated using precision, recall and F-score based on Eqs. 8.12, 8.13, and 8.14. True positive (TP) refers to correct predictions of high severity plots when plots are actually high severity. True negative (TN) indicates correct prediction of low severity plot when plots are actually low severity. False positive (FP) means incorrect predictions of high severity plots when plots are actually low severity. False negative (FN) indicates incorrect predictions of low severity plots when plots are actually high severity (Table 8.3).

Table 8.3 Confusion matrix for high severity and low severity class

		Predicted class	
		High severity	Low severity
Actual class	High severity	TP	FN
	Low severity	FP	TN

$$Precision = \frac{TP}{TP + FP} \tag{8.12}$$

$$Recall = \frac{TP}{TP + FN} \tag{8.13}$$

$$F - score = \frac{2 * Recall * Precision}{Recall + Precision} \tag{8.14}$$

8.2.4 Results

Regarding non-augmentation, GB achieved comparatively higher precision (0.85), recall (0.81) F-score (0.82) than other classifiers in this study (Table 8.4). In terms of precision (0.62) recall (0.61), and F-score (0.61), KNN had the lowest performance (Table 8.4). KNN achieved higher number of FN (10) than the other classifiers (Fig. 8.4). RF achieved comparatively similar precision (0.83), recall (0.78) and F-score (0.79) than the GB (Table 8.4).

On Segmentation dataset, RF achieved comparatively higher F-score (0.56) than other classifiers. LR and GB achieved similar precisions of 0.58 and 0.57, respectively and recalls of 0.56 and 0.57, respectively (Table 8.4). However, MLP achieved lowest precision (0.41) and F-score (0.40) comparatively to the other classifiers. MLP yielded highest FN (16) and lowest TP (3) than other classifiers (Fig. 8.4). Moreover, all the classifiers also yielded poor classification results (Table 8.4) (Fig. 8.5).

On augmentation dataset, RF classifiers outperformed other ML classifiers and achieved highest precision (0.99), recall (0.99) and F-score (0.99) (Table 8.4). It achieved higher TP (589) and TN (640) however, lower FN (5) and FP (6) among other classifiers (Fig. 8.6). The NB and MLP yielded lower precisions of 0.61 and 0.62 respectively, lower recall of 0.61 and 0.56 respectively and F-score of 0.60 and 0.51 respectively. The MLP and SVM yielded higher number of FN (465) higher number of FP (290) respectively (Fig. 8.6).

In this study, GoogLeNet and ResNet18 both performed good in classifying the disease severity. Though GoogleNet achieved 0.75 of precision, 0.70 of recall and 0.73 of F-score, Resnet18 yielded comparatively better precision (0.81), recall (0.78) and F-score (0.79). GoogleNet and ResNet both performed lower than ML classifier (RF) in terms of precision, recall and F-score on augmentation dataset (Table 8.5).

Figures 8.7 and 8.8 showed accuracy and loss curve of GoogLeNet and ResNet18 respectively. The lower gaps between training and validation loss indicated that the ResNet18 is good fitted with the dataset and free from overfitting problems (Fig. 8.8).

Table 8.4 Performance comparison of different machine learning (ML) algorithms in classifying Goss's Wilt disease severity on different types of dataset

Datasets	Machine learning classifiers	Precision	Recall	F-score
No augmentation	Logistic regression	0.79	0.76	0.76
	Ada boost	0.72	0.72	0.72
	Gradient boosting	0.85	0.81	0.82
	Support vector machine	0.80	0.73	0.73
	Multilayer perceptron	0.74	0.71	0.71
	Random forest	0.83	0.78	0.79
	Naive Bayes	0.82	0.76	0.76
	K-nearest neighbors	0.62	0.61	0.61
Segmentation	Logistic regression	0.58	0.56	0.54
	Ada boost	0.55	0.54	0.53
	Gradient boosting	0.57	0.57	0.57
	Support vector machine	0.55	0.54	0.52
	Multilayer perceptron	0.41	0.44	0.40
	Random forest	0.57	0.57	0.56
	Naive Bayes	0.43	0.42	0.42
	K-nearest neighbors	0.46	0.47	0.45
Augmentation	Logistic regression	0.68	0.67	0.67
	Ada boost	0.80	0.80	0.79
	Gradient boosting	0.89	0.89	0.89
	Support vector machine	0.73	0.71	0.70
	Multilayer perceptron	0.62	0.56	0.51
	Random forest	0.99	0.99	0.99
	Naive Bayes	0.61	0.61	0.60
	K-nearest neighbors	0.94	0.94	0.94

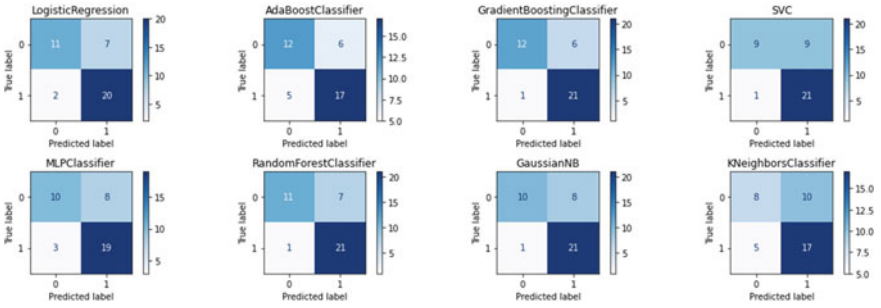

Fig. 8.4 Confusion matrix of classifications on non-augmentation dataset

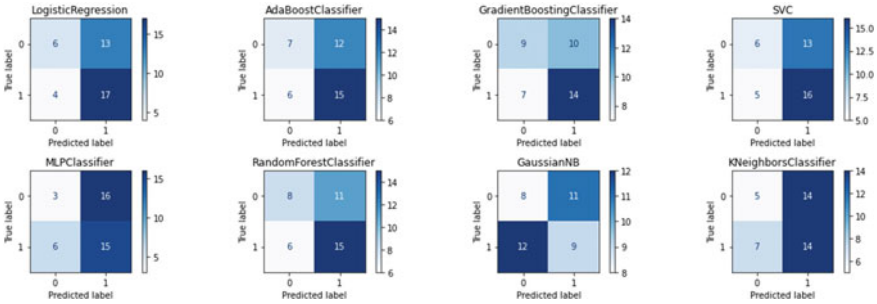

Fig. 8.5 Confusion matrix of classifications on segmentation dataset

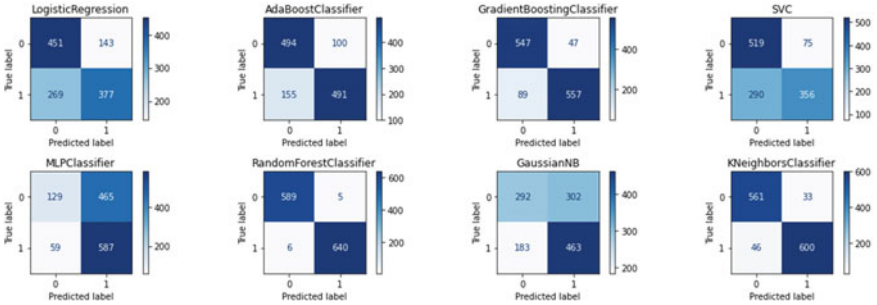

Fig. 8.6 Confusion matrix of classifications on augmentation dataset

Table 8.5 Evaluation matrices of Deep learning algorithms obtained during validation

Deep Learning Classifiers	Precision	Recall	F-score
GoogleNet	0.75	0.70	0.73
ResNet18	0.81	0.78	0.79

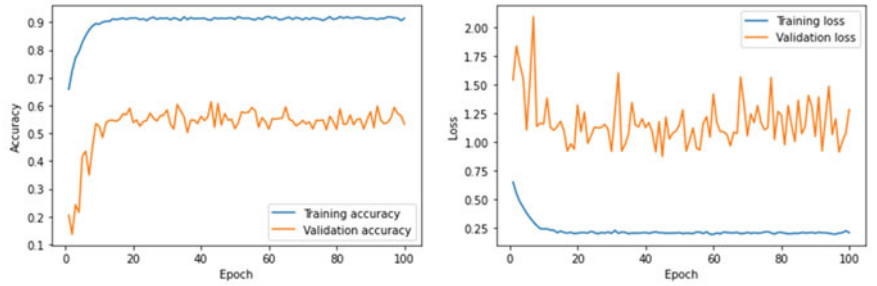

(a) **(b)**

Fig. 8.7 Accuracy and loss curve of GoogLeNet. **a** Training accuracy of 90% with 1–1.5% of training loss; **b** validation accuracy of 50 to 60% and 2.5% validation loss

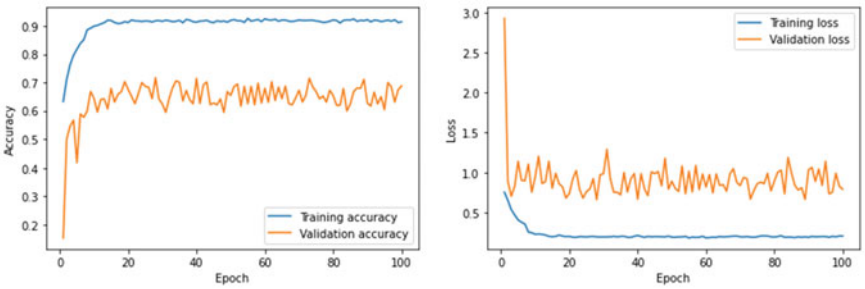

(a) (b)

Fig. 8.8 Accuracy and loss curve of ResNet18. **a** ResNet18 yielded around 90% of training accuracy and validation accuracy around 60–70%. **b** Training loss decreased gradually and reached 0% and validation loss reached between 0.5 and 1.5%

8.2.5 Discussion

The ML based algorithms constantly performed poor in terms of Precision, Recall and F-score on segmentation dataset. The probable reason for underperforming ML models on segmentation dataset was loss of information during segmentation. Plots were segmented using the threshold a value (25) which were determined empirically or manually. Dataset contained plot images from five different heights. The images from higher height might lose information higher than shorter heights which requires further investigations. RF algorithm outperformed other ML and DL based algorithms in this study and achieved F-score of 0.99. Conversely DL algorithms can extract features automatically and avoid manual feature extraction and selection process. Data augmentation enhanced the number of instances in training dataset helps ML and DL algorithms learn from adequate dataset.

8.2.6 Conclusion

This study concluded that ML algorithm (Random Forest) performed better in Goss's Wilt disease severity assessment in augmentation dataset, which can be recommended for severity assessment in future practical application. Random Forest yielded higher precision (0.99), recall (0.99) and F-score (0.99) among all ML algorithms. Random Forest can be incorporated to unmanned aerial imagery to build an automatic Goss's Wilt disease assessment system. ML models performed poor on the segmentation dataset. The effect of flight height on classification accuracy has not been investigated due to data limitations of individual heights (Total 40 images; training set: 32 images; testing set: 8 images). This could lead to model overfitting in ML. The effect of heights on accuracies will be investigated in future.

Acknowledgements Authors would like to express their gratitude to Jensen Kenton for his preliminary processing images collected by the unmanned aerial vehicle, which includes stitching them using Pixle4D and georeferencing them using ArcGIS10. Additionally, the authors would like to thank Dr. Friskop's specialists for assisting in the preparation of the experimental sites. This study was conducted in collaboration with the North Dakota Corn Commission and the USDA Agricultural Research Service under the project No. 6064-21660-001-32S. Project accession No. 435589.

References

1. Abdulridha J, Batuman O, Ampatzidis Y (2019) UAV-based remote sensing technique to detect citrus canker disease utilizing hyperspectral imaging and machine learning. Remote Sens 11(11):1373
2. Chemura A, Mutanga O, Sibanda M, Chidoko P (2018) Machine learning prediction of coffee rust severity on leaves using spectroradiometer data. Tropical Plant Pathology 43(2):117–127
3. Das AK, Friskop A, Flores P, Igathinathan C, Mathew JJ, Zhang Z (2021) Using aerial imagery coupled with machine learning to assess Goss's Wilt disease severity in field corn. In: 2021 ASABE annual international virtual meeting. American Society of Agricultural and Biological Engineers
4. Flores P, Zhang Z (2021) Wheat lodging ratio detection based on UAS imagery coupled with different machine learning and deep learning algorithms. Smart Agric 3(2):23–34
5. Greg Endres (2018, December 3) Goss's leaf blight and wilt of corn—carrington REC. https://www.ag.ndsu.edu/carringtonrec/center-points/2018/goss2019s-leaf-blight-and-wilt-of-corn
6. Haralick RM, Shanmugam K, Dinstein IH (1973) Textural features for image classification. IEEE Trans Syst Man Cybern 6:610–621
7. Jahan N, Flores P, Liu Z, Friskop A, Mathew J, Zhang Z (2020) Detecting and distinguishing wheat diseases using image processing and machine learning algorithms. ASABE Paper No. 2000372. St. Joseph, MI: ASABE. https://doi.org/10.13031/aim.202000372
8. Jahan N, Zhang Z, Liu Z, Friskop A, Flores P, Mathew J, Das A (2021) Using images from a handheld camera to detect wheat bacterial leaf streak disease severities. ASABE Paper No. 2100112. St. Joseph, MI: ASABE. https://doi.org/10.13031/aim.202100112
9. Kerkech M, Hafiane A, Canals R (2018) Deep leaning approach with colorimetric spaces and vegetation indices for vine diseases detection in UAV images. Comput Electron Agric 155:237–243
10. Kerkech M, Hafiane A, Canals R (2020) Vine disease detection in UAV multispectral images using optimized image registration and deep learning segmentation approach. Comput Electron Agric 174:105446
11. Kusumo BS, Heryana A, Mahendra O, Pardede HF (2018) Machine learning-based for automatic detection of corn-plant diseases using image processing. In: 2018 international conference on computer, control, informatics and its applications (IC3INA). IEEE, pp 93–97
12. Lee K, An H, Park C, So K, Na S, Jang S (2019) Estimation of rice grain yield distribution using UAV imagery. J Korean Soc Agric Eng 61(4):1–10
13. Liang Q, Xiang S, Hu Y, Coppola G, Zhang D, Sun W (2019) PD2SE-Net: Computer-assisted plant disease diagnosis and severity estimation network. Comput Electron Agric 157:518–529
14. Liu Z, Du Z, Peng Y, Tong M, Liu X, Chen W (2020, June) Study on corn disease identification based on PCA and SVM. In: 2020 IEEE 4th information technology, networking, electronic and automation control conference (ITNEC), vol 1. IEEE, pp 661–664
15. Mathew J, Zhang Y, Flores P, Igathinathane C, Zhang Z (2021) Development and testing of an RGB-D camera-based rock detection system and path optimization algorithm in an indoor environment. ASABE Paper No. 2100105. St. Joseph, MI: ASABE. https://doi.org/10.13031/aim.202100105

16. Meng R, Lv Z, Yan J, Chen G, Zhao F, Zeng L, Xu B (2020) Development of spectral disease indices for southern corn rust detection and severity classification. Remote Sens 12(19):3233
17. Mogili UR, Deepak BBVL (2018) Review on application of drone systems in precision agriculture. Procedia Comput Sci 133:502–509
18. Panigrahi KP, Das H, Sahoo AK, Moharana SC (2020) Maize leaf disease detection and classification using machine learning algorithms. In: Progress in computing, analytics and networking. Springer, Singapore, pp 659–669
19. Parikh A, Raval MS, Parmar C, Chaudhary S (2016, October) Disease detection and severity estimation in cotton plant from unconstrained images. In: 2016 IEEE international conference on data science and advanced analytics (DSAA). IEEE, pp 594–601
20. Pedregosa F, Varoquaux G, Gramfort A, Michel V, Thirion B, Grisel O, …, Duchesnay E (2011) Scikit-learn: machine learning in Python.J Mach Learn Res 12:2825–2830
21. Raeva PL, Šedina J, Dlesk A (2019) Monitoring of crop fields using multispectral and thermal imagery from UAV. Eur J Remote Sens 52(sup1):192–201
22. Ren T, Zhang Y, Wang C (2019, September) Identification of corn leaf disease based on image processing. In: 2019 2nd international conference on information systems and computer aided education (ICISCAE). IEEE, pp 165–168
23. Salgadoe ASA, Robson AJ, Lamb DW, Dann EK, Searle C (2018) Quantifying the severity of phytophthora root rot disease in avocado trees using image analysis. Remote Sens 10(2):226
24. Santoso H, Tani H, Wang X, Prasetyo AE, Sonobe R (2019) Classifying the severity of basal stem rot disease in oil palm plantations using WorldView-3 imagery and machine learning algorithms. Int J Remote Sens 40(19):7624–7646
25. Singh V, Misra AK (2017) Detection of plant leaf diseases using image segmentation and soft computing techniques. Inf Process Agric 4(1):41–49. https://doi.org/10.1016/j.inpa.2016.10.005
26. Stroppiana D, Villa P, Sona G, Ronchetti G, Candiani G, Pepe M, ... , Boschetti M (2018) Early season weed mapping in rice crops using multi-spectral UAV data. Int J Remote Sens 39(15–16):5432–5452
27. USDA ERS—Feedgrains Sector at a Glance. (n.d.). Retrieved May 3, 2021, from https://www.ers.usda.gov/topics/crops/corn-and-other-feedgrains/feedgrains-sector-at-a-glance
28. Wang G, Sun Y, Wang J (2017) Automatic image-based plant disease severity estimation using deep learning. Comput Intell Neurosci. https://doi.org/10.1155/2017/2917536
29. Yao L, Hu D, Zhao C, Yang Z, Zhang Z (2021) Wireless positioning and path tracking for a mobile platform in greenhouse. Int J Agric Biol Eng 14(1):216–223. https://doi.org/10.25165/j.ijabe.20211401.5627
30. Zhang J, Wan L, Igathinathane C, Zhang Z, Guo Y, Sun D, Cen H (2021b) Spatiotemporal heterogeneity of chlorophyll content and fluorescence response within rice (Oryza sativa L.) Canopies under different nitrogen treatments. Front Plant Sci 12, 499. https://doi.org/10.3389/fpls.2021.645977
31. Zhang Z, Flores P (2021) Detection of wheat lodging plots using indices derived from multispectral and visible images. In: Li J, Zhang Z (eds) Nondestructive evaluation of agro-products by intelligent sensing techniques. Sharjah, United Arab Emirates, pp 1–299. https://doi.org/10.2174/9789811485800121010 1
32. Zhang Z, Flores P, Igathinathane C, Naik LD, Kiran R, Ransom JK (2020) Wheat lodging detection from UAS imagery using machine learning algorithms. Remote Sens 12(11):1838. https://doi.org/10.3390/rs12111838
33. Zhang Z, Heinemann PH, Liu J, Baugher TA, Schupp JR (2016) The development of mechanical apple harvesting technology: a review. Trans ASABE 59(5):1165–1180. https://doi.org/10.13031/trans.59.11737
34. Zhang Z, Igathinathane C, Li J, Cen H, Lu Y, Flores P (2020) Technology progress in mechanical harvest of fresh market apples.Comput Electron Agric 175:105606. https://doi.org/10.1016/j.compag.2020.105606
35. Zhang Z, Lu Y, Lu R (2021) Development and evaluation of an apple infield grading and sorting system. Postharvest Biol Technol 180:111588. https://doi.org/10.1016/j.postharvbio.2021.111588